

FIELD EMISSION OF ZNO NANO-STRUCTURES PRODUCED BY LASER ABLATION

A thesis submitted for the degree of

Doctor of Philosophy

Presented to:

The School of Physical Sciences, Faculty of Science and Health,
Dublin City University.

Author

Conor McLoughlin B.Sc.

Research Supervisor

Dr. Jean- Paul Mosnier

December 2009

Declaration:

I hereby certify that this material, which I now submit for assessment on the programme of study leading to the award of Doctorate of Philosophy is entirely my own work, that I have exercised reasonable care to ensure that the work is original, and does not to the best of my knowledge breach any law of copyright, and has not been taken from the work of others save and to the extent that such work has been cited and acknowledged within the text of my work.

Signed: _____

ID No.: 51309145

Date: _____ / _____ / _____

Dedication:

To Anne and to my parents.

Acknowledgements:

First and foremost I would like to thank my supervisor, Dr. Jean- Paul Mosnier, for his constant availability, encouragement, support, guidance and patience, despite the many problems encountered, his direction and help always got me through. I would also like to thank Dr. Enda McGlynn for all his help and direction over the past number of years.

I will always be grateful to Prof. John Costello, Dr. Tony Cafolla, Dr. Brian Lawless and Prof. Greg Hughes for their availability, willingness to loan equipment and discussions on materials, electronics, vacuum systems or any number of odd questions I asked of them over the course of my PhD.

To my many colleagues over the years, Jean-Rene, who taught me much about materials (not to mention that my name is not the best name to have in France), RT for the many hours spent in the lab, Brendan, who I'll never forget describing me "as a frightened deer in car headlights!" and I also learned so much about ion probes from, and Pat Yeates, who, when the ReTOF wouldn't work said high voltage is the way to go! turns out he was right, thanks to you all.

Thanks to Padraig, without whom my PhD would not have been the same, we had some great moments. Ricky, for lots of advice about everything and anything and of course for CoD! Also thanks to Barry Brennan who I have "borrowed" so much from over the years and had many a chat with about "random stuff". Thanks to Alexandra for the TEM/AFM work and trying to set up a collaboration with Chalmers... we never quite got there! Thanks Martin for his very successful summer work experience with the FE system. And all the members of the physics department who made my day to day experiences so enjoyable, those who have moved on, Justina, Eoin, Caroline, John D., Jofre, Alan and Deirdre, and of course the people who are still around, Mossy, Eanna, Jack, Conor C., Vincent, Jiang Xi, Mahua, Colm and Paddy H, thanks for the many discussions over coffee. Thanks to my office buddies for all the gossip and tea, Paddy K, Mairead, Ruth and Daragh, hang in there Paddy... I know the chats about knitting can get to a man!

I must express my appreciation to Lisa for all the orders and printing and also to all the technicians in the department, Des for understanding my very bad design explanations, Pat for all the electronics circuits especially in the early days, Mike for the gas and Alan for every other problem that would arise, thank you all.

I must thank my parents, for their support encouragement and the many lifts, and finally, Anne, always asking questions that made me really think about my thesis, for keeping me sane and not letting me give up!

Abstract:

The thesis describes the development of, and results from, two new laboratory facilities designed to investigate the properties of laser produced plasmas, with in-situ time of flight mass spectrometry, for deposition of ZnO materials for applications as field electron emission sources.

The results from the work are concerned with the study of the important physical processes present in a laser ablation zinc oxide plasma plume expanding into vacuum and various ambient gas pressures.

The thesis also demonstrated the advantages of combining a linear ToF detector and a mass resolved ReToF spectrometer for clarification of ionisation processes in the pulsed laser ablation regime of solid targets. The outstanding results show that during the ablation process, ZnO atomises into Zn and O. In the vacuum regime we have shown that at long distances from the target multiple charged states of Zn and O are present. While under the same conditions in an ambient gas the multiple charged states are not present, however the ambient gas undergoes an ionisation process.

Deposited materials are tested for applications as field electron emission sources, for analysis of field enhancement factors from nano-material ZnO.

Table of Contents

Declaration:.....	i
Dedication:.....	ii
Acknowledgements:	iii
Abstract:.....	iv

Chapter 1: INTRODUCTION

1.1	Organisation of Thesis:.....	1
1.21	Motivation: ZnO	2
1.22	Motivation: PLD.....	4
1.23	Motivation: Clusters.....	6
1.24	Motivation: Field Emission.....	7
1.3	Thesis Objectives:.....	8

Chapter 2: THEORETICAL BACKGROUND

2.1	<i>Field Emission:.....</i>	<i>9</i>
2.2	<i>Work Function of Solids.....</i>	<i>9</i>
2.3	<i>Thermionic Electron Emission:</i>	<i>10</i>
2.4	<i>Schottky Emission:.....</i>	<i>13</i>
2.5	<i>Field Electron Emission:.....</i>	<i>15</i>
2.6	<i>Fowler-Nordheim Tunnelling:.....</i>	<i>17</i>
2.7	<i>Field Emission analysis:</i>	<i>23</i>
2.8	<i>Geometry Effects:.....</i>	<i>24</i>
2.9	Plasma Definition:	26
2.10	Laser ablation:.....	28
2.11	Plasma Expansion:.....	31
2.12	Ion Probes:	35
2.13	Mass Spectrometry:	38

Chapter 3: EXPERIMENTAL DEVELOPMENT

3.1	Experimental Design, Field Emission:	45
3.1a	<i>System Layout:</i>	<i>46</i>
3.1b	<i>Electrical Design:</i>	<i>48</i>
3.2	Field Emission Computer Interface:.....	51
3.3	Experimental Design: ReTOF System:	54
3.3a	Vacuum Systems:	54
3.3b	ReTOF Set-Up:	59
3.3c	Ion Probe:.....	62
3.3d	Laser Systems:.....	63
3.4	Electrical Design and Timing:	64
3.5	Simulation Program (SIMION):.....	67
3.6	Computer Interface:.....	72
3.7	System Calibration:	75

Chapter 4: FIELD EMISSION: RESULTS AND ANALYSES

4.0	<i>Field Emission Background and Interpretation:.....</i>	<i>80</i>
4.1	<i>Field Emission Results From Hybrid Growth Technique:</i>	<i>81</i>
4.2	<i>Hybrid Growth Morphologies:.....</i>	<i>84</i>
4.3	<i>Field Emission Results from ZnO nanorods grown by Hybrid Growth Method :</i>	<i>86</i>
4.4	<i>Interpretation of the Data:.....</i>	<i>90</i>
4.5	<i>Field Emission Results From PLD Growth Technique:</i>	<i>90</i>
4.6	<i>Sample Growth:.....</i>	<i>91</i>
4.7	<i>PLD Growth Morphologies:</i>	<i>91</i>
4.18	<i>Field Emission Results from PLD Growth and Analysis</i>	<i>94</i>

Chapter 5: ANALYSIS OF LASER PRODUCED ZnO PLASMAS

5.0	Background and motivations	98
5.1	Ambient effects comparison between vacuum, O ₂ and N ₂ atmospheres.....	102
5.2	Electron temperature analysis:	104
5.13	Ion Temperature Analysis	106
5.2	Mass spectrometry analysis of ZnO:	112
5.3	Laser ablation of ZnO via 1064 nm:	113
5.31	High Fluence Regime Pressure Scans:.....	113
5.32	Low Fluence Regime Pressure Scans:	117
5.4	Laser ablation of ZnO via 532 nm:	120
5.41	High Fluence Regime Pressure Scans:.....	120
5.42	<i>Low Fluence Regime Pressure Scans:</i>	<i>123</i>
5.5	Laser ablation of ZnO via 355 nm:	126
5.51	High Fluence Regime Pressure Scans:.....	126
5.51	Low Fluence Regime Pressure Scans:	129
5.4	Ionisation of a ZnO target via 266 nm Laser Radiation:.....	132
5.5	Summary of Mass Spectra Analysis:	137

Chapter 6: CONCLUSIONS AND OUTLOOK

.....	139
Appendix A.	141
Appendix B:	144
Appendix C:	145
References:.....	147

Chapter 1:

INTRODUCTION

1.1 Organisation of Thesis:

Here I present the work I carried out for my PhD studies in the Centre of Laser Plasma Research (CLPR), a wing of the National Centre for Plasma, Science and Technology (NCPST), based in the School of Physical Sciences at Dublin City University.

The thesis is split into six chapters. A short description of each chapter is given below.

Chapter 1: is a brief overview followed by a review of the thesis subject of study, the semiconducting material zinc oxide, and the reasons for its study in this thesis.

Chapter 2: is concerned with electron emission from solids, field emission theory and the theory of laser produced plasmas and diagnostics techniques.

Chapter 3: presents the design of our field emission apparatus and the required computer interfacing for it. The laser plasma system is also presented from, the design of this system, modelling the flight of laser produced ions through electric fields, computer interfacing and calibration of the system.

Chapter 4: describes the growth of various ZnO materials and our measurements of their field emission properties.

Chapter 5: shows the mass spectra of ablation plumes obtained for various parameters.

Chapter 6: presents the conclusions of the work and future prospects.

Appendix A: is made up of flowcharts of the Labview programs used to control some of the equipment for the experiments.

Appendix B: is the MatLab program used for data recovery

Appendix C: is the procedure used to create the Phosphor screens used for Field emission.

1.21 Motivation: ZnO

The main driving force for this thesis is the wide band gap material Zinc Oxide (ZnO). ZnO occurs naturally in a mineral form known as zincite, whose colour can range from pale yellow to dark red depending on the impurities / defects present.

It is a part of the group II-VI, compound semiconductor family, with a hexagonal wurtzite structure whereby four zinc atoms tetrahedrally surround every oxygen atom and every zinc atom is surrounded by four oxygen atoms (Fig. 1.1).

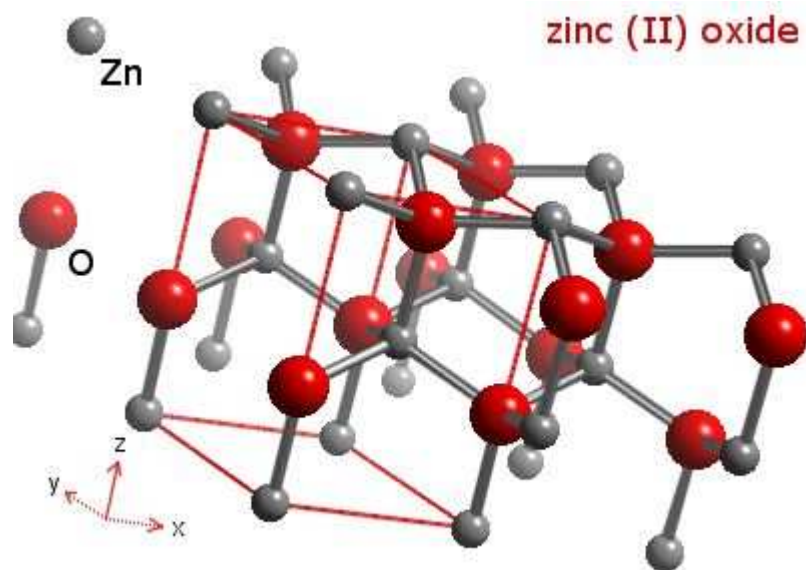


Figure 1.1 Hexagonal Wurtzite Structure of ZnO [1]

ZnO is not new to research, with studies of its lattice parameters dating from 1935 when C. W. Bunn used electron and x-ray diffraction methods to investigate ZnO “smoke” which was made by the combustion of pure granulated zinc of “forensic quality” [2].

Interest in ZnO was reignited within the last twelve years after Bagnall et al. [3] showed lasing from it at room temperature. With a direct, (fig 1.2), wide band gap of 3.37 eV at room temperature corresponding to ~ 370 nm, ZnO has many potential applications as a photonic material for the fabrication of UV / blue devices such as light emitting diodes, laser diodes, nanolasers and photodetectors.

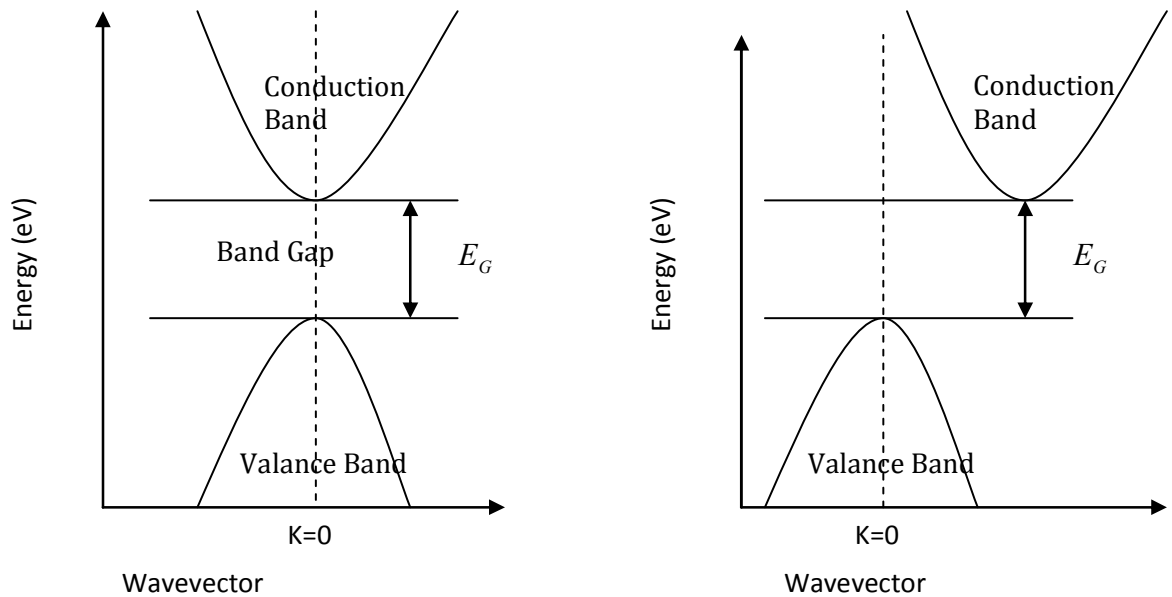


Figure 1.2 Direct band gap, with maximum energy of the valence band and minimum energy of the conduction band occurring at the same wavevector i.e. same location of the first Brillouin zone, and in-direct band gap with this relationship shifted.

This bandgap, coupled with an exciton binding energy of 60 meV, makes ZnO special in that room temperature excitonic emission can be studied for the material. There are other materials which display wide band gap properties and therefore are viable UV emitters, such as Gallium Nitride (GaN) with a band gap of 3.39eV, (~ 365 nm), but the exciton binding energy is rather low at ~ 21 meV, meaning that at temperatures above ~ 162 K the exciton is dissociates. Similarly for zinc sulphide (ZnS) with a band gap of 3.8eV corresponding to an excitation wavelength of ~ 365 nm, the exciton binding energy is ~ 39 meV, meaning that at temperatures above ~ 301 K the exciton is dissociates.

Simple thermal energy at room temperature, (293 K), can be enough to break the bond between electron-hole pairs due to the fact that room temperature thermal energy is $\sim 37\text{meV}$.

Radiative emission from an exciton recombination has a much higher transition probability than emission from an electron-hole transition. This is because of the highly correlated motions of the electron and hole in the exciton form.

Most importantly for us, ZnO is one of the most versatile materials for the fabrication of a plethora of nanostructures, including nanorods and nanowires [4]. The fact that these nano-structures have a large surface area makes them ideal for gas and chemical sensing as well as electron emitters. Moreover for possible future applications, the nucleation sites, for the growth of ZnO, are controllable making them useful for lasing devices and memory arrays [5], with a control of the packing densities and a control of the vertical alignment being additional positives for field emission experiments and optical pixel applications.

ZnO is radiation hard [6], hence ZnO based electronic devices could operate in satellites circling in low earth orbits. It is significantly more radiation hard than silicon (Si), gallium arsenide (GaAs), and GaN which is of utmost importance in preventing wearing out during field emission [6]. In traditional nano-scale field emission devices the wearing out of the tip due to radiation damage is a major reliability issue [7].

1.22 Motivation: PLD

With regards to the deposition technique used in this work, for the most part, it is that of pulsed laser deposition, (PLD). This is a well established technique for the deposition of thin films [8] and it has also proved successful for the growth of nano wires [9] and nanorods [10].

The basic idea of the deposition process is quite simple, a pulsed laser, (Q-switched), vaporises the surface of a target, in a moderate vacuum, creating a plasma which expands normal to the target surface. The ablated material then

re-condenses on the substrate some distance from the target surface. The properties of the deposited material will typically depend on the experimental parameters such as the substrate temperature, the laser fluence, the target to substrate distance, the gas pressure and nature of the gas in the chamber.

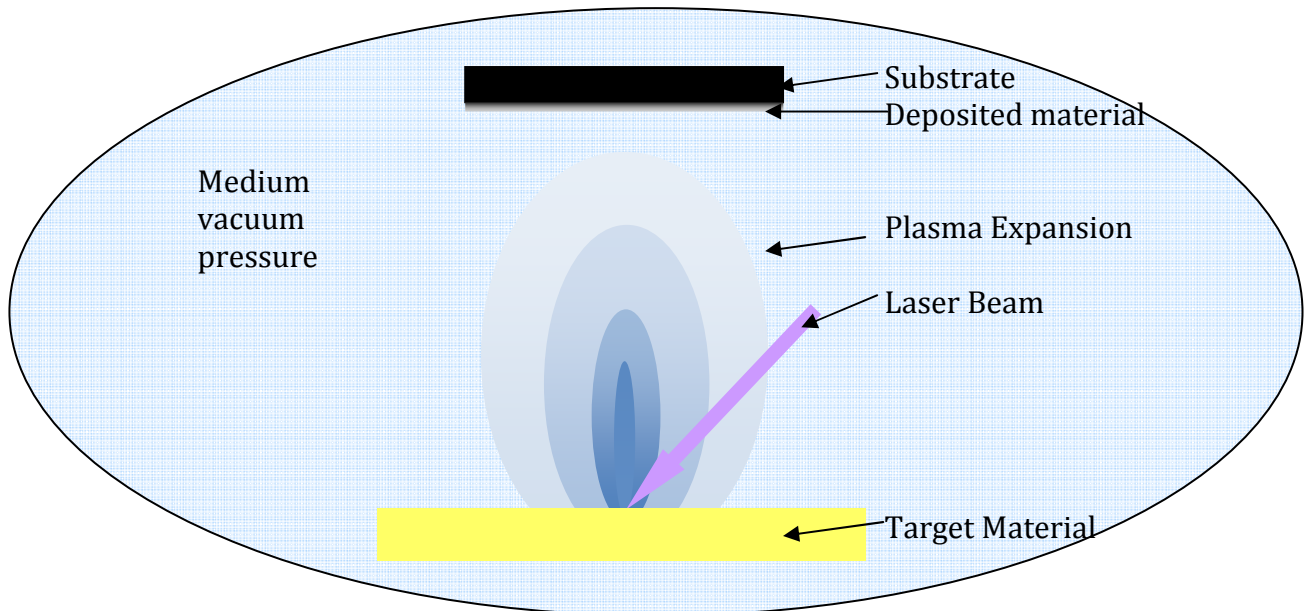


Figure 1.2: Schematic of PLD

PLD is a versatile deposition technique, characterised by specific features such as:

1. There is the possibility of producing microstructure at relatively low substrate temperatures,
2. The rate of deposition is relatively high,
3. There is the possibility to deposit multi-component thin films with the same stoichiometry of the multi-component materials used as targets.
4. It is also possible to produce heterostructure i.e. multilayered films of many different materials.

Unfortunately there are some drawbacks to this technique:

1. Uniform films or nanostructures are generally difficult to acquire.

2. For large scale production the turnaround time is quite long, with generally small area deposition.

1.23 Motivation: Clusters

A cluster is a small ensemble of bound atoms, three or more atoms constitute a so called “cluster”.

The formation of nanoparticles or clusters in the laser produced plasma plume of ZnO is a question which has yet to be resolved [11-12]. One of the motivations for this thesis is to explore the formation of clusters, the ionisation properties of the laser ablated material and the corresponding effects on the deposited material.

Sometimes the ablation of a material will produce some preferential clusters for example the element, Lead (Pb) has been shown to produce more clusters of $n=7, 10, 13, 17$ and 19 atoms than other cluster groups [13]. This means that these clusters numbers are more stable and are given the name, $n =$ “magic numbers”.

Clusters of metallic particles have been produced by pulsed laser techniques ever since the mid 1990’s with Jogender Singh, as described by Clark. [14], producing silver nanoparticles in a liquid solution and controlling the size of the nanoparticles by controlling the laser energy and rotation speed of the target.

The topic of clusterisation in a ZnO laser ablated plasma has been investigated in the course of this study, with some works already performed on ZnO clusters. A more extensive review of recent publications on the clusterisation of ZnO is given in chapter 5, however just for example, Kukreja et al. [15], have measured mass spectra for a nitrogen laser, with low fluences of 0.125 J/cm^2 and 0.01 J/cm^2 . They recorded a complete series of $(\text{ZnO})_n$ clusters up to $(\text{ZnO})_{20}$. No enhancements of the cluster yield, corresponding to n equals to a magic number was observed. Behrman et al. [16] had previously shown using molecular-dynamics simulations of ZnO clusters that at certain magic numbers ($n=12, n=16$) of atoms the clusters spontaneously form into fullerene-

like spheroids. These theoretical predictions have not been verified experimentally to date and so, during the course of this study a systematic study, of high and low fluences, effects of background gas pressure and effect of laser wavelength on the measured mass spectra of laser ablated ZnO has been performed.

1.24 Motivation: Field Emission

The presence of clusters in the plume would lead one to believe that they would result in the formation of nanoparticles, leading to nucleation sites on the surface of a substrate used for deposition and ultimately the formation and growth of nanostructures. In order to test any nanostructures grown in this facility, a field emission facility was constructed.

The field emission facility has two specific functions. Firstly it can produce an image pattern of the surface, with equally spaced nanostructures, with uniform height and made from the same material, emitting electrons at the same electric field density. The second measurable properties via field emission are the electrical properties which will be discussed in detail in chapter 2.

With the research into nano-materials and the growth morphologies obtainable by researchers, field emission from metal planes or Spindt tip emitters are being replaced by nano-rods [17], nano-tubes [18] and any high aspect ratio nano-material which has the potential to be a better emitter than the traditional metallic tips used for field emission experiments [19]. The so called field enhancement factors, which will be discussed later, of nanomaterials can be in the thousands, so it is possible to use low electric fields to generate electron emission, which results in low power consumption electron sources.

This makes field emitting electron sources a topical research area with these emitters finding their niche in applications such as field emission scanning electron microscopy, field emission flat panel displays and many other vacuum microelectronic devices.

The field emission display (FED) is one of the most important applications, the display properties are seen as a real alternative to cathode ray

tubes (CRT) [20], working on the same principle of electron emission with the added advantages of less scatter of emitted electrons and the compactness of a liquid crystal displays (LCD).

1.3 Thesis Objectives:

The aim of this work is to investigate the field emission properties of various growths of ZnO, using the growth techniques of PLD and a hybrid PLD vapour transport technique.

It is also intended to directly measure the influence of varying laser fluence, gas pressure and laser wavelength on the detected mass spectra for the laser ablation of a ZnO target.

For the higher pressure regime of 10^{-2} mbar, with a relatively high fluence of the fundamental output of the Nd:YAG laser employed for this study, an ionisation of a background gas is also shown. The mass spectrometer was used to confirm this ionisation and data via ion probe time of flight is used to supplement the mass spectra, adding additional information about the flight profile, electron and ion temperatures.

Chapter 2:

THEORETICAL BACKGROUND

2.1 Field Emission:

“Field emission (FE) is defined as the emission of electrons from the surface of a condensed phase into another phase, usually a vacuum, under the action of high electrostatic fields [21].

2.2 Work Function of Solids

Electrons in metals and semiconductors can be approximately considered as a Fermi gas, that is, the electrons move freely inside the metal. The electrons cannot freely escape the metal surface as there is a potential barrier known as the work function. The value of the work function is given by the difference in the energy between the highest occupied electron energy level inside the metal or semiconductor, the conduction band, and the vacuum level, the electron at rest outside the surface, fig 2.1. For electron emission to occur the electrons must somehow pass through or over this barrier and be released from the surface.

The work function depends on both the bulk properties and surface characteristics of a metal or semiconductor. In the bulk properties, this dependence arises from the difference in energy of the highest filled level compared to the mean electrostatic potential in the material. While for the surface structure, the dependence occurs from the difference between the potential inside the material and the potential outside the material.

This difference in energy levels resulting in the potential barrier arises due to the so called double layer [22], fig 2.1. This is formed due to the fact that positive charges cannot move freely in a metal or semiconductor, resulting in a constant positive charge density up to the surface and no positive charges exist beyond that of the material. If this double layer were not to exist, it would correspond to an infinite gradient of the wave function and therefore to an infinite kinetic energy. In the deep bulk the electron density equals that of the

positive charge density, but the electron density falls gradually up to the surface rather than a sudden disappearance [23]. The result of this is an excess of negative charge just outside the surface and an excess positive charge just inside the surface. This electrostatic potential gives rise to the energy barrier known as the work function. In addition to this there is a contribution to the work function by a Coulomb-like attractive image force, known as the classical image potential, experienced by any charged particle in front of a conductive material [22].

Basing their method on a model in which the positive charges inside a metal are replaced by a uniform background of positive charge density, Lang and Kohn [24] developed a method for calculating the work function of metals which takes into account both the surface double layer dipole potential and the image potential. Their results agreed with experimental results of many metals, leading to further computationally concise works for determining the barrier for field and thermionic emission potentials [25].

2.3 Thermionic Electron Emission:

Electron emission is the process by which electrons near the top of the conduction band of a metal or semiconductor escape from the surface. For one of these electrons to escape the surface it must undergo one of two processes, thermal excitation or tunnelling.

If the electron is excited by an energy greater than the work function the electron is able to overcome the potential barrier. This electron emission can result from the application of heat, by absorption of light quanta of sufficient energy to cause photoelectric emission or by a collisional ionisation via energetic particles incident on a conducting target surface ionising the surface and releasing an electron. All these excitations are considered thermionic electron emission processes.

Thermionic emission is caused by the transfer of energy from vibrations of the crystal lattice to the free electrons. The energy transferred should be greater than the height of the potential barrier for emission to occur.

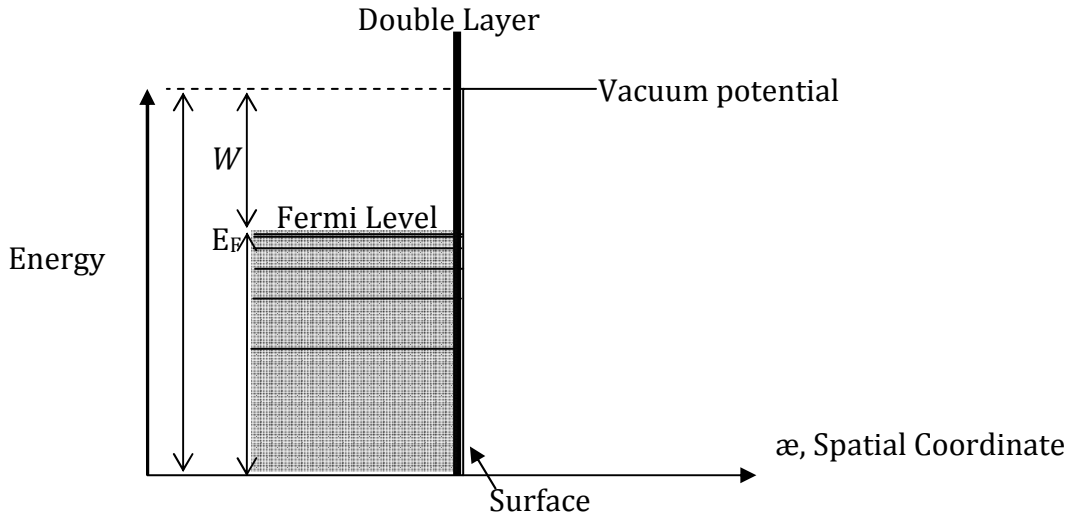


Figure 2.1 Schematic of the electron energy in a conductor. W is the work-function and E_F is the Fermi energy.

At a temperature of zero Kelvin the electron distribution function is a step function, i.e. there is a probability of unity for an electron to occupy a state below the Fermi energy, the energy of the highest occupied state at zero kelvin, and zero probability for the electron to occupy a state above the Fermi energy.

$$f(E) = \begin{cases} 0 & \Rightarrow E > E_F \\ 1 & \Rightarrow E < E_F \end{cases}$$

(2.1)

Where $f(E)$ is the probability the electron will occupy a quantum state, E is the energy of the state and E_F is the Fermi energy.

At temperatures above absolute zero, electrons can be excited and occupy levels above the Fermi level, the Fermi level is equal to the Fermi energy at absolute zero but differs at temperatures above that. The probability that there is an electron in a particular single-particle state with energy E is now given by:

$$f(E) = \frac{1}{e^{\left(\frac{E-\mu}{kT}\right)} + 1}$$

(2.2)

Where μ is the Fermi level, also known as the chemical potential, k is Boltzmann's constant and T is the absolute temperature.

From this equation it is quite easy to understand that the probability an electron occupies a particular state increases with increasing temperature, and decreases with a decreasing temperature, assuming $E - \mu$ remains constant.

Further understandings of the electron emission process were developed by the Nobel laureate Owen Richardson, who in 1913 first realised that in strong electric fields cold discharges could be made to pass in highly exhausted tubes [26]. Later, he proposed that the emission current density could be represented by the mathematical form [27]:

$$J = \lambda_R \left[\frac{4\pi m k^2 e}{h^3} \right] T^2 e^{\frac{-W}{kT}}$$

(2.3)

Where J is the emission current density, λ_R is a material-specific correction factor that is typically of ~ 0.5 , m and e are the mass and charge of an electron, h is Planck's constant and W is the work function of the metal.

In 1928 with the publication of a paper by L.W. Nordheim [28] there was agreement that, due to the wave-like nature of electrons, as a result of the image force, some proportion, R , of the outgoing electrons would be reflected back into the material as they reached the emitter surface, so the emission current density would be reduced, resulting in:

$$J = (1 - D) \left[\frac{4\pi m k^2 e}{h^3} \right] T^2 e^{\frac{-W}{kT}}$$

(2.4)

Where D is the emission coefficient, R is the reflection coefficient and $R+D=1$.

2.4 Schottky Emission:

In the presence of an applied electric field the emission of electrons becomes more complicated.

As mentioned earlier, an electron outside a conducting plane induces a positive charge on the surface. This positive charge results in an image charge force experienced by the electron.

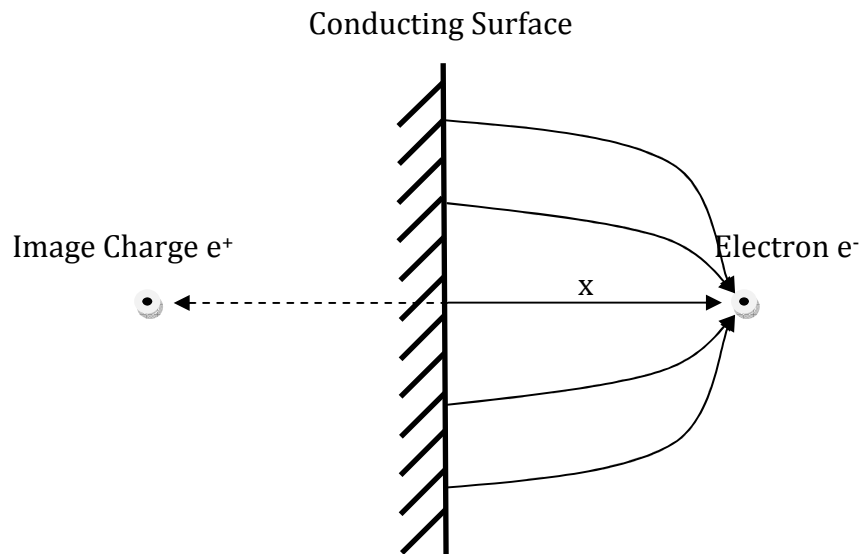


Figure 2.2 The image charge, e^+ , of an electron in front of a conducting plane, e^- . The image charge has the opposite charge of the electron and the distance between the image charge and the conducting surface is equal to the distance between the electron and the plane.

The image charge force experienced by the electron is an electrostatic force between the electron and image charge. Taking “ x ” as the distance from the conducting surface to the electron, the electrostatic force the electron experiences is equal to:

$$f = \frac{-e^2}{4x^2}$$

(2.5)

Where f is the image charge force.

The energy of an electron transferred from infinity to a distance “ x ” from the surface is given by:

$$E(x) = - \int_{-\infty}^{\infty} f dx = \frac{-e^2}{4x}$$

(2.6)

The effect of this image force is that the barrier height remains the same, W , however the step potential at the surface is rounded, described later in figure 2.3a, this is the initiation of the so called Schottky lowering effect discussed by Nordheim [28].

In Schottky emission the work function is reduced under the application of an electric field [29]. Without the field, the surface barrier seen by an escaping Fermi-level electron has height W equal to the local work-function. The electric field lowers the surface barrier by an amount ΔW , and increases the emission current. It can be modelled by a simple modification of the Richardson equation, by replacing W by $(W-\Delta W)$. This gives the equation:

$$J = \lambda_R \left[\frac{4\pi m k^2 e}{h^3} \right] T^2 e^{\frac{-(W-\Delta W)}{kT}}$$

(2.7)

Where: $\Delta W = W - V_{max}$

(2.8)

V_{max} is the Schottky lowering potential energy [30], given by:

$$V_{max} = (e^3 F)^{1/2}$$

(2.9)

Where “ F ” is the electric field.

Equation 2.7 is relatively accurate for electric field strengths lower than about 10^8 V/m. For electric field strengths higher than 10^8 V/m, Fowler-Nordheim tunnelling becomes the major source of electron emission.

Millikan and Lauritsen tried to unite the relations of field currents to thermionic currents, their conclusion was that “The application of an external field is equivalent to increasing the temperature of the electrons within the metal.” [31] These claims were later questioned by Fowler and Nordheim [32].

2.5 Field Electron Emission:

As stated earlier, electron emission may also occur due to tunnelling. In a tunnelling process, the height of the potential barrier is reduced and the electrons escape due to their wave characteristics. The tunnelling process has been dubbed “cold cathode emission” or more commonly “Field Emission”.

In field emission there is no thermal heating, but only electron tunnelling. The barrier is deformed by the electric field into a triangular form so much so that unexcited electrons can leak out through it. This phenomenon was first reported in 1897 by R.W.Wood [33], who was actually looking for a way to produce very intense x-rays so as he could analyse the diffraction bands produced. The first mathematical explanation was made by Ralph H. Fowler and Lothar W. Nordheim in 1928 [32], who developed, what is now known as the Fowler-Nordheim law, also called the field emission equation.

Figure 2.1 shows an electron energy band diagram of a conductor for thermal emission of electrons. Figure 2.3 shows the effects of the image potential (a), the Schottky lowering without the image potential (b) and their combined effect (c).

From figure 2.3 a) we see the steep discontinuity at the surface is rounded, the resulting barrier is smaller near the surface than that obtained by neglecting image effects.

Figure 2.3 b) shows the effect of an external electric field on the barrier height. When a field is applied to the conducting surface, electrons of kinetic energy, V_x , along the emission direction, see a barrier of height $E_F + W - V_x$ and thickness, $x = (E_F + W - V_x) / Fe$. Provided this barrier is small enough, the electron penetration will occur.

Ultimately in the presence of an electric field, both the image effect and the presence of an applied field have to be considered. For this, we look to Figure 2.3 c), where we can see the potential energy of an electron in the case of field electron emission. The potential at the metal surface, in eV, in the presence of a constant electric field “ F ” is given by [30]:

$$V(x) = -\frac{e^2}{4x} - Fex, \quad x > \text{Vacuum potential} \quad (2.10)$$

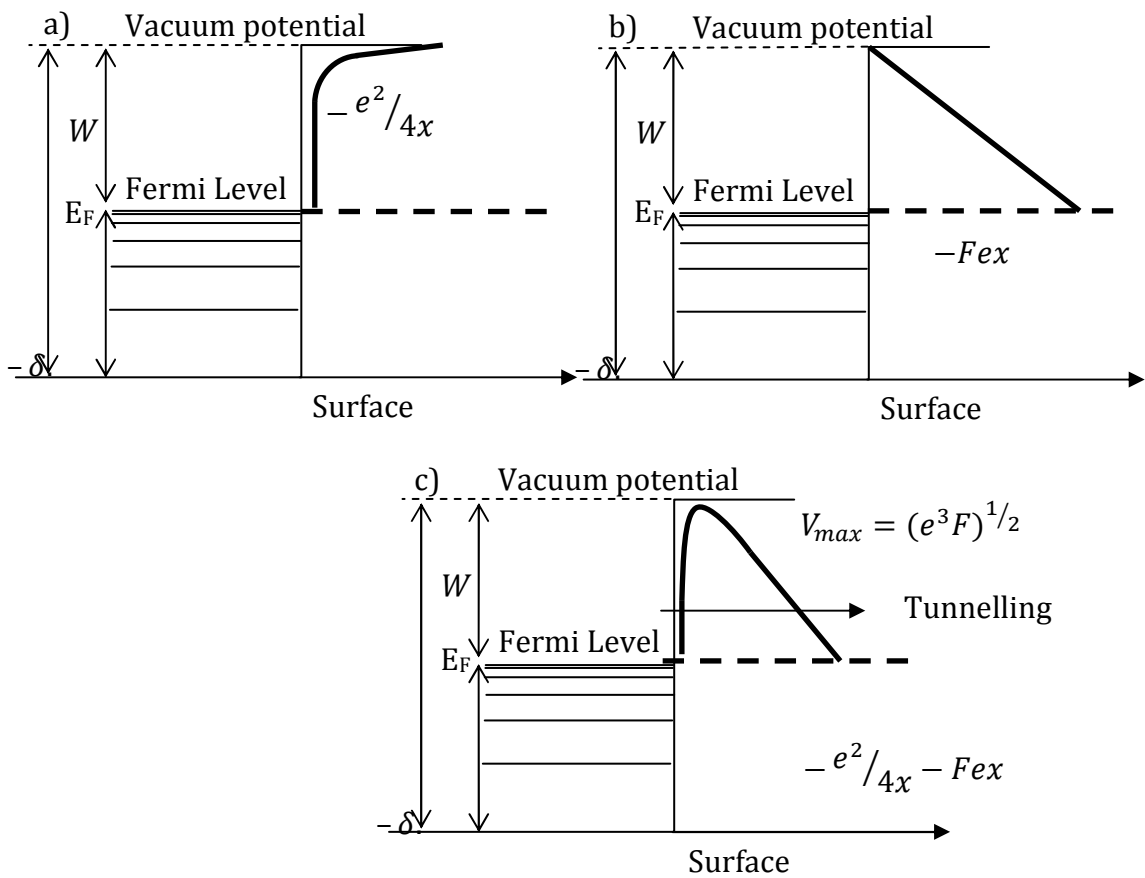


Figure 2.3: Schematic of the Schottky lowering effect on the potential barrier in a conductor. a) corresponds to the image potential effect, b) corresponds to the effect of the external field and c) corresponds to the sum of both the image potential and external field.

This is known as “the effective potential model” and its reasoning is as follows: firstly the potential energy of the electrons within the metal is constant and equal to $-\delta$, the energy difference between the bottom of the metal

conduction band and the vacuum level. Secondly, if an external field is applied, F , this field gives a contribution $-Fex$ to the potential barrier, W . It is assumed that within the metal, there is no field penetration as the free charges cause this field to be neutralised. Finally the image potential goes to zero when the electron is far from the metal.

2.6 Fowler-Nordheim Tunnelling:

The standard physical assumptions of the theory of cold field electron emission (CFE) first used by Nordheim in 1928 [28] were:

1. The free electron gas model for the conducting electrons, which is that the electrons are completely detached from their ions.
2. The effective potential model.
3. Electrons inside the metal remain at equilibrium.

According to the Fowler-Nordheim model, electrons arriving at the surface of a conducting material obey Fermi-Dirac statistics and penetrate the potential barrier at the surface of the material with a probability that is predicted by a solution of the Schrödinger equation [34].

Figure 2.4 shows a one dimensional potential energy diagram of an electron near the surface of a conductor, here the potential energy of an electron outside the surface is given as the zero point, previously this has been shown as the vacuum energy level. The total energy of an electron, ε , under the surface energy potential $V(x)$ is then given by:

$$\varepsilon = \frac{P_x^2}{2m} + \frac{P_y^2}{2m} + \frac{P_z^2}{2m} + V(x)$$

(2.11)

Where P_x, P_y , and P_z , are the momentum components of the electron in x, y, and z directions.

The “x” part of the energy can be written as:

$$\begin{aligned}\delta &= \varepsilon - \frac{p_y^2}{2m} - \frac{p_z^2}{2m} \\ &= \frac{p_x^2}{2m} + V(x)\end{aligned}$$

(2.12)

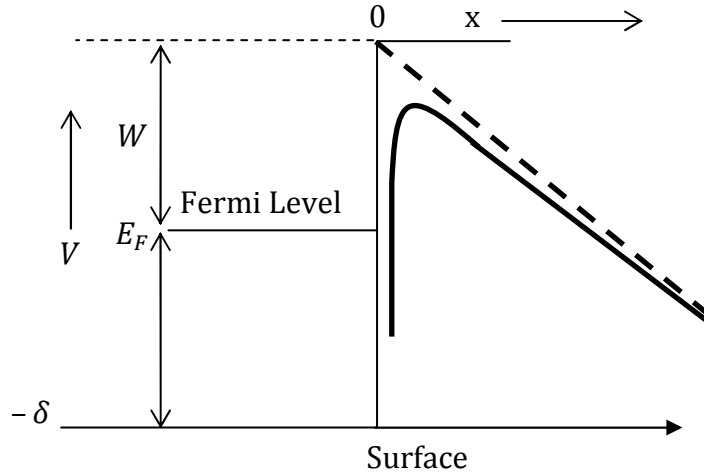


Figure 2.4: One-dimensional potential energy $V(x)$ of an electron near a metal surface, for the Fowler-Nordheim model. Here the zero point is taken as the vacuum energy level and E_F represents the Fermi energy.

In the derivation of the Fowler-Nordheim equation a number of assumptions are made. Firstly, that all energies will be measured from the same reference as the effective potential $V(x)$. A supply function is defined as $N(\delta)d\delta$, it is the number of electrons with the “x” part of their energy, from equation 2.12, within the range δ to $\delta+d\delta$ incident on the surface per second per unit area. The barrier penetration probability for an electron with an energy δ , is defined as $D(\delta)$, with the product, $P(\delta)d\delta$, of the supply function and the penetration probability giving the number of electrons within $d\delta$ that emit from the conductor per second per unit area.

$$P(\delta, \varepsilon)d\delta d\varepsilon = D(\delta)N(\delta, \varepsilon)d\delta d\varepsilon$$

(2.13)

While the total energy distribution is given by:

$$P(\varepsilon)d\varepsilon = \int_{\delta} P(\delta, \varepsilon)d\delta d\varepsilon$$

(2.14)

And finally, “ j ”, the electric current per unit area is defined as:

$$j = e \int_{-\infty}^{\infty} P(\delta)d\delta,$$

(2.15)

The supply function and the transmission coefficient must now be solved. In Fermi-Dirac statistics the number of electrons with energy ε is uniform for the solid angle ω . The number of electrons incident between the angles θ and $\theta + d\theta$, equal to that between the electron velocity vector and the normal to the surface, and between ϕ and $\phi + d\phi$, equal to the azimuthal angle created from some point of reference, with an energy between ε and $\varepsilon + d\varepsilon$ on the unit surface at $x=0$ per unit time is given by the product of the number of electrons arriving at θ per solid angle and the differential solid angle:

$$N(\omega, \varepsilon)d\omega d\varepsilon = n(\varepsilon)d\varepsilon \frac{|v|\cos\theta}{4\pi} \sin\theta d\theta d\phi$$

(2.16)

Where $|v|$ is the magnitude of electron velocity given by:

$$|v| = \left[2(\varepsilon - V)/m \right]^{1/2}$$

(2.17)

Manipulation of equation 2.17 utilising equation 2.12 results in the possibility to integrate equation 2.16 over ϕ to obtain:

$$N(\omega, \varepsilon)d\omega d\varepsilon = \frac{-n(\varepsilon)d\delta d\varepsilon}{2[2m(\varepsilon - V)]^{1/2}}$$

(2.18)

Where $n(\varepsilon)$ is the number of electrons per unit volume within the metal between ε and $\varepsilon + d\varepsilon$.

$n(\varepsilon)d\varepsilon$ is the energy distribution in a Fermi Dirac electron gas with energy measured relative to an electron at rest at a position of ∞ .

$$n(\varepsilon)d\varepsilon = \frac{4\pi(2m)^{3/2}(\varepsilon - V)^{1/2}d\varepsilon}{h^3 \exp\left[\frac{\varepsilon - W}{kT}\right] + 1}$$

(2.19)

The supply function needed to solve the Fowler-Nordheim equation is then given by [34]:

$$N(\omega, \varepsilon)d\omega d\varepsilon = -\frac{4\pi m}{h^3} * \frac{d\omega d\varepsilon}{\exp\left[\frac{\varepsilon - W}{kT}\right] + 1}$$

(2.20)

As for the transmission coefficient, $D(\delta)$, it was calculated using the Wentzel-Kramers-Brillouin (WKB) approximation [35].

$$D(\delta) = \exp(-c + (\delta - E_f)/d)$$

Where:

$$c = \frac{4(2mW^3)^{1/2}}{3\hbar eF} v \left(\frac{(e^3 F)^{1/2}}{W} \right)$$

$$d = \frac{\hbar eF}{2(2mW)^{1/2} t \left(\frac{(e^3 F)^{1/2}}{W} \right)}$$

$$t(y) = v(y) - \frac{2}{3} y \frac{dv(y)}{dy}$$

(2.21)

Where “ t ” is a slowly varying function ranging from 1.00 to 1.11.

From these equations 2.13 and 2.14, the total energy distribution goes to:

$$P(\varepsilon)d\varepsilon = \int_{\delta=\varepsilon}^{\infty} D(\delta)N(\delta, \varepsilon)d\delta d\varepsilon \Rightarrow$$

$$P(\varepsilon)d\varepsilon = \exp\left(-c - \frac{W}{d}\right) * \frac{4\pi md}{h^3} * \frac{\exp\left(\frac{e}{d}\right)}{\exp\left[\frac{\varepsilon - W}{kT}\right] + 1} d\varepsilon$$

(2.22)

The product of a field and work function dependant barrier penetration probability and the Fermi-Dirac distribution function is given by the energy dependant portion of this function, with equation 2.22 resulting in the total energy distribution for field emitted electrons.

This can now be inserted into the Fowler-Nordheim equation, 2.15, to obtain:

$$j = e \int_{-\infty}^{\infty} P(\delta)d\delta = \exp\left(-c - \frac{W}{d}\right) * \frac{4\pi md}{h^3} * \int_{-\infty}^{\infty} \frac{\exp\left(\frac{e}{d}\right)}{\exp\left[\frac{\varepsilon - W}{kT}\right] + 1} d\varepsilon$$

(2.23)

With a further manipulation resulting in the standard Fowler-Nordheim equation, 2.24, in the higher temperature approximation, limited to the region where $kT < d$.

$$j = \frac{e^3 F^2}{8\pi h W t^2 \left(\frac{(e^3 F)^{\frac{1}{2}}}{W}\right)} * \exp\left[\frac{-4(2m)^{\frac{1}{2}} E_F^{\frac{3}{2}}}{3\hbar e F} v\left(\frac{(e^3 F)^{\frac{1}{2}}}{W}\right)\right] * \frac{\frac{\pi k T}{d}}{\sin\left(\frac{\pi k T}{d}\right)}$$

(2.24) [34]

If the work function, W , is represented in eV and F in V/cm, equation 2.24 results in:

$$j = \frac{1.54 * 10^{-6} F^2}{W t^2 \left(3.79 * 10^{-4} \frac{F^{\frac{1}{2}}}{W} \right)} * \exp \left[-6.83 * 10^7 \frac{W^{\frac{3}{2}}}{F} v \left(3.79 * 10^{-4} \frac{F^{\frac{1}{2}}}{W} \right) \right] A. cm^2$$

(2.25)

This equation is often seen without the function t , as it is usually set to unity as a simplification with $1/t^2$ seen only to vary between 1.00 and 0.81[36].

Finally, the Fowler-Nordheim equation referred to in the modern literature, to describe the process of field emission, including the emission area, A , in terms of the emitted current using quantum mechanical tunnelling in a triangular barrier is given by: [32]

$$I = \frac{aAF^2}{W} \exp \left\{ \frac{-bW^{\frac{3}{2}}f(y)}{F} \right\}$$

(2.26)

I = emission current, $a = 1.514 * 10^{-6} eV V^{-2}$, $b = 6.83 * 10^9 AeV^{\frac{-3}{2}} V^{-2}$
 A = Emission area, F = macroscopic electric field, W = work function, and
 $f(y)$ = is a function of the variable $y = \frac{3.79 * 10^{-4} F^{\frac{1}{2}}}{W}$.

This equation assumes a flat emission surface and that the local field is the macroscopic field.

An extension of the Fowler-Nordheim treatment was developed by Sommerfield and Bethe [37] to include a factor known as the field enhancement factor, to take account of the fact that the local electric field may differ from the macroscopic value, due to sharp emission tips an explanation of which will be given in section 2.8, which is of utmost importance in field emission theory:

$$I = \frac{aA(\beta F)^2}{W} \exp \left(\frac{-bW^{\frac{3}{2}}}{\beta F} \right)$$

(2.27)

Where β = Field Enhancement factor and βF is the local electric field.

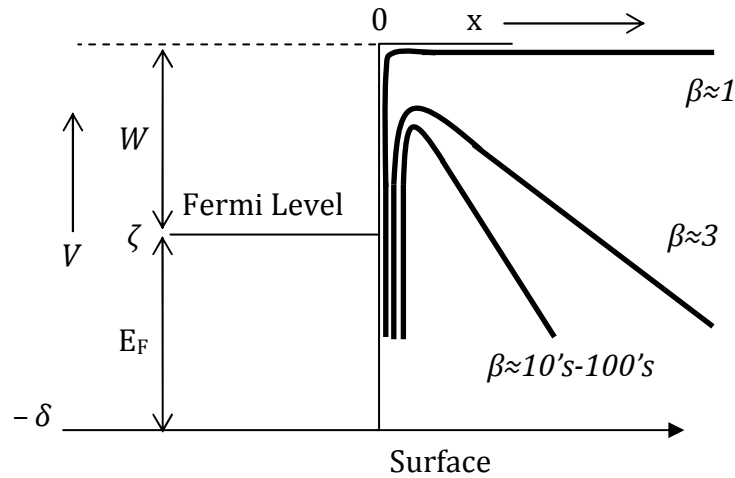


Figure 2.5: Schematic of the effect of the Field enhancement factor on the potential barrier in a conductor.

2.7 Field Emission analysis:

The main measurement made in a field emission experiment is the field emitted current versus applied electric field (I-F) characteristic. Currents are recorded as electric field is increased.

The analysis of a field emission experiment then involves the plotting of a simple current versus voltage curve, with the data giving information about the turn on fields, determined by extrapolation of the I-V curve to the x-axis intersect, and the threshold of emission, defined as the electric field necessary to achieve a "minimum current density", where the current density is defined as a value making the sample useful for requirements in a particular application. For example a current density of 10 mA/cm² is necessary for a field emission flat panel display

Then from this IV curve if a plot is made of $\log\left(\frac{I}{F^2}\right)$ against $\frac{1}{F}$, a straight line indicates field emission is the dominant emission process and the slope of this line is equal to:

$$\text{Slope} = \frac{-bW^{\frac{3}{2}}}{\beta}$$

(2.28)

from the Fowler – Nordheim equation.

2.8 Geometry Effects:

In practise there are two basic types of field emission device, planar or pointed. Previously I have discussed planar conducting surfaces in relation to the so called double layer.

Figure 2.6 depicts these double layers. The electron distribution in the interior of the conducting surface does not terminate abruptly, but instead there is a gradual decay, resulting in an electron deficiency just inside the conductor surface, figure 2.6 a), with the negative end outermost. If the surface is atomically rough, figure 2.6(b), electrons are seen to flow into the concave portions of the stepped surface. This results in a double layer with the outermost end positive. This opposes the first type of double layer, shown in figure 2.6 a). Essentially the electrostatic potential between the electron cloud above the surface and positive electron deficiency just below the surface in an atomically flat conductor is given an extra positive potential above the electron cloud in the atomically rough surface, this potential adds an attractive force to the electrons and is equivalent to reducing the potential barrier.

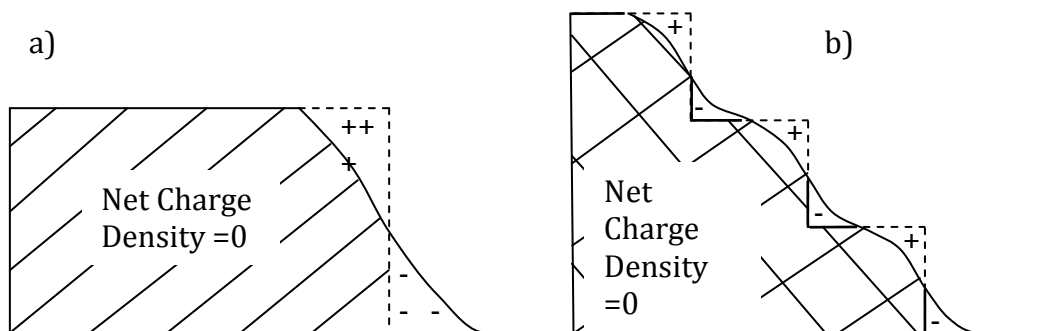


Figure 2.6: Charge distribution at a conductor surface, a) atomically smooth surface, b) atomically stepped surface.

The consequences of this is that very closely packed crystal faces will have high work functions and atomically rough or loosely packed ones will have lower work functions [21].

In recent years with the production of nanomaterials, high-aspect ratio materials whose geometry ensures the maximum field at the tip apex, have become the preferred material for field emission experiments as local electric fields can be determined more accurately with emission sites more predictable.

Nanomaterials with the same aspect ratios, perpendicular to the substrate, but most importantly with equal spacing to their neighbouring nano-particle should emit electrons at the same electric fields and with the same intensities. A closer spacing will result in a shielding effect of the electric field imposed on the nano-particle. Samples which are not uniformly perpendicular to the substrate will stretch the electric field around the particle while varying heights again affect the electric field experienced by the emitter.

It should also be mentioned that in many cases for nanomaterials the field enhancement factor is approximately equal to [38]:

$$\beta = \frac{h}{r}$$

(2.29)

h = the height of the emission tip, r = the radius of the emission tip.

2.9 Plasma Definition:

Plasmas are accepted as the fourth state of matter with unique properties which clearly characterise them as differing from those of solids, liquids and gases. This state of matter is essentially that of an ionised gas, whereby some of the atoms or molecules have either lost or gained an electron. The plasma consists of electrons which are no longer bound to an atom or molecule, and of positively charged atoms known as ions. These charged particles, although capable of a collective motion, are not exactly “free”, as they are strongly affected by each other’s electromagnetic fields [39]. The charged particles make the plasma electrically conductive and therefore respond to electric fields.

Ionisation of the gas can take place in a variety of ways but in general is due to the absorption of energy from an external source, e.g. the application of DC or low frequency RF, or high frequency RF electric fields. The system must then meet certain criteria to be defined as plasma:

- (a) Collective processes: The charges in a plasma will act on their neighbours with a Coulombic force. These forces between charged particles in plasmas are strong with a relatively long-range of influence. Beyond a certain distance, known as the Debye length, λ_D , the Coulombic force of an ion is completely shielded by the electrons. The Debye length, calculated in metres, is [40]:

$$\lambda_D = \left(\frac{\epsilon_0 k T}{n_e e^2} \right)^{1/2}$$

(2.30)

Where ϵ_0 is the permittivity of free space, k is the Boltzmann constant, T is the temperature in Kelvin, n_e is the density of electrons and e is the electric charge. The Debye sphere centred about an ion has a volume V_D given by:

$$V_D = \frac{4}{3} \pi \lambda_D^3$$

(2.31)

Only beyond the Debye length are the collective properties of the plasma dominating the influence of neighbouring charged particles and the plasma as a

whole displays a collective behaviour to any disturbing influence. Therefore the length of the plasma, L , must be much greater than the Debye length.

$$L \gg \lambda_D$$

(2.32)

(b) Electrical neutrality: In order for the system to be neutral, the interactions in the bulk of the plasma must be more important than those at the edges. To meet this criterion the Debye length must be short. The condition for electrical neutrality is written as:

$$n_e = \sum_z n_z z$$

(2.33)

Where n_z is the density of ions in the z^{th} ionisation state, $z=0$ for neutrals; $z=1$ for singly charged; etc... [41].

(c) Dominating plasma frequency: The plasma frequency, more specifically the electron plasma frequency, is the most fundamental time scale in a plasma. It corresponds to the typical electrostatic oscillation frequency of a given species in response to a displacement, dx , of the electron cloud from an equilibrium position. The plasma frequency must be large in comparison to the frequency of collisions between electrons and neutral particles, when this condition is met, electrostatic interactions will dominate over ordinary gas kinetics.

$$\omega_p = \left(\frac{n_e e^2}{m_e \epsilon_0} \right)^{1/2}$$

(2.34)

Where ω_p is the plasma frequency [42].

This plasma frequency plays a crucial role in laser produced plasmas, which is the ionisation method we employ.

2.10 Laser ablation:

The power flux density of the laser is another crucial aspect in the plasma creation. There are three main laser irradiance regimes, low ($I < 10^6 \text{ Wcm}^{-2}$), medium ($10^6 \text{ Wcm}^{-2} < I < 10^{10} \text{ Wcm}^{-2}$) and high ($I > 10^{10} \text{ Wcm}^{-2}$).

In a low irradiance regime, the main processes are heating, melting and vaporisation. This regime is typically used in medicinal and data storage applications.

In the intermediate irradiance regime, $10^6 \text{ Wcm}^{-2} < I < 10^{10} \text{ Wcm}^{-2}$, plasma effects begin to play a role in the physics of the evaporated material. However, the laser radiation penetrates through to the target surface for the duration of the laser pulse. This regime is used where the maximum mass of ablated material is desirable and is therefore used in applications such as pulsed laser deposition (PLD) or plasma etching.

If the irradiance is increased to $I > 10^{12} \text{ Wcm}^{-2}$, the plasma frequency will increase with the increased electron density [43] causing more of the light radiation to become shielded from the target and resulting in further heating of the ablated material. Simultaneously, there are large pressure gradients in existence in the plasma so that the plasma expands, causing a reduction in electron density and, hence, plasma frequency so that the laser radiation will again penetrate through to the target surface. This cycle is repeated until laser pulse termination.

This initial heat absorption takes place over a very thin surface layer known as the skin depth [44]:

$$\delta = \left(\frac{\lambda}{c\pi\mu_0\sigma} \right)^{\frac{1}{2}}$$

2.35)

Where c is the speed of light, λ is the wavelength of the laser used, μ_0 is the magnetic permeability of free space and σ is the electrical conductivity of the target.

If the laser light absorption takes place over a significantly shorter time scale than the ablated material expansion, the process may be described in two distinct parts, the interaction of the beam with the target and initial plume formation followed by the plume expansion into vacuum/background gas. In the case of plasma creation using femto- or picosecond lasers, thermal conduction may be neglected since there is insufficient time for the diffusion of heat and further melting and evaporation to take place so that the laser absorption depth is comparable to, or greater than, the heat penetration depth.

For nano-second laser pulses, the heat penetration depth, δ_h , is usually much larger than the laser absorption length [45]:

$$\delta_h = 2(at_p)^{\frac{1}{2}}$$

(2.36)

Where t_p is the time duration of the laser pulse, a is the thermal diffusivity $a = \frac{K}{\rho C}$, with K the thermal conductivity in $\text{Wm}^{-1}\text{K}^{-1}$, ρ is the density in kg m^{-3} and C is the specific heat capacity in $\text{J K}^{-1} \text{kg}^{-1}$.

Evaporation occurs when the energy absorbed by the target material is greater than the enthalpy of vaporisation. In most practical cases of laser-material interaction, the transverse dimensions of the laser beam are large in comparison to the heat penetration depth and the heat flow into the target is treated as a one dimensional process, as described below.

For nanosecond lasers, there is enough time for the energy to diffuse into the target material so that the ablated depth can be written as,

$$Z_a \approx \frac{A(F_{th} - F_L)}{\rho L_v}$$

(2.37)

Where A is the surface absorbance of the target material, F_L is the fluence and the fluence threshold, F_{th} , is the energy necessary to vaporize a

surface layer of the order of the laser absorption length, at initial temperature T_0 and melting temperature T_m , and is given by,

$$F_{th} \approx \frac{\rho c (T_m - T_0) L_{th}}{A}$$

(2.38)

With the surface absorbance, $A=1.0-R$, of the target and, hence, the reflectance, R , dependent on the refractive index, n , of the target material and the absorption coefficient, k , so that [46]:

$$R = \frac{(n-1)^2 + \kappa^2}{(n+1)^2 + \kappa^2}$$

(2.39)

For example, a ZnO target ($n=1.99$, $\kappa=0.34$ [47]) irradiated with a 266 nm laser radiation has an absorbance of 0.88.

The pulsed laser deposition of oxide material such as ZnO usually requires the presence of a background gas in order to reproduce the oxygen stoichiometry of the target material in the deposited films. The presence of this background gas and its possible reactive character influences the kinetic energy, the spatial distribution and even the nature of the species present in the plasma.

The analytical model of Phipps et al. [48], based on self-regulating absorption via inverse bremsstrahlung, works well when the laser intensity is sufficiently high that a fully ionised plasma is established early in the pulse, permitting approximate prediction of the dependence of ablation pressure, mechanical coupling coefficient, and related parameters such as pulse laser intensity, wavelength, and pulse width.

The work presented here is concerned with laser ablation plasmas of ZnO in the regime applicable to the intermediate irradiance regime for nano-second pulses.

2.11 Plasma Expansion:

The expansion of a laser produced plasma can be explained as follows: firstly the laser impacts on the target surface, next there is the formation of a so called Knudsen layer, followed by unsteady adiabatic expansion; i.e. no heat is transferred to or from the expanding plasma with a leading edge of electrons followed by the ions; and finally the regime of free expansion.

There are a large number of variables for modelling the expansion of a laser produced plasma, such as electron and ion temperatures, ionisation potentials of the target material, laser wavelength and energy, electron and ion velocities, plasma densities, background medium and pressure to mention just a few. The vast bulk of plasma models treat the plasma as a gas [49-50-51].

In order to characterise a laser produced plasma, many different techniques are required. Generally we can define two categories, particle based and radiation based diagnostics. Those belonging to the radiation based category would be techniques such as optical spectroscopy, fast photography or laser interferometry to name just a few. While for the purposes of this thesis the techniques employed are considered particle based, electrostatic probes and mass spectrometry, that is to say that the probing technique directly interacts with the charged particles.

It is commonly assumed that in a laser produced plasma the velocity distribution of particles is Maxwellian and therefore allows a calculation of the temperature. A condition for a statistical approach to be valid is that the mean free path between collisions must be much smaller than the maximum extension of the plasma, and the time between these collisions must be short compared to other heating mechanisms.

Assuming the emission of particles is collisionless, the velocity distribution function of thermally emitted particles is defined as a half-range Maxwellian, fig 2.7, of the form [52]:

$$\begin{aligned}
f_s^+(v_x, v_y, v_z, E_I) &= \frac{n_s}{(2\pi kT_s/m)^{3/2}} * \frac{E_I^{(j/2-1)}}{\Gamma(j/2)(kT_s)^{j/2}} \\
&* \exp\left[-\frac{2E_I + m(v_x^2 + v_y^2 + v_z^2)}{2kT_s}\right]
\end{aligned}$$

;

$$v_x \geq 0; -\infty < v_y < \infty; -\infty < v_z < \infty;$$

(2.40)

Where E_I is the total internal energy, n_s is the gas number density near the surface of the emitting target, T_s is the surface temperature, Γ is the gamma function (an extension of the factorial function to real and complex numbers) and j refers to the number of degrees of freedom at T_s .

For equation 2.40 to hold true, the thermal emission of particles requires that the velocities normal to the surface take on only positive values, i.e. there are no collisions, there is no re-condensation at the surface and the angular distribution scales as $\cos\theta$.

The behaviour of emitted particles from a target surface has been summarised by Kelly et al., figure 2.7, [53] summarised below.

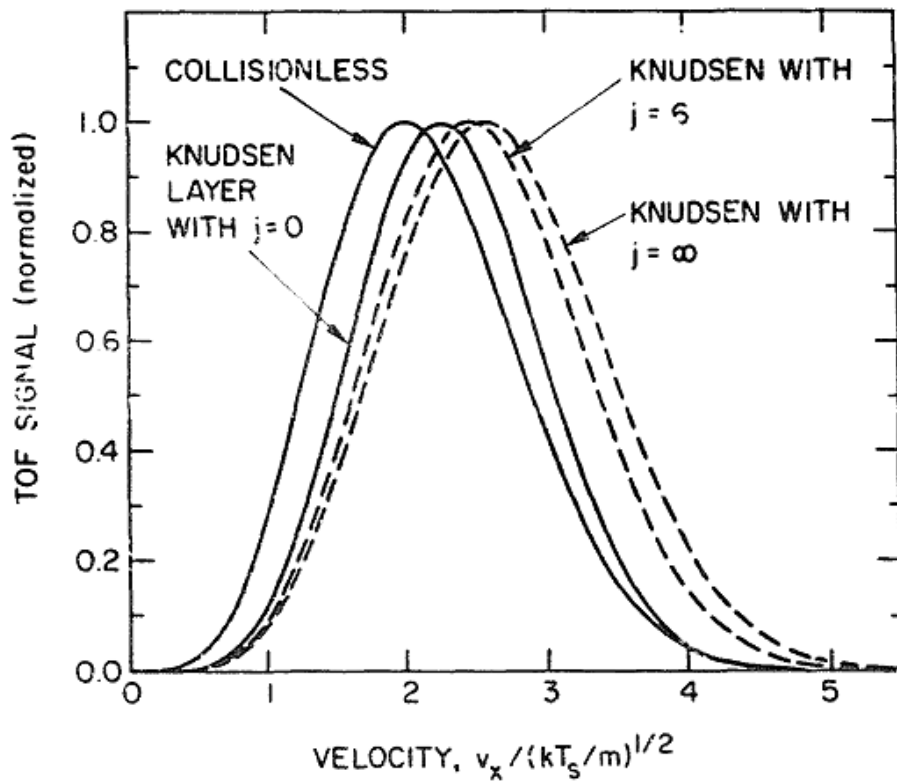


Figure 2.7: Comparison of ToF spectra as would be obtained with a small density sensitive detector located a distance x normal to a small target.

The first case, as discussed above, describes the particles emitted from the target surface which are not energetic enough to form a so-called Knudsen layer, a layer formed at higher vapour densities where many collisions occur near the surface, and therefore all the velocity vectors are positive. This is the case when the gas number density near the surface is equal to that in the Knudsen layer, $n_s = n_k$, the surface temperature equals the Knudsen layer temperature, $T_s = T_k$, and centre of mass component $u_k = 0$.

The second case is an extension of the first, with the emission containing enough particles for collisions. These collisions result in a retarding velocity emanating from a region of several mean free path thickness at the target surface, known the Knudsen layer. It is a layer between liquid and vapour. As a result of this layer the velocity components of the emitted particles can be towards or away from the target surface, i.e. $f = f^\pm$, this is discussed below.

Finally the third case describes a class of particles which re-condense at the surface and is ascribed a distribution function $f = f^-$, with $v_x \leq 0$. The sticking probability of re-condensing particles is assumed to be unity.

Considering the fact that there can be dense particle emission from a surface irradiated by intense laser radiation, resulting in a laser produced plasma, there needs to be the addition of a retarding velocity in the x-direction to describe the velocity distribution function of thermally emitted particles. It has been shown that a fluence of $>200\text{mJ}/\text{cm}^2$ is sufficient to initiate a Knudsen layer [54].

This negative velocity component is a so called centre of mass component u_k , and results in the distribution function being a full-range Maxwellian due to possible negative values of the x-direction, it also means there will be a lower temperature T_k , and lower number density n_k , than there is at the surface:

$$\begin{aligned}
 f_s^\pm(v_x, v_y, v_z, E_I) &= \frac{n_k}{(2\pi kT_k/m)^{3/2}} * \frac{E_I^{(j/2-1)}}{\Gamma(j/2)(kT_k)^{j/2}} \\
 &* \exp\left[-\frac{2E_I + m((v_x - u_k)^2 + v_y^2 + v_z^2)}{2kT_k}\right] \\
 &-\infty < v_x, v_y, v_z < \infty
 \end{aligned}$$

(2.41)

Where T_k is the Knudsen layer temperature and n_k is the gas number density in the Knudsen layer.

According to Kelly and Dreyfus, in order to arrive in a time of flight situation from the velocity distribution function, firstly the bombardment area and detector must be small with respect to their spacing, secondly the detector is normal to the target surface, and finally the laser desorption time is much less than the flight time.

If the detector is located at a distance “x” perpendicular to the target surface, the “y” and “z” directions are parallel the target normal, it can be assumed that $y=z=0$ and that the signal detected by the ion probe, at a position x , is flux sensitive. The nature of the x -axis orientation gives $|dv_x| = xdt/t^2$. Provided the Knudsen layer thickness is much smaller than the flight distance, the resulting time of flight problem is adequately solved using the general form:

$$\text{time of flight signal} \propto x^2 t^{-5} \exp\left(-\beta_s^2 x^2 / t^2\right)$$

where β_s^2 stands for $m/2kT_i$.

(2.42)

With x , the distance from the target to the detector, m is the mass of the ion, k is the Boltzmann constant and T_i is the ion temperature determined by the total width of the flight time distribution.

However if the Knudsen layer is significantly large in comparison to the flight length there is a need for the re-introduction of the Knudsen layer, producing:

$$\text{time of flight signal} \propto x^2 t^{-5} \exp\left(-\beta_k^2 (x - u_k)^2 / t^2\right)$$

(2.43)

Where u_k is the average centre of mass velocity.

2.12 Ion Probes:

In 1926 [55], Mott-Smith and Langmuir published their well known paper on the use of electrostatic probes to measure the properties of a steady, collisionless plasma, in which the electron energy distribution is considered Maxwellian. The experimental setup for an ion probe is relatively simple, making use of a conducting object, which is inserted into the plasma and

connected to external circuitry, at the exterior of the chamber, via a vacuum feedthrough.

The use of electrostatic probes in a flowing plasma was further developed by Koopman, firstly using a ruby laser to generate a “plasma ball” expanding into an ambient plasma [56], and secondly studying the density, velocity, electron temperature and ion temperature in streaming plasmas verifying the operation of Langmuir probes in such conditions [57].

A schematic diagram of a typical Koopman circuit used for a flowing plasma is shown in figure 2.8. The operating principle of the circuit is that of generating current-voltage characteristics, therefore a variation of the probe voltage results in a variation of the recorded current. The charge collected by the probe must be much less than the charge stored in the blocking capacitor, once this condition is met transitory currents from the plasma will cleanly reach the oscilloscope, failure to meet this condition and the consequences are that of a long discharge of the capacitor giving un-reliable results.

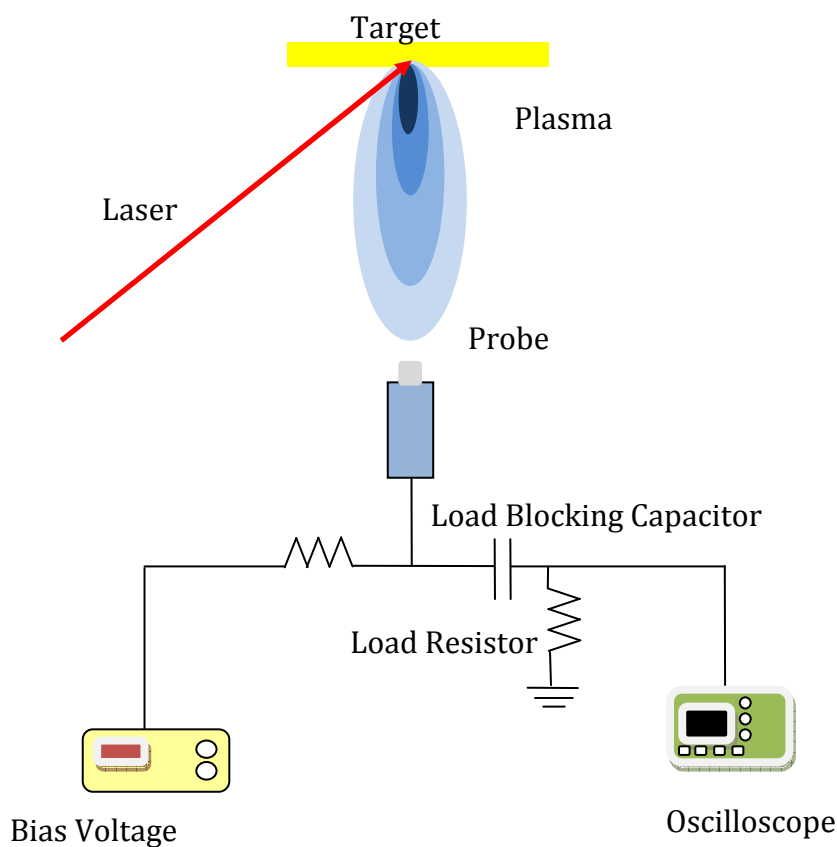


Figure 2.8: Schematic diagram of a typical Koopman Circuit.

The ion probe used in our setup consisted of a 5x5 mm conducting “collector” plate protruding from a grounded collar with an insulating layer separating both. The capacitor used was 1 μ F, with a circuit resistor of 100 k Ω . The load resistor used was that of the internal resistor of the oscilloscope, 50 Ω .

Another condition which must be met is that the probe tip must be able to endure the heat from the plasma, with a physical size that is small compared to the typical length of the plasma. Also the probe must not agitate the plasma. The most difficult condition to satisfy is that of the perturbation of the plasma. Unlike magnetic probes, which are considered non-local in nature, implying the local perturbation of the plasma can be ignored, a particle flux measurement is fundamentally local and therefore an understanding of how the locally perturbed plasma relates to the unperturbed plasma is important in ion probe measurements [58].

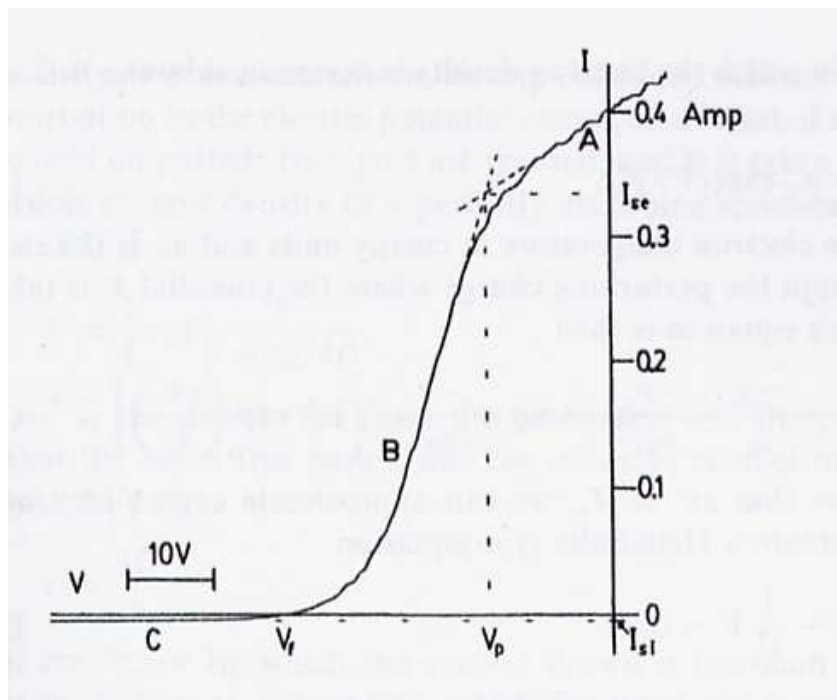


Figure 2.9: Electric probe characteristics showing how the probe current varies with probe potential[58]

Figure 2.9 shows the IV characteristics of the probe current, varying with probe potential, with three distinct regions.

Region “A” is known as electron saturation region, with I equal to the electron-saturation current. This arises when the voltage applied to the probe is

much larger than the plasma potential V_p , essentially the electron current cannot increase any further due to this already being maximised, with all the electrons arriving collected. Note that in this diagram, no zero is indicated on the voltage scale as we do not know the plasma potential with respect to, for example the grounded walls of the chamber.

Region “B” is given when the probe voltage is less than the plasma potential, it is known as the electron retarding region. When the electron current is equal to the ion current, we reach V_f , the floating potential.

Decreasing the probe potential further we enter region “C”, the ion saturation region, where only ions are collected.

2.13 Mass Spectrometry:

Mass spectrometry is an analytical technique that measures the mass to charge ratio of ions formed when a molecule or atom is ionised.

The development of mass spectrometry can be said to have began as early as 1886 when Goldstein [59] discovered positive rays in a low pressure electrical discharge tube. He observed luminous streamers passing through a perforated cathode, into the space behind. Wien then showed that these streamers were deflected by magnetic and electric fields proving that they were positively charged particles [60].

The instrument used for mass spectrometry has its origins in a device known as a mass spectrograph, an instrument that records the mass spectrum on a photographic plate [61]. For calibration purposes the usual technique was to use a phosphor screen, this allowed the effects of adjustments to be quickly observed, when employing the use of a phosphor screen the device was termed a mass spectroscopy. Once the instrument was properly adjusted, a photographic plate was inserted and exposed.

As the detection technique changed to that of an oscilloscope [62] the terminology also changed, with spectrometry used in place of spectroscopy to avoid confusion with spectroscopy of light.

During the 1940's with advances in electronics, mass spectrometers became a convenient tool for the analyses of charged particles, playing a pivotal role in the discovery of new isotopes and in determining their relative abundances and accurate masses. A famous example of this is the Manhattan project which used a type of mass spectrometer known as a calutron [63] to separate the isotopes of Uranium. The variation between an ordinary mass spectrometer and a calutron is in its use, with the calutron designed specifically to harvest large quantities of known isotopes.

The time of flight mass spectrometer with pulse extraction was developed by Wolff and Stephens during the 1940's and 1950's [64], with double - focusing high-resolution mass spectrometers finding their market in accurate mass measurements of a variety of compounds.

The fundamental requirement for the mass spectrometer is that the material be charged; then, if a charged particle is situated in an electric field, it will accelerate in a direction opposite to that of its own polarity; this is the extraction of the charged material. The mass spectrometer then separates the ions by their mass to charge ratio (m/z). For the case of a time of flight mass spectrometer this is done simply due to the fact that the same kinetic energy is imparted on all particles, those with smaller masses will then fly more quickly than those of a heavier mass. The ions are then detected qualitatively and quantitatively by their respective m/z and abundance. The mass to charge ratio is calculated from the atomic mass number of a given element and the number of times the element has been ionised "z". One may ionise thermally, by electric fields or by impacting energetic electrons, ions, photons, energetic neutral atoms or heavy cluster ions into the material to be analysed [65]. For the purposes of this thesis, the ionisation technique is that of laser ionisation, i.e. the impact of photons.

The mass spectra acquired, usually consists of a large number of peaks, with the only knowledge to begin with, being that the peaks have their origins in the ionised material. The usual situation for organic chemistry, where the vast majority of mass spectrometers are currently used, is that the charge is equal to one and clusters, that is, molecules with mass number equal to two or more, make up the spectrum. However in our situation, as we will see later, this is not the case with multiply charged states more common for our laser ablation. The most intense peak of a mass spectrum is named the base peak, with the general representations of mass spectra normalising this peak to 100% intensity. This normalisation can be performed as the relative intensities are independent from the absolute ion abundances registered by the detector [66].

Reflection Time of Flight Mass Spectrometry (ReTOF MS) has its origins in Time of Flight (TOF) MS, a method in which ions are accelerated by an electric field of a known strength. The result of this acceleration is that all ions, of the same mass and charge, have the same kinetic energy. The velocity of the ion depends on the ratio between the mass and charge, with heavier particles travelling slowly and lighter particles, i.e. a small mass or one which is highly ionised moving quickly, fig 2.10.

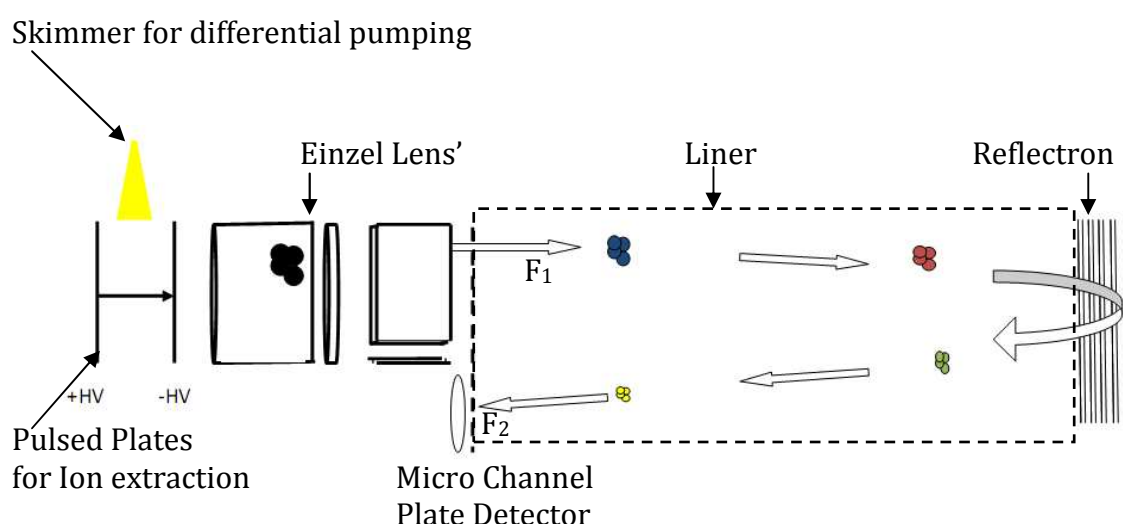


Figure 2.10: Mass separation in a ReTOF Mass Spectrometer.

The ion in the extraction region has a potential energy,

$$PE = qV$$

(2.44)

Where q is the charge and V is the electric potential.

An acceleration of this particle results in this potential energy being converted to a kinetic energy.

$$PE = qV = KE = \frac{1}{2}mv^2$$

(2.45)

Where v is the velocity of the ion, and m is the mass.

Considering three ions, of the same mass to charge ratio in the extraction region, where a pulsed high voltage is applied to the extraction plate to push the ions into the flight tube and an extraction grid usually connected to ground is opposite this pulsed plate. The ion closest to the extraction grid will leave this region first but will have the slowest velocity, the ion closest to the pulsed plate will leave last but will have the highest velocity. At some point, the faster ions which started late will just catch up with the slower ones, this point is known as the primary focus point.

It can be seen that if the detector could be located at point F_1 , an optimal resolution would be obtained as the width of the ion packet would be at its narrowest point. Unfortunately, the distance F_1 in most instruments is only 100 mm or so. This is not enough flight time for peak separation to occur. Therefore, the peaks although narrow, would overlap each other in time. For the remaining 90% or so of their flight time, the faster ions will continue to run away from the slower ones. This will cause the width of the ion packets to grow larger. This characteristic of short focal length is the principal limitation to the maximum resolution that can be obtained in a simple linear time of flight instrument. The focal length can be increased by adding other lens elements;

these elements have the same effect as increasing the head start of the slower ions.

During the flight of the ion through the liner, fig 2.10, the velocity should not change,

$$v = d/t$$

(2.46)

Where d is the length of the flight tube and t is the flight time.

Adjusting this equation will result in the form:

$$t^2 = \frac{d^2 m}{2Vq}$$

(2.48)

Of which d and V are both constants, resulting in the relation [66]:

$$t^2 = k \frac{m}{q}$$

(2.49)

Where k is a proportionality constant.

From the time of flight, t , a plot of the mass of the particle in atomic mass units (amu) versus t^2 , will result in a linear plot, the slope of which can be used to fit curves of unknown species.

It has been shown that poor mass resolution is obtained when only one field is used to accelerate the ions, i.e. without the use of a reflectron, fig 2.10 [67]. Due to the nature of the pulsed ion source, most time-of-flight mass spectrometers employ more than just a single accelerating stage. Wiley and McLaren [68] showed that the effects of initial spatial separation of the ion packets could be minimised for a given arrangement of accelerating fields by application of an electrostatic focusing lens, known as an einzel lens, with

optimum focusing conditions achieved by using two accelerating regions to extract the ions into the field-free region, known as first order focusing.

To even further increase the resolution of TOF mass spectrometers, many scientists in the 1950s–60s tried to design ion sources with smaller energy spreads, however no substantial progress was made. B.A. Mamyryn recalled, in his review of mass spectrometers [69], that his point of view on this subject was to devote efforts not to combating the energy spread but rather to neutralise their effect outside the source. His analogy was that of children’s games, whereby he wondered “whose ball thrown upward would fly the longest”, leading to the idea of decelerating electric fields, and ultimately the “reflectron grid” in a ReTOF [70].

The so called “reflectron” is, put simply, a correcting device used to account for the initial spread of ions in the extraction region. The ions enter the extraction region and are extracted by a uniform e-field which imparts the same kinetic energy on all ions, however the e-field is created by two conducting plates some distance apart. This separation of the two plates creates an error in the detection of ions, unnecessarily broadening the mass peaks. The reflecting assembly consists of an entry grid, kept at the same potential as the flight tube, then the first repelling grid followed by several plates giving a uniform repelling field, which prevents the scattering of ions and loss of sensitivity.

When a reflector is used, ions from the source converge until they reach the primary space focus they then diverge until they penetrate into, and are stopped in the reflector. They are reflected, and then converge on the way to the secondary, or reflected focal point. Placing the detector at this point has the same benefit to resolution as it did at the primary focal point. The flight times are longer in this case, which allows for adequate peak separation.

If a packet of ions enter a decelerating field, whose energy potential grows as $V_U = ax^2$, where “a” is a constant, and “x” is the position within the decelerating grid taken as the distance from the beginning of the field to that position, “x”. The time, t, to stop an ion with energy qV_U in this field is given by:

$$t = \int_0^{x_{max}} \frac{dx}{\sqrt{\frac{2q(V_U - ax^2)}{m}}} = \frac{\pi}{2\sqrt{2qa/m}}$$

(2.50)

Where q is the charge and $x_{max} = \sqrt{V_U/a}$ is the position the ion stops [69].

From this equation it is clear that the ion time of flight in the decelerating field, taken from the instant the ion enters the field to leaving the field (equal to $2t$), does not depend on the initial ion velocity. Therefore if a packet of ions of a given mass but having slightly different initial energies, due to slightly different starting positions in the extracting region, reach the detector having exited this reflecting field, the instrument resolution should only be determined by factors other than the initial errors generated by the extraction field. The reflector has the ability to both increase the focal length, and to compensate for energy distribution. If two molecules of the same mass have different axial velocities when they are ionized, the reflector will compensate for an energy difference. At the same time it compensates for the difference in energy which is due to a spatial distribution.

It can also be used for energy separation by allowing the more energetic ions to crash, or pass through.

Chapter 3:

EXPERIMENTAL DEVELOPMENTS

3.1 Experimental Design, Field Emission:

In the design of a field-emission system a few initial criteria need to be met. Firstly there is a need to obtain high vacuum; the presence of background gas will lead to an ionisation of this gas by the intense electric fields generated in a field emission experiment. This ionisation would be seen as arcing between the anode and cathode, damaging the samples, or if somehow gone un-noticed could lead to inaccurate results.

A stainless steel CF vacuum chamber was used for the field emission experiments and is shown in figure 3.7. The system was equipped with a 500 l/s BOC Edwards EXT501 turbomolecular pump, with a BOC Edwards RV18 oil diffusion backing pump. This RV18 pump evacuated the chamber, or “roughed the chamber” through the turbomolecular pump at a rate of 18 m³/h. An active pirani gauge was positioned on the chamber and connected to the turbomolecular pump controller. This pirani gauge has a pressure setting which can be adjusted for the automatic commencement of the turbomolecular pump. This setting was fixed to 1x10⁻¹mbar, so when the chamber pressure is sufficiently roughed by the RV18 pump, the EXT501 turbomolecular pump would begin. Due to the fact that the pirani gauge was connected directly to the control unit of the turbomolecular pump, this gauge could not be used to monitor the chamber pressure. Therefore a second pirani gauge was attached to monitor the chamber pressure down to 1x10⁻³mbar and a third pirani was attached between the RV18 pump and the turbomolecular pump to ensure efficient backing pressure. Finally when the chamber pressure passed the pirani gauge range an active inverted magnetron gauge was used to monitor the pressure to the base pressure of the chamber, ~5x10⁻⁷ mbar.

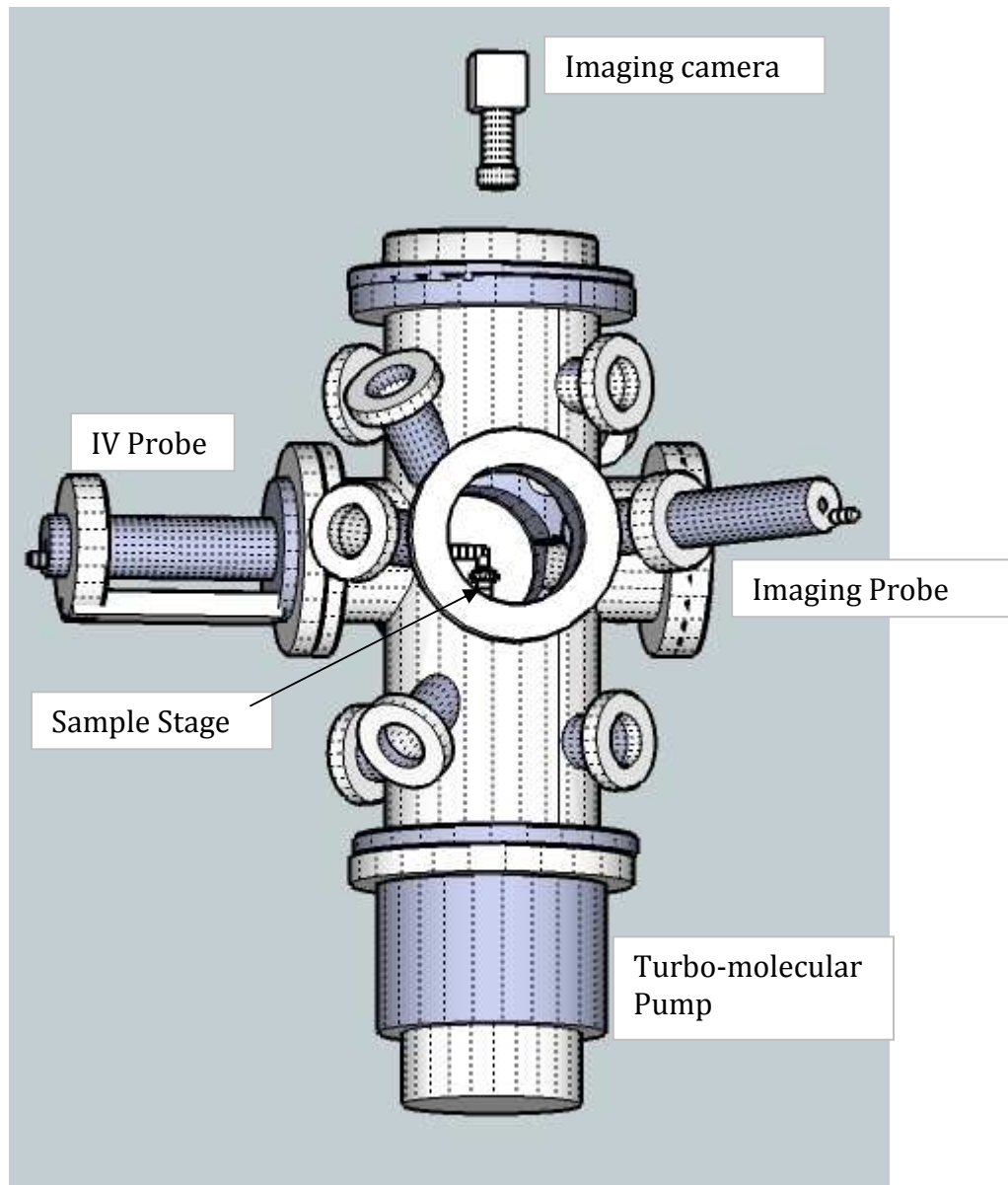


Figure 3.7 Field Emission Apparatus

3.1a System Layout:

Once a good vacuum system was functional, the inside of the chamber needed to be organised and designed. The electrons move by tunnelling, across a vacuum gap, in the presence of a strong electric field. There was a need to accurately apply a high voltage across a known distance and measure a current.

It was decided that for optimal measurements it would be best to have two voltage probes, one, a sturdy metallic probe used for IV characteristics, and the second, a relatively fragile probe used for imaging the emission sites of the

sample, fig 3.8. We configured the system so as the sample would be in a horizontal orientation. This would allow for easy positioning of both the sample and spacer to be used. The use of two voltage probes meant that it would be necessary to be able to withdraw these probes without venting the system; it also meant that the sample would require vertical movement so as to be clear of the probes during repositioning.

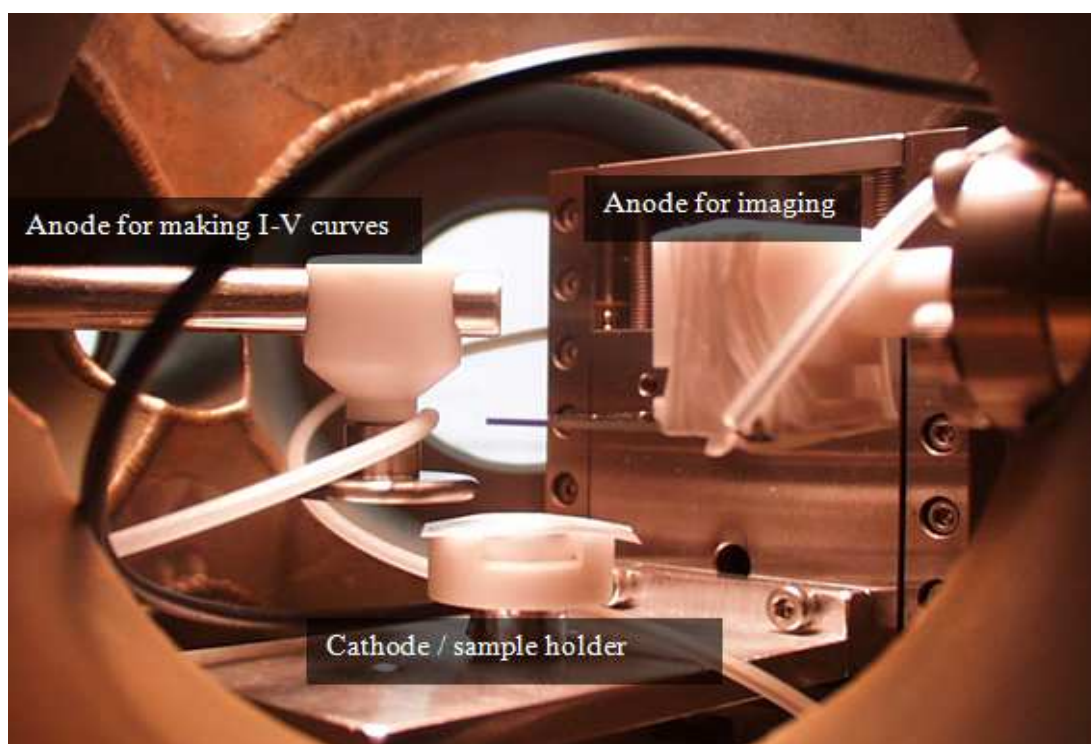


Figure 3.8 Internal view of Field Emission Apparatus

We used a stage which has the ability for vertical motion, the main problem with this stage for a field emission experiment is that it is metallic and would therefore attract electric fields. To solve this we placed the sample away from the stage on an insulating base, but we also needed to be able to make electrical contact to the sample.

The sample was placed on a Polytetrafluoroethylene (PTFE) stage which could move up to meet either of the two probes. This PTFE stage was made from two PTFE blocks. The first block is a simple 12mm diameter circular rod of 10mm height, with a 1mm diameter clearance hole through its centre. The second was made from one piece of Teflon with the bottom section having a diameter of 15 mm and 10 mm high. Above this section is a 30mm diameter

circular shape, with a 12mm diameter circle hollowing its centre to a depth of 10mm. There is a clearance hole from the exterior of the tower to the centre of this hollow made at an angle of 45° from the vertical. Putting the two pieces together gave a clearance from under the “ledge” to the top flat of the PTFE block where the sample would sit; this clearance allowed for an electrical connection through the Teflon block, but which, via a back contact to the sample, would not be seen directly by the electric field therefore we could be confident that all the signal would be due to the sample surface.

For imaging purposes a glass anode with a triple structure was employed, fig 3.9. It composed of a ZnO layer, on a phosphor layer, on another ZnO layer all deposited onto a glass substrate (see appendix c). This substrate was attached to a CF 40 Z-direction only manipulator. A Teflon bar was attached between the manipulator and probe for safety reasons.

Unfortunately the two probes had to be positioned at different heights but the ability of the sample holder to move up and down allowed for this without any problems.

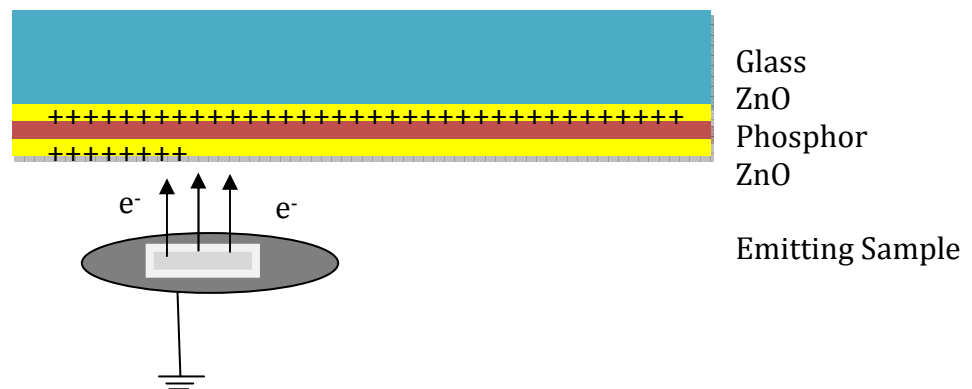


Figure 3.9, Field emission imaging probe

3.1b Electrical Design:

For the electrical design, it had to be safe to work with high voltages but also had to be able to accurately apply a known voltage and accurately measure a current. We knew there was a good chance of breakdown inside the chamber

during initial setup, so there was concern about protecting the picoammeter, used to measure current, from damage.

The circuit to protect the picoammeter was designed with a series of current limiting resistors and two opposite facing, low leakage, fast response time, diodes. These served to bypass the picoammeter in case of a sudden surge of current.

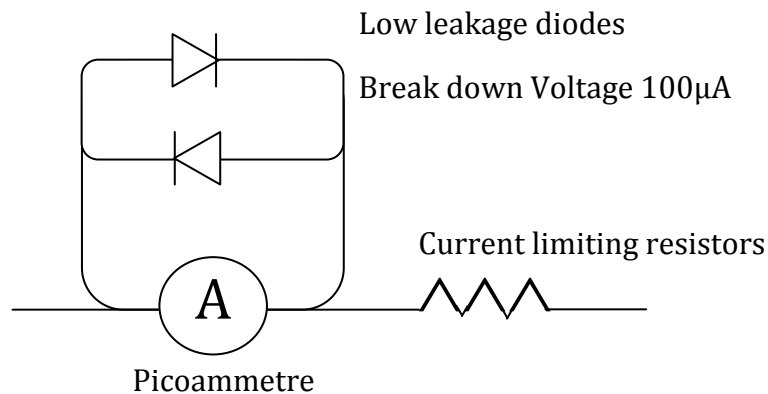


Figure 3.10: Protection circuit for the picoammeter

After several attempts the best design was found to be that of reading the current from the sample side, fig. 3.11. The only issue with this is that the sample is not connected directly to ground, and therefore is floating.

If we consider a current reading of $400\mu\text{A}$, and that the current limiting resistors add up to $231\text{K}\Omega$, if ohms law is applied, $V=IR$, the voltage “seen” by the sample will in fact be 92.4V lower than the voltage which is actually applied to the circuit, as the sample now sits at this voltage above ground.

The samples tested are the electron emitters, therefore these act as the cathodes. The sample was connected to ground via a back contact of silver paste (SPI Supplies® Silver Paste Plus™); for this reason a conducting substrate is preferred, although semiconducting substrates suffice as the resistance through a semiconducting substrate will be substantially less than the resistance through the vacuum.

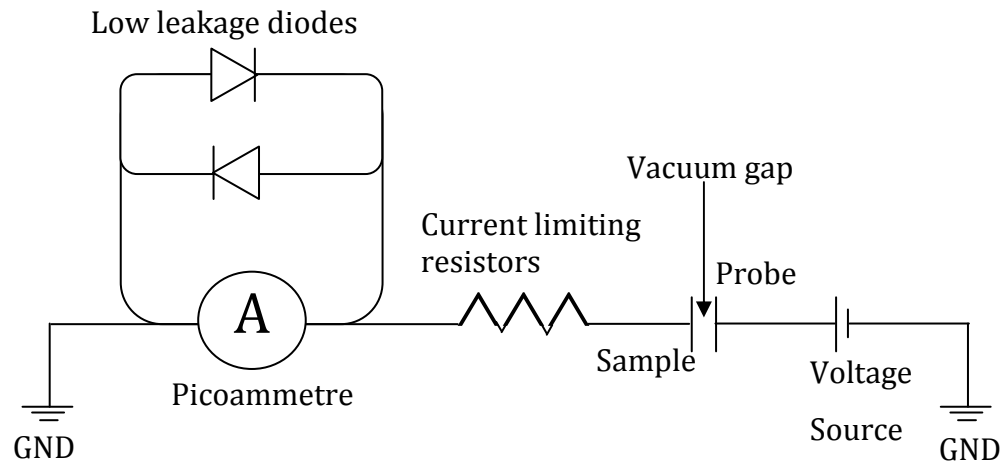


Figure 3.11:Electrical design of Field Emission system

For current-voltage characteristics a high voltage is applied to the flat aluminium electrode, as seen in fig 3.8. The distance between the anode and cathode was kept constant at $100\mu\text{m}$ by a PTFE film (630-643-79 Goodfellow Cambridge Ltd.), which was punctured with a circular hole punch to expose the substrate surface. From practical experience it is worth noting that the hole punch will create a raised edge in the film, this edge needs to face the substrate or else it could lead to “edge effects” generating a signal from the PTFE spacer. When the electric field is high enough it is comparable to a switch being closed, the electrons begin to flow across the vacuum gap and a current can be measured, this “switching on” of the circuit is the initial turn on field whereby a good emitter has a low turn-on-field.

For the high voltage power supply we used two different sources, a manually controlled Bertan high voltage, low current power supply for the imaging probe and one of only two pieces of equipment which were specifically bought for the field emission system, a Stanford Research PS350 high voltage power supply with a GPIB interface. The maximum output of both power supplies is a voltage of 5 kV, with a maximum output current of 5 mA. In order to measure the current we had available a Keithley 6485 picoammeter which also has a GPIB interface.

The second piece of equipment which was specifically bought for the field emission system was the camera used for imaging the emission pattern. This is an Artcam-150PII, 1.5M pixel monochrome camera, positioned ~300mm above the sample.

3.2 Field Emission Computer Interface:

The final part of the field emission setup was to interface the voltage source and picoammeter with a computer. Both pieces of equipment have GPIB interfaces and a National Instruments IEEE 488.2 card was used to interface to the computer. The “Labview” software was used to control the equipment.

Below in figure 3.12, the front panel of the Labview program is shown. The panel is split into windows with, in anti-clockwise order:

- The instruments initialize panel with SRSPS350 being the voltage source located at GPIB 14 and KE 6485 the picoammeter located at 13.
- The enable window to set the high voltage setting “on” and check the zero level line on the picoammeter.
- The errors window, which describes any errors such as incorrect GPIB location of device, high voltage not enabled etc.
- The next window is the file path location of the saved voltage and current data along with a define window for how many decimal places are desired in the saved data.
- The integration time is the maximum length of time in which to allow the read operation to complete.
- The next window is to define the voltage step taken by the voltage source, the starting voltage, usually +50V, and the wait time for the current reading at the set voltage.
- Finally there is the output display of the voltage and current readings, as well as the setting for the “trip value current” in case of arching and the high limit for the voltage, i.e. the high voltage setting at which the voltage stops and starts to descend back down to the initial starting voltage.

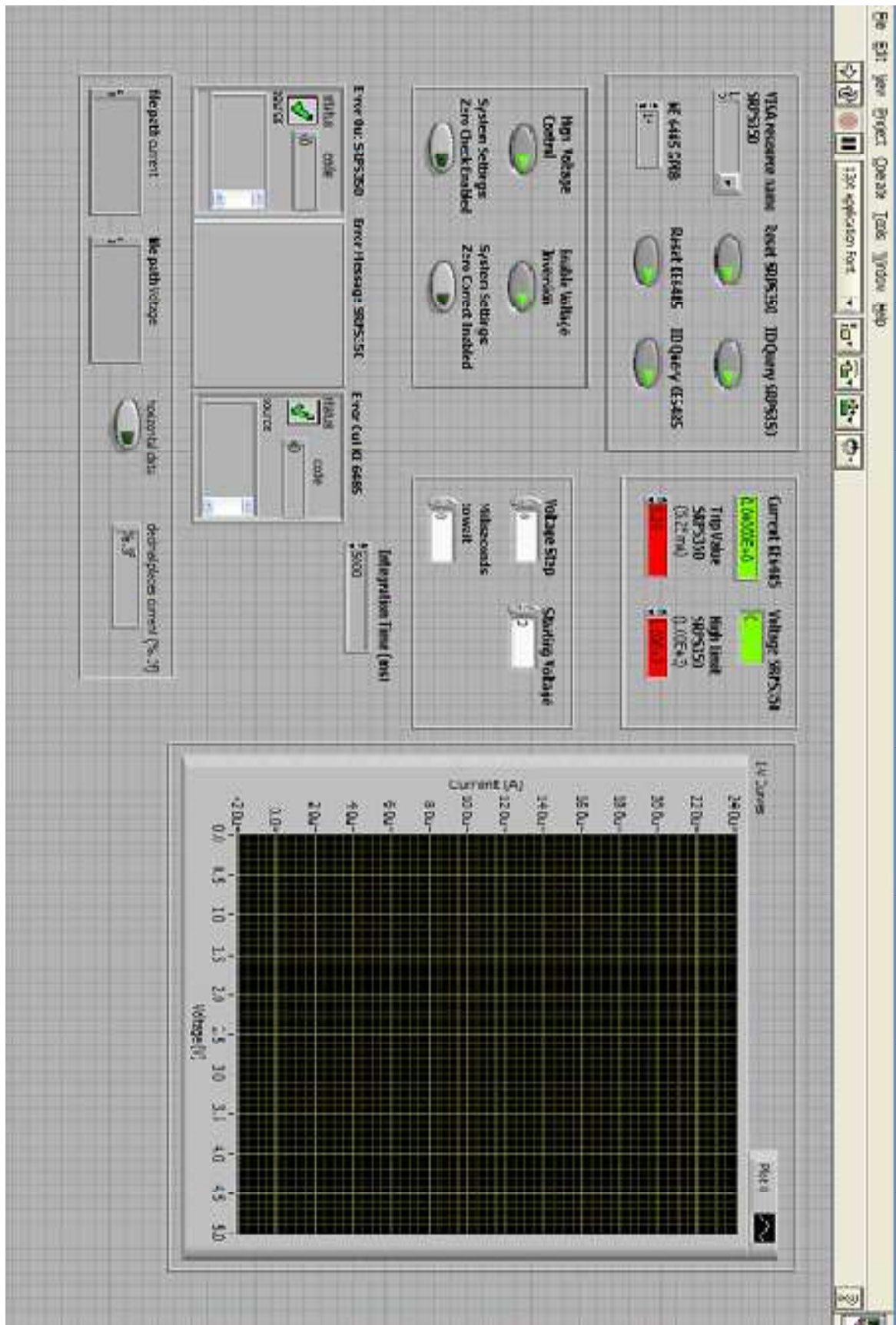


Figure 3.12: Computer controlled front panel of SRSPS350 communicating with KE6485

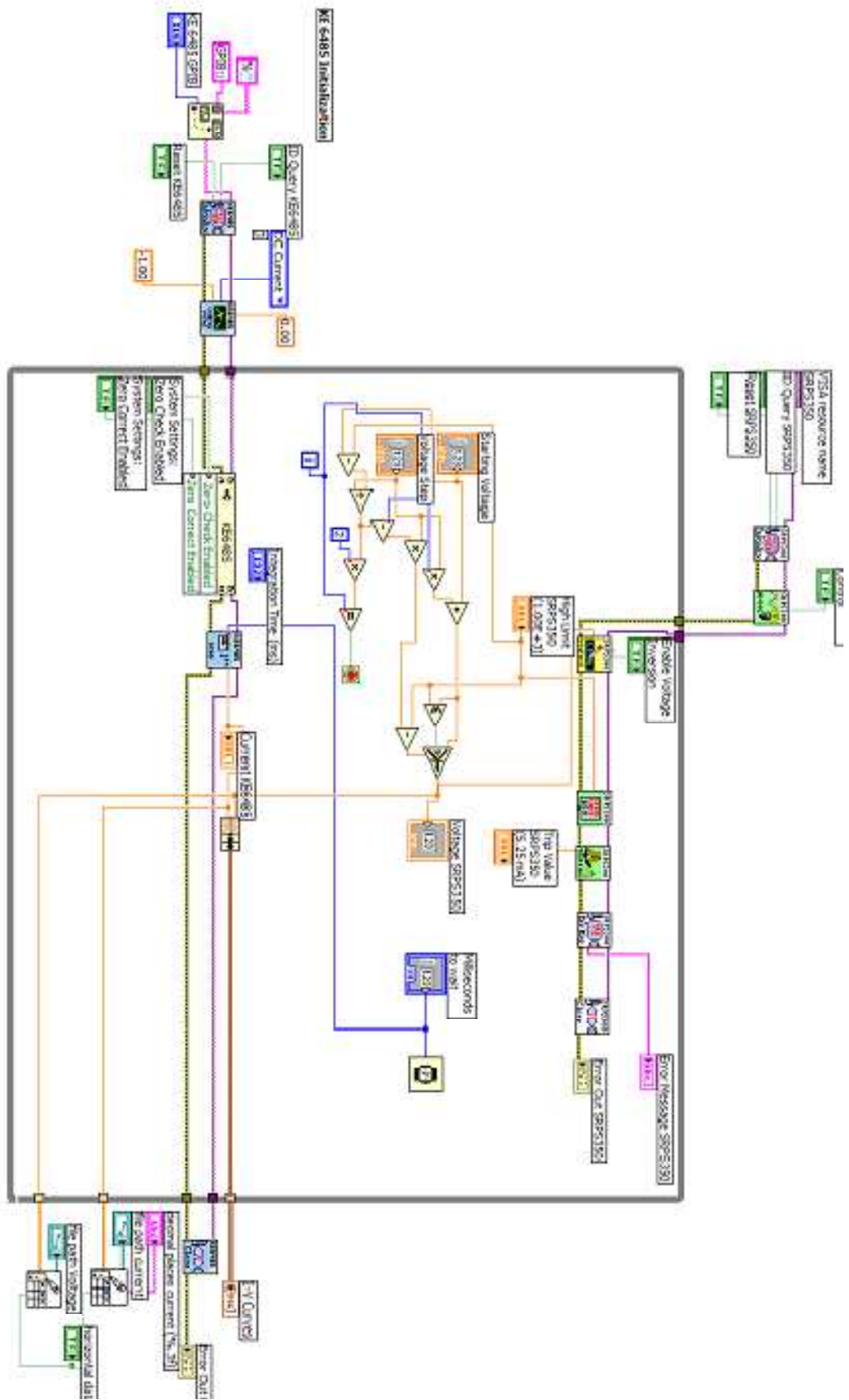


Figure 3.13: LabView VI of SRSPS350 communicating with KE6485

3.3 Experimental Design: ReTOF System:

The first step for the plasma diagnostic system was to start the design and development of a new laboratory facility to probe the properties of laser produced plasmas, namely by integrating a ReTOF mass spectrometer into the experimental setup.

The main supporting table for the time of flight mass spectrometer was a steel frame recycled from a previous experiment, to secure the ReTOF in place. The main table for the system was extruded aluminium ordered from Flomax Ireland Ltd, this was chosen due to its ease of construction, recyclability and the possibility to expand the table should the need arise. This main table supported the main chamber (the plasma chamber) and connecting tee piece to the ReTOF. Finally a large steel table was used to support a 2x1 m optical table, onto which all lasers and optics necessary for the experiment were housed.

3.3a Vacuum Systems:

We decided the plasma chamber needed to be easily accessible with a large internal area for optics and deposition essentials, figure 3.14. A cylindrical chamber, 400 mm in diameter was chosen. It was equipped with a single CF 150 port, for connection to the tee piece of the ReTOF, 90° from this position in both the clockwise and anticlockwise directions are CF 100 ports and at each of the 45° from these positions are CF 40 ports. This gave quite a lot of flexibility to the layout. To enable easy access to the chamber, the whole lid could be removed; this was enabled by a large ISO connection.

A Leybold Turbovac TW250S (pumping speed of 250 l/s) turbo molecular pump was attached to the main interaction chamber via an ISO 100 flange at the bottom of the chamber. This was backed by an oil sealed rotary pump.

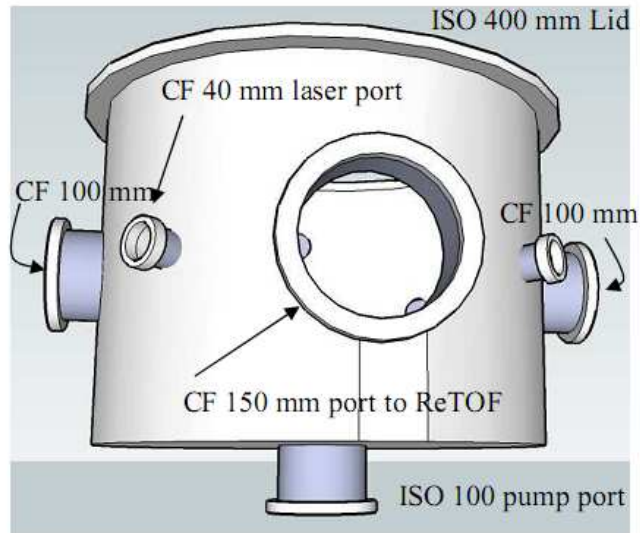


Figure 3.14 Plasma Chamber.

The next question to arise was the interface between the mass spectrometer and this chamber. Our first concern when connecting the ReTOF to the plasma chamber was the position of the so called “shroud”, in particular the exact position of the “skimmer”, the small orifice used for differentially pumping the ReTOF and allowing the ions enter the mass spectrometer from the plasma chamber. For this reason the positioning of the skimmer needed to be exactly in line with the flow of the plasma plume, so it required a custom ordered T-piece section of very specific lengths, figure 3.15. This Tee-piece was pumped, via one of the CF 40 mm ports, by a Leybold 50 l/s turbomolecular pump, which was backed by an oil sealed rotary pump .

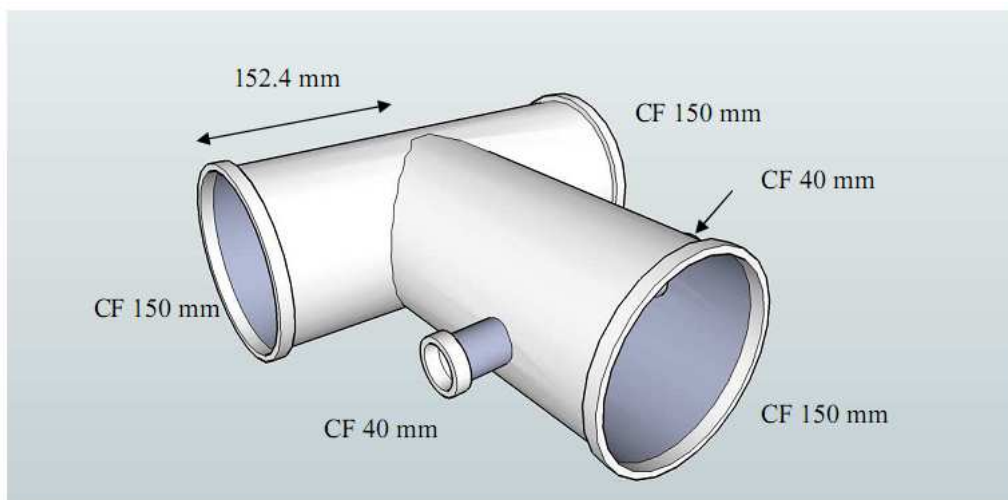


Figure 3.15. Specialised Tee – Piece connecting the ReTOF to plasma chamber.

The skimmer protrudes 152.4mm from the vacuum connection of the ReTOF system, figure 3.16. The ideal situation is that the skimmer be lined up exactly with the centre of the plasma chamber, therefore this exact length was specified for the tee-piece.

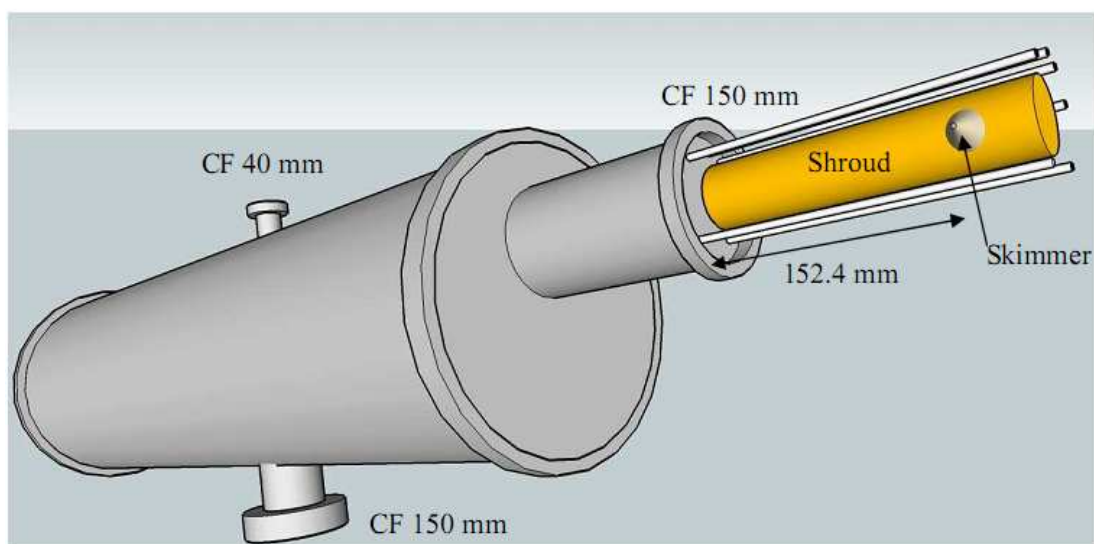


Figure 3.16 ReTOF mass Spectrometer

The ReTOF chamber is pumped by a Leybold TW 250 l/s turbomolecular pump, which is backed by an “Ecodry” oil free piston pump, this pump was chosen to keep the ReTOF as clean as possible. The skimmer in the ReTOF acts as differential pump feedthrough of 1 mm diameter. We required that the plasma chamber would have operating pressures as high as $1*10^{-2}mbar$, while the highest recommended pressure for operating the MCP detector was $1*10^{-6}mbar$. We also added a gate valve between the chamber and the tee piece. This gate allows venting of the chamber while keeping the TOF under vacuum, it was important to keep the MCP under vacuum as, if it were to absorb moisture from the atmosphere, it could easily be damaged during operation via arcing.

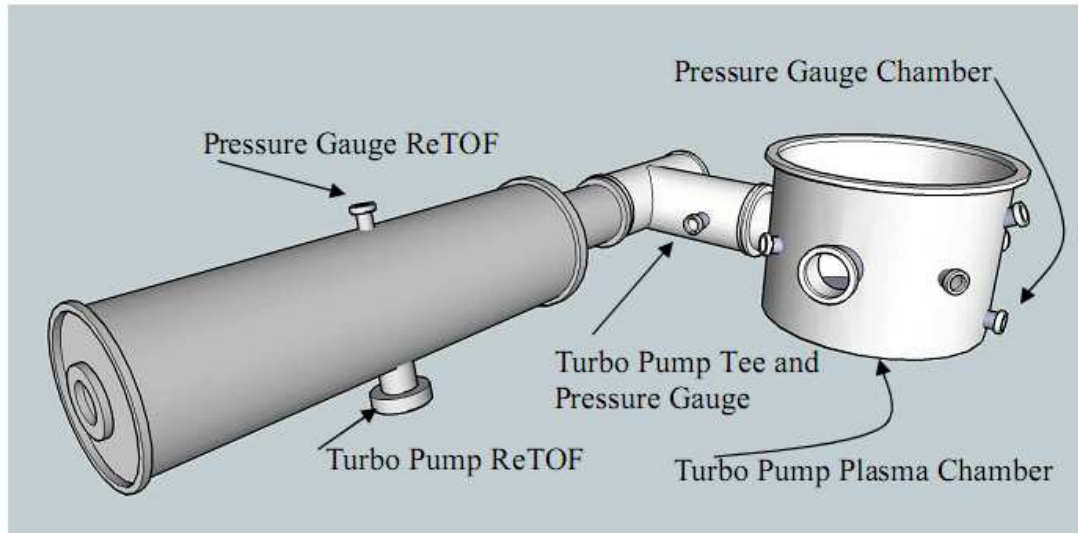


Figure 3.17 Experimental vacuum setup, Plasma Chamber coupled to the ReTOF.

In order to monitor the pressure in the system, we used three separate full range gauges. The base backing pressure was found to be $\sim 5 \times 10^{-3}$ mbar throughout the system, while with the turbo molecular pumps switched on, a base pressure of 3×10^{-6} mbar was achieved in the plasma chamber and T-piece, while 2×10^{-8} mbar was achieved in the RETOF. The turbo pumps on the plasma chamber and the ReTOF were also computer interfaced so as to have the ability to vary the pumping speed. This is of most importance for the plasma chamber with the regular introduction of gases for the deposition of materials, and the analysis of laser produced plasmas in ambient atmospheres.

Once the vacuum testing stage was complete, a motorised target system needed to be put in place. We decided on two types of target mount, firstly a lateral motion, computer controlled motorised stage, Thorlabs high precision motor Model: T25X, was placed in the centre of the chamber on a base plate. The base plate was machined from an aluminium plate, with M6 screw bore holes made every 2.5 cm apart. Next, for vertical motion, a second Thorlabs high precision motor Model: T25X was mounted at 90° on the first stage, this assembly enabled 25 mm of movement giving both the vertical and lateral movements needed for experiments generally involving flat, square targets, usually no more 25*25*1 mm. When using disk targets, the vertical motion stage was replaced by a stepper motor, this would rotate the target after each

shot. A combination of both techniques; rotational and lateral, or vertical and lateral; allowed each shot to impinge on a fresh surface, ensuring no cratering or pitting would occur.

Next a mass flow controller, Analyt GFC, with a calibration for O₂, was installed. This allowed for a flow sensitivity of 1 sccm to be achieved into the chamber. The final part of the internal construction of the chamber was that of the sample holder for depositions. The holder was mounted on a rail so as variations in the sample target distance could be made. The samples were held onto the holder using a conducting paste, SPI Supplies Silver Paste Plus, which needed to be dried before the system could be pumped, usually ~30 minutes drying time. The actual sample holder was that of a silicon carbide element which could reach temperatures of ~800° C at the tip. Power was supplied to this element via an external current source, with temperature of the substrate checked using a pyrometer.

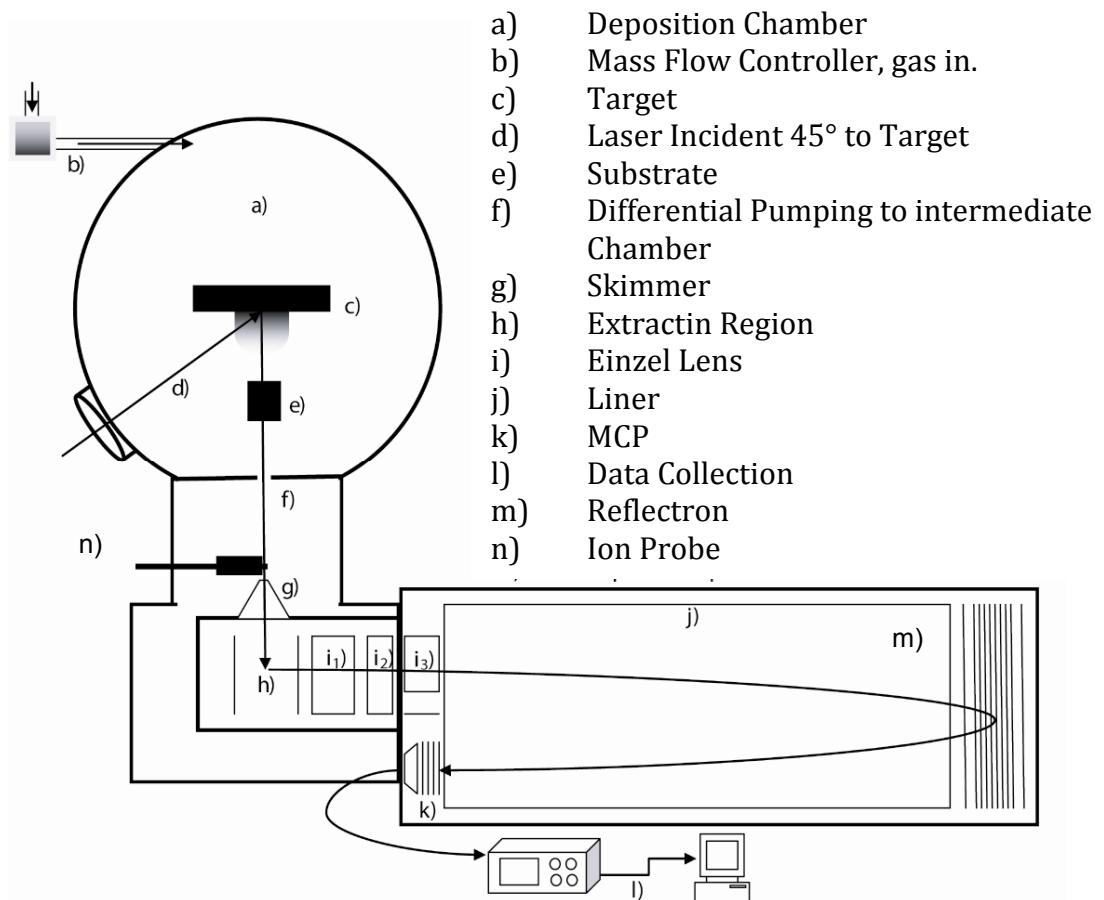


Figure 3.18: Layout of the Laser ablation system with in-situ ReTOF and ion probe.

3.3b ReTOF Set-Up:

The ReTOF was a standard system designed and built by R. M. Jordan (California, USA). The instrument consists of a shroud and skimmer, an ion source assembly, a reflection grid, a 40 mm dual micro-channel plate (MCP) detector, a liner and a flight tube, fig 3.18.

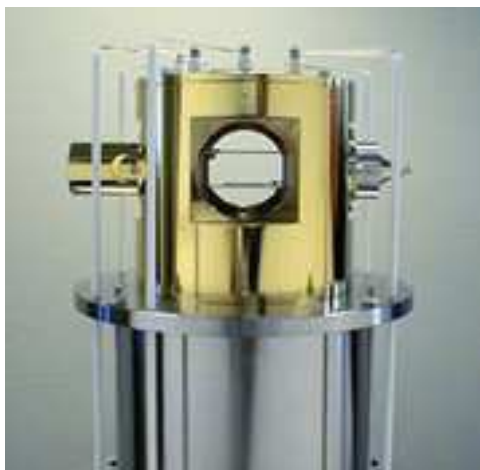


Figure 3.19 Shroud and Skimmer

The shroud is the golden part in figure 3.19, while the skimmer, (g) in figure 3.18, is the cone shaped metallic piece protruding to the far right hand side. This assembly is essentially to increase the resolution by allowing a differential pumping system, giving lower pressures in the TOF chamber, and feeding from the path of the ion source.

Underneath the shroud resides the ion source assembly consisting of the repelling plates, figure 3.18 (h), A1, the top plate and A2, the second plate with a circular aperture, figure 3.20. In normal operation, both of these plates are kept at ground and pulsed, A1 positive and A2 negative for extraction of the ions. The extraction pulse was generally as short as 100 ns, therefore making timing critical. This voltage pulse was generated by an external voltage source, a DEI products PVM-4150 pulse generating module. The minimum pulse width was 50 ns, with a capability of simultaneously generating two separate pulses up to

± 1500 V. The pulse width and delay timing was controlled by a TTL pulse from a Stanford DG535 digital delay and pulse generator.

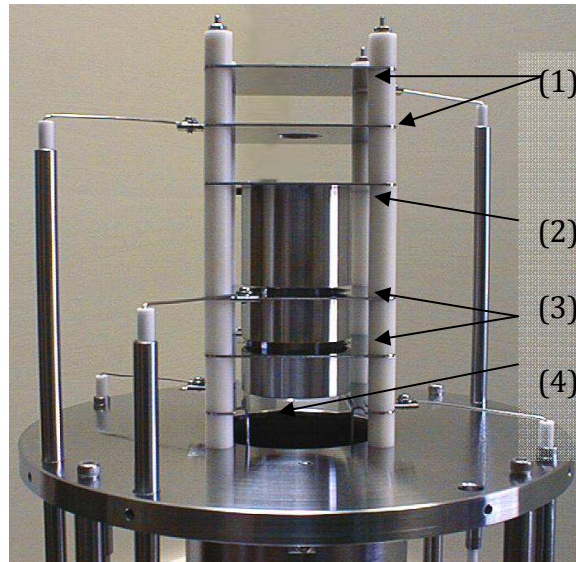


Figure 3.20 Ion Source Assembly

The next plate down, which is in fact a short tube, is an acceleration grid, (2), internally connected to the liner. Positioned after this is an Einzel lens (3) used to focus the ion beam, and finally a mass gate (4), which is essentially a box lens with three sides of the box internally connected to the liner and the fourth side connected to a separate voltage source, in order to supply a slight “kick” off axis to the ion bunch (I_3) figure 3.18.

The ions will exit this mass gate and enter the liner, which is in actual fact a cylindrical metal tube, isolated from the vacuum chamber, spanning the length of the flight tube, supplying a field free flight region to the ions. From this field free region the ions exit the flight tube into the reflectron.

The reflectron assembly, fig 3.21, consists of an entry grid, (top). Below this is the first repeller grid, followed by several plates, giving a uniform repelling field. So many plates are used to prevent ion scatter and loss of sensitivity. The ions are pushed back out of this grid, refocused, accounting for

any initial spread in extraction, and are sent towards the MCP for high resolution detection.



Figure 3.21 Reflectron Assembly

The ions should impact on the 40 mm Dual MCP detector. This detector provides gain of between 10^6 to 10^7 with sub-nanosecond rise times. Each ion impacting on the first plate of the detector will deliver $\sim 10^4$ electrons onto the second plate, these secondary electrons will give $\sim 10^4$ electrons. These then exit the second plate and hit an electrode at ground potential giving our signal.



Figure 3.22 40 mm Dual Micro-channel Plate Detector

The construction of the ReTOF firstly involved the assembly of the MCP detector. The MCP arrived in a separate housing to the rest of the system, it is

the most sensitive piece of equipment in the laboratory and needed to be attached at the rear end of the shroud. The shroud was then attached to the flight tube, and from the other end of the flight tube the liner was inserted. The liner required some modification, essentially a Teflon ring was made, in order to hold the tube ensuring bending would not occur. This had to be done to stop conduction between the liner and the outer walls of the chamber. Finally the reflection grid was inserted into the rear end of the flight tube.

3.3c Ion Probe:

The ion probe used for experiments presented in this thesis consists of a metal electrode exposed beyond an insulating casing and inserted just in front of the extraction region of the ReTOF mass spectrometer, ~55cm from the target, (n) in fig 3.18. This distance is unusually long for an ion probe TOF measurement, however, the main interest was the material entering the ReTOF and not the initial interactions close to the target surface. The electrical diagram was the same as that shown in fig 2.8. The probe bias was variable from -1kV, to attract ions to +1kV, to attract electrons. A 1 μ F capacitor was used with a 100 k Ω resistor connected to the high voltage power supply

The advantage of these probes is due to their simplicity, with all of the control in an external circuit, we may bias the probe positively or negatively, thus attracting electrons or ions.

3.3d Laser Systems:

Two Continuum Surelite laser Q-switched systems were used for the ablation in all experiments, with a lasing medium of Neodymium-doped: Yttrium Aluminium Garnet (NdYAG). A Surelite III-10 laser operating at its fundamental wavelength of 1064 nm only, and producing an energy of 800 mJ and a second laser, a Surelite I-10, with the capability of operating with the full four harmonics. This laser could produce a 1064 nm pulse, with an energy of 450 mJ, 532 nm, with an energy of 200 mJ, 355 nm, with an energy of 100mJ and finally a pulse at 266 nm producing an energy of 30 mJ.

The Full Width at Half Maximum (FWHM) pulsewidth of the Surelite III was measured as 6ns while for the Surelite I operating at its fundamental frequency was measured to be 6 ns and 4 ns when operating the harmonics. The output from both lasers was linearly polarised with a Gaussian profile.

The optical arrangement can be seen below, figure 3.23.

For the Surelite III, a half-wave plate was used to vary the degree of polarisation while a Brewster's window was used to separate the two directions, the "s" and "p" directions, of polarisation; transmitting one and reflecting the other. This variation in polarisation states was important for tuning the energy of the laser to impact the target.

In the case of the Surelite I, harmonic generating crystals, essentially a nonlinear optical material where the photons are combined to forming photons with twice the energy and half the wavelength of the original photons, are used to convert the wavelength of the emitted laser photons. The beam exiting the laser head will contain the original 1064 nm but also photons which possess the wavelength of the chosen harmonic. Then, dichroic mirrors are used to reflect the wavelength of the chosen harmonic and transmit any other wavelengths. The result of this process is laser emission of either 532 nm or 355 nm or 266nm. The half-wave plate is again used to vary the degree of "s" and "p" polarisation, while the cube polariser will transmit one of these states and reflect the other through 90°. Again the laser is reflected using mirrors to reach the target and the energy is again determined by the half-wave plate.

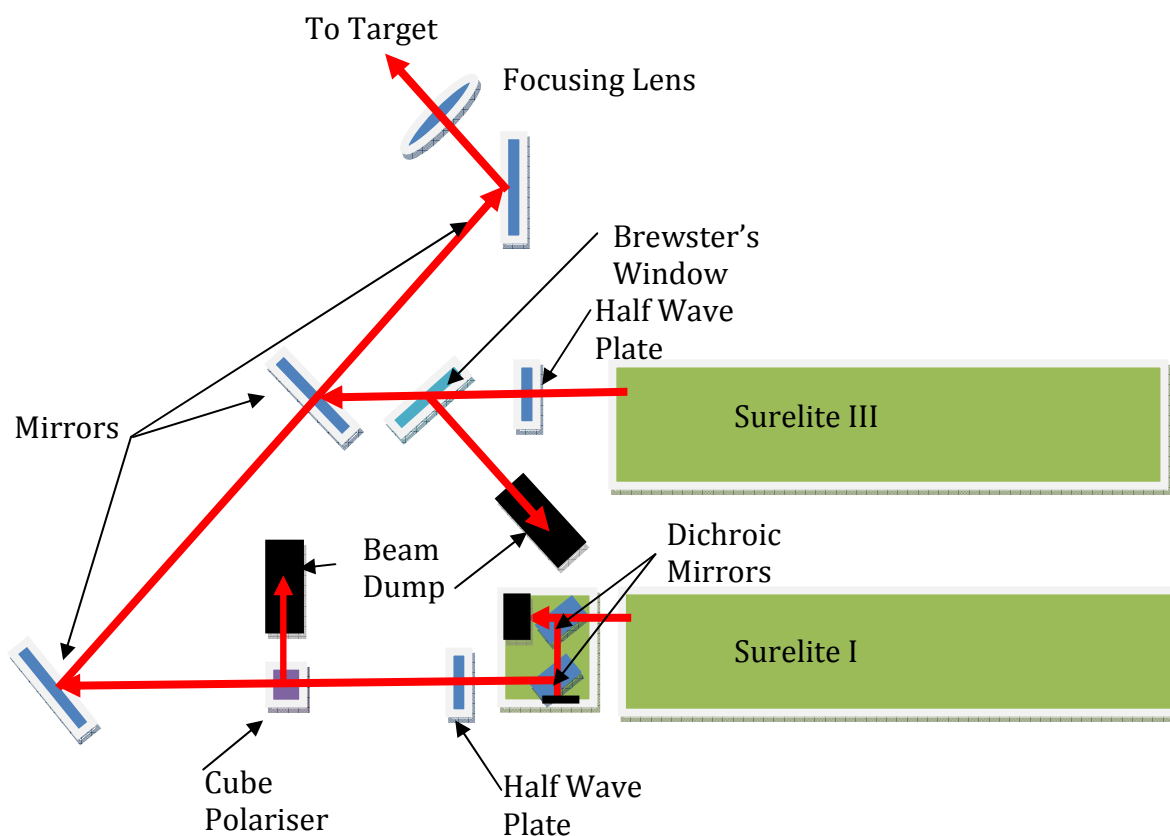


Figure 3.23 Optical Arrangement for Time of Flight Laboratory

The ablating laser beam is angled at 45° to the target normal, this allowed expansion of the laser produced plasma into the RETOF which is orientated normal to the target.

3.4 Electrical Design and Timing:

Timing plays a crucial role in our type of mass spectrometry, therefore exact timing was vital in setting up this experiment.

Simply, once the laser impacts on the target, a plasma is formed, the ions from this plasma expand down through the tee piece and reach the skimmer. Once passed the skimmer the ions are in the extraction region of the ReTOF, where they were extracted down the flight tube by a pulsed electric field.

The Surelite I and Surelite III both operate their flash lamps at 10 Hz, which can be set to trigger internally or externally. For all experiments carried out, the lasers were set to trigger externally via a Stanford DG535 delay generator. This delay generator then constituted the master oscillator, generating a +5 V TTL pulse 10 μ s wide at 10 Hz, in order to trigger the flashlamps on the laser used for ablation. The starting time of this pulse was named T_{0a} , fig 3.24. A second output on the same delay generator was used to generate an identical TTL pulse 180 μ s after T_{0a} , this was the optimal time delay between the laser flashlamps and triggering the Pockels cell, the technique of active Q-switching used in the laser. Before being sent to the laser this second output was passed through an AND box, which had a second input arriving from a computer controlled TTL signal. Only when both inputs to the AND box were positive, would the TTL signal be sent to the pump laser Q-switch. A copy of this signal was sent to a second Stanford DG535, used to control the extraction of ionised material into the ReTOF.

For this delay generator, the incoming pulse from the AND box acted as the trigger, with two outputs used to control the ReTOF and data collecting oscilloscope. Firstly a +5 V TTL pulsed BNC, "AB", was connected to the pulsed plates of the ReTOF. "A" was varied with respect to the incoming pulse from the AND box. This "A" corresponded to the switching on of the voltage to be applied to the extraction plates. The "B" value was kept a constant 100 ns with respect to "A". This corresponded to the switching off of the voltage applied to the extraction plates and therefore was the extraction pulse width.

Next the second +5 V TTL pulsed BNC, "CD" was sent to the oscilloscope, to trigger the collection of data. "C" was equal to "A", and "D" was equal to "B". This pulse had the effect to make the starting time of the ReTOF measurement equal to the starting time of the ReTOF extraction, and not the starting time of the laser generating plasma. The reasoning behind this is as follows.

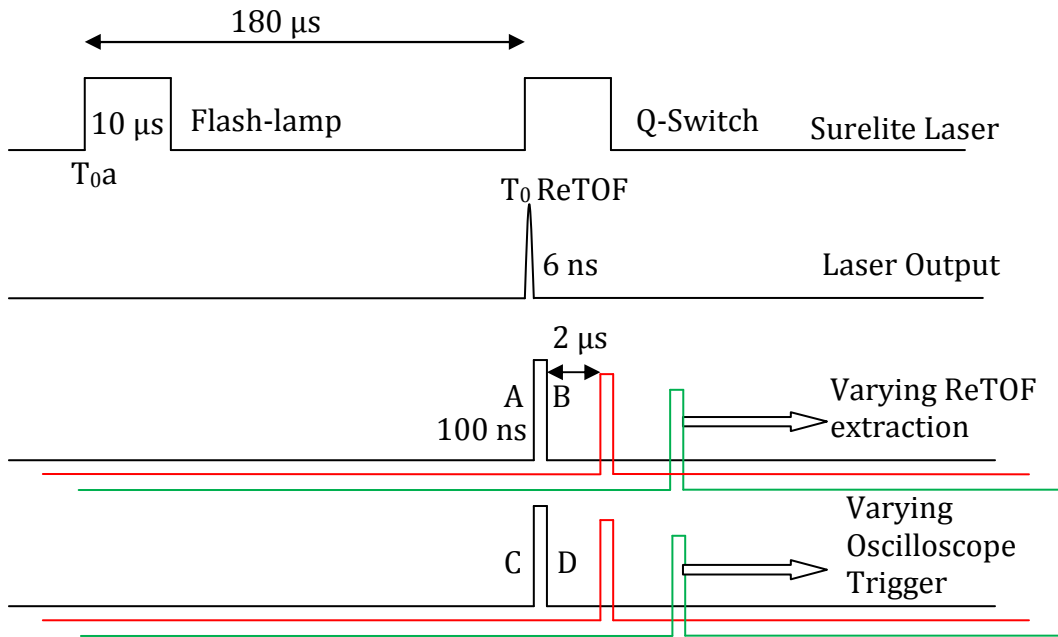


Figure 3.24 Timing Diagram

The ReTOF, as explained earlier, imparts the same kinetic energy on all ionised material that is extracted. A variation of the “AB” delay with respect to the firing of the laser results in a scan of an expanded plume.

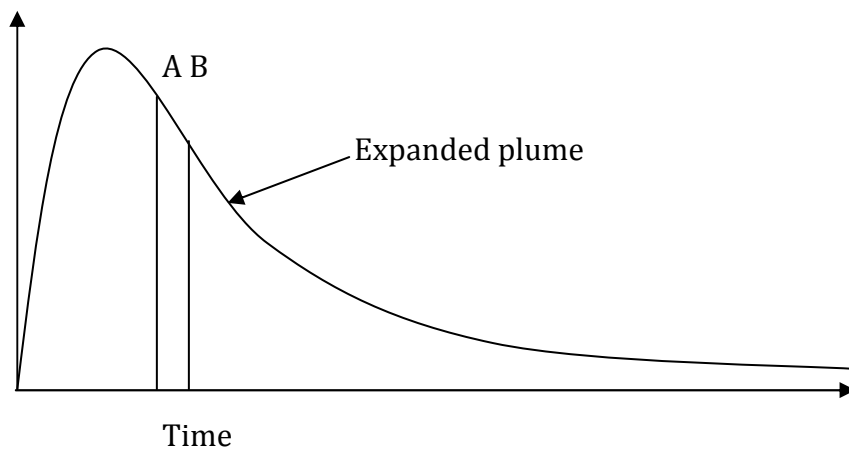


Figure 3.25 Scanning the plume by varying extraction times AB with respect to the Laser.

If two spectra are taken at varied times, e.g. 4 μs apart, but containing material of the same mass to charge ratio, then, the extraction region, imparting the same KE on all the material, will result in the two different spectra, having mass peaks detected and resolved at the same time. The intensity of these peaks

may vary due to more or less material being present at a particular time delay between the laser and extraction.

Secondly if the recording of the mass spectra was varied according to the triggering of the Pockels cell, then some data would be collected before the material is extracted into the ReTOF and the collected data, from detection of material flying the path of the ReTOF would vary according to the variation of the extraction. This would lead to the appearance of multiple peaks where in fact only a single peak is present.

3.5 Simulation Program (SIMION):

SIMION is an ion optics simulation program developed by Don McGilvery during an undergraduate research project for Professor James Morrison in 1973. It calculates electric fields for electrodes of defined voltages and ion trajectories in those fields [71].

The ReTOF system was drawn in SIMION, figure 3.26, shows a side view of the system, “ZY” direction. The outer chamber was taken into account and set to 0 V for accuracy. The system was copied as closely as possible to that of the actual ReTOF system.

Explaining the system from top to bottom of figure 3.26, the first plate shown is “A1”, the positive extraction grid. Next is “A2”, the negative extraction grid. The “top-hat” shaped electrode following this is internally connected to the liner, followed by an einzel lens named “Focus”, for first order focusing of the ion beam. The box lens discussed earlier is next, with three sides connected to the liner and one side, the “mass gate” individually controlled to guide the ions off axis. Following this below there is a short narrow flight tube which connects into the main flight tube, again internally connected and sitting at the same potential, this is named the “Liner”.

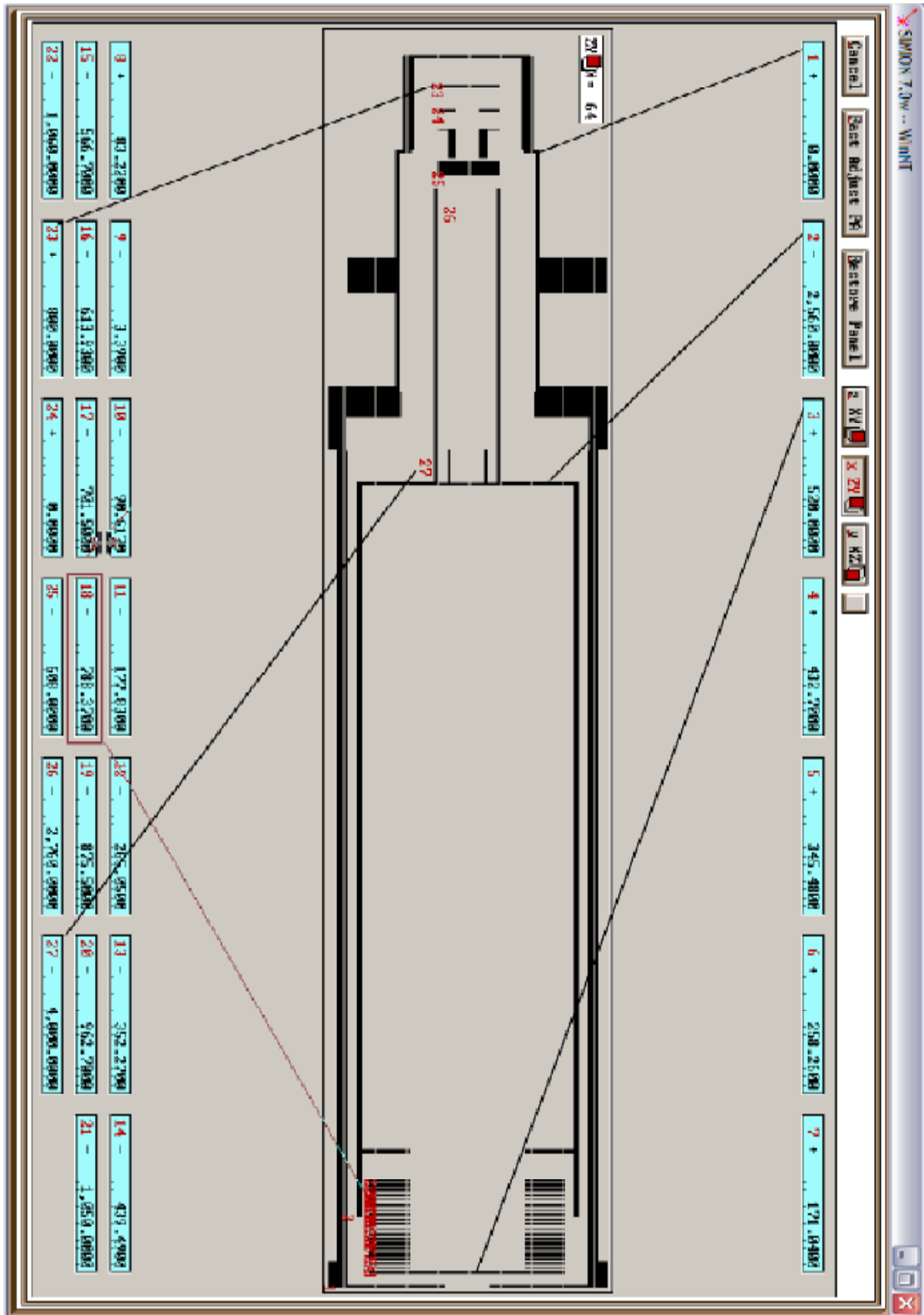


Figure 3.26. SIMION ReTOF design.

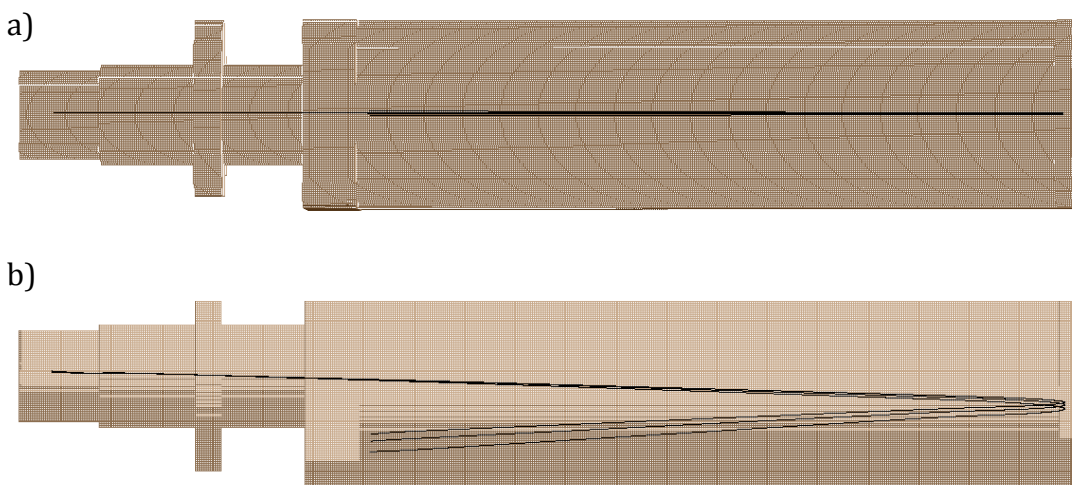
At the bottom of the diagram is the reflectron grid, starting with the first plate “VR1”, internally connected to further plates, stepping the voltage up to a

“VR2” positive plate. The ions are reflected back towards the MCP, which cannot be seen from this angle. The MCP is located at the entrance to the main liner section, from this view, at the same height as the entrance from the narrow flight tube, but closer to the viewer in the “X” direction.

After much trial and error with SIMION, the following voltages, table 3.1, were found to successfully guide Zn ions, mass 65.39, of charge 1, 2, and 3 through the system and impact on the MCP. The voltage applied to the MCP controls its gain, with the MCP turn on voltage of ~ 3500 V.

Electrode	Voltage
Chamber	0
A1	+400
A2	-400
Focus	-608
Mass Gate	-2360
Liner	-2560
VR1	-1050
VR2	+520
MCP	-4000

Table 3.1 Voltages for ReTOF system



c)

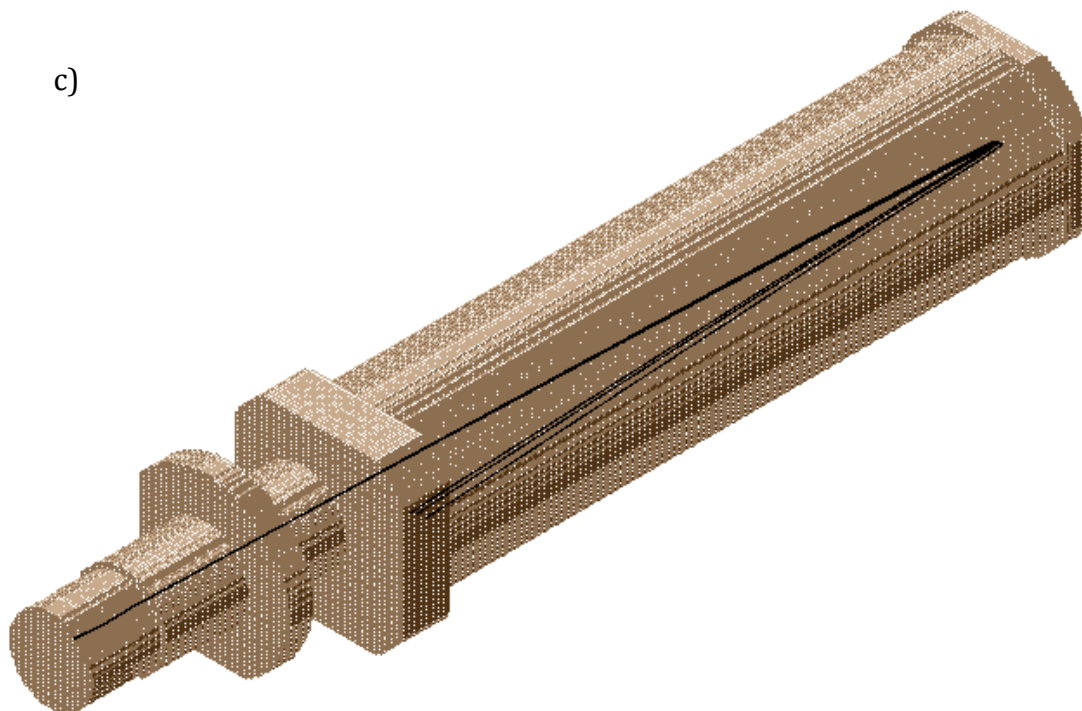


Figure 3.27, Ion flight through the ReTOF, a) side view, b) top down view, c) 3 dimensional view

Adjusting the potential difference of the extraction from 800 V to 400 V results in the ions crashing into the reflectron, figure 3.28

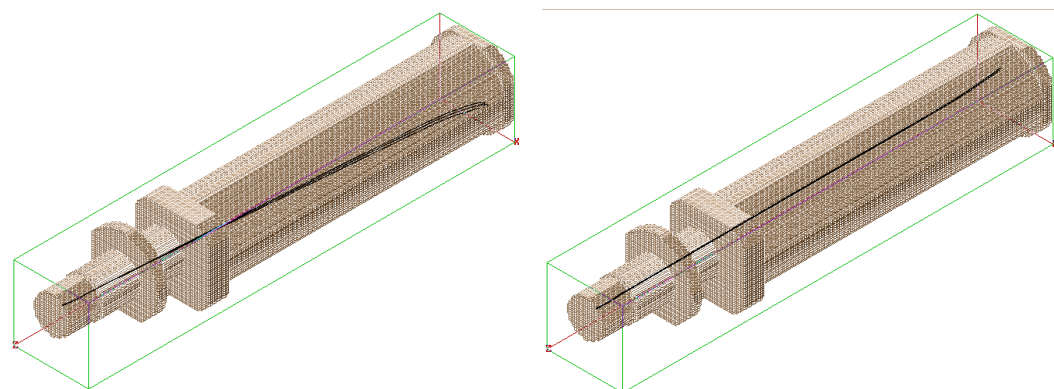


Figure 3.28, Ion flight through the ReTOF, a) extraction at +400, b) extraction at +1200.

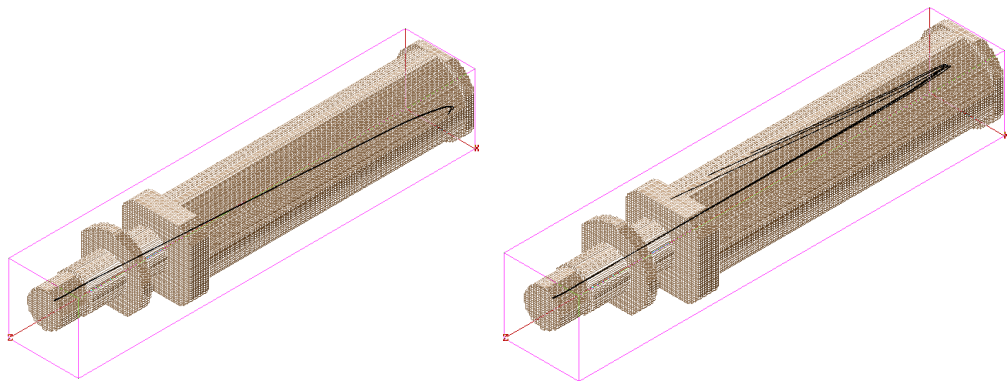


Figure 3.29, Ion flight through the ReTOF, a) Mass Gate -2560 V, b) Mass Gate – 2160 V.

Figure 3.29 shows the mass gate varied by ± 200 V, the effect is clearly enough to stop the detection of any particles. The Mass Gate and the extraction voltage are the two most important and critical voltages in the system.

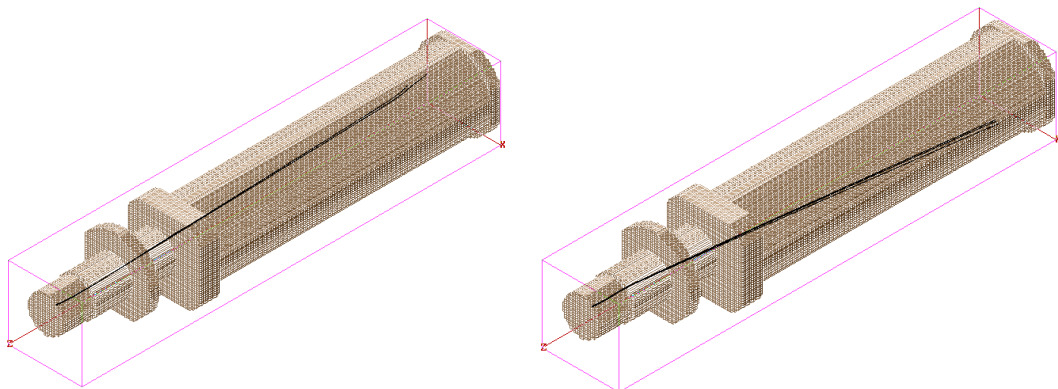


Figure 3.30 Ion flight through the ReTOF, a) Liner +500 V, b) Liner -500 V.

Finally figure 3.30 shows the effect of varying voltage on the liner by 500 V.

3.6 Computer Interface:

The final part of the setup was to interface the various parts of the system which did not come with interface software, but however, could be interfaced. These parts were: the oscilloscope, the pressure gauges, and the Stanford DG535 delay generator.

Both the delay generator and oscilloscope had GPIB interfaces, while the pressure gauge was interfaced using a RS232 to USB cable. The computer was equipped with a National Instruments IEEE 488.2 card for interface to the “Labview” software package.

The priority for this work was an interface to the oscilloscope as data collecting through a floppy disk was slow, meaning pumps would suffer under heavy gas loads for extended periods of time and general equipment ageing, such as flashing laser lamps without firing the laser regularly occurring. The interfacing of the delay generator and pressure gauges was more for practical purposes, as using them in the lab in “a hands on” approach was much more efficient.

The front panels and block diagrams for the pressure gauges and the delay generators can be found in appendix A. Below in figure 3.31, is the first Labview front panel to control the oscilloscope.

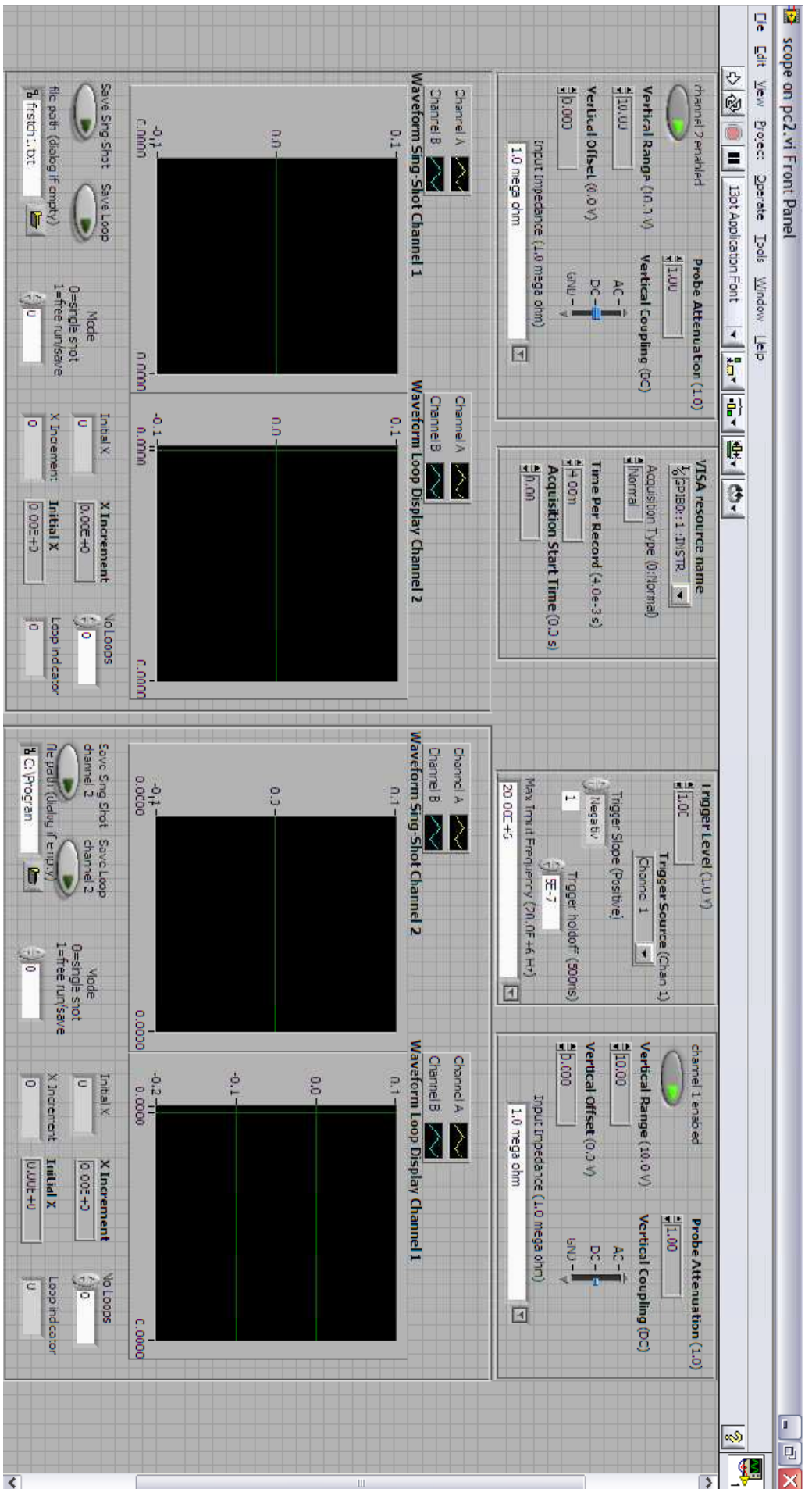


Figure 3.31, Labview front panel control of Tektronics TDS3032 oscilloscope

This allowed a complete control of the oscilloscope from the computer, however this was not entirely necessary as the two were beside each other, for this reason, I developed a smaller program which would simply fetch the data displayed on the oscilloscope.

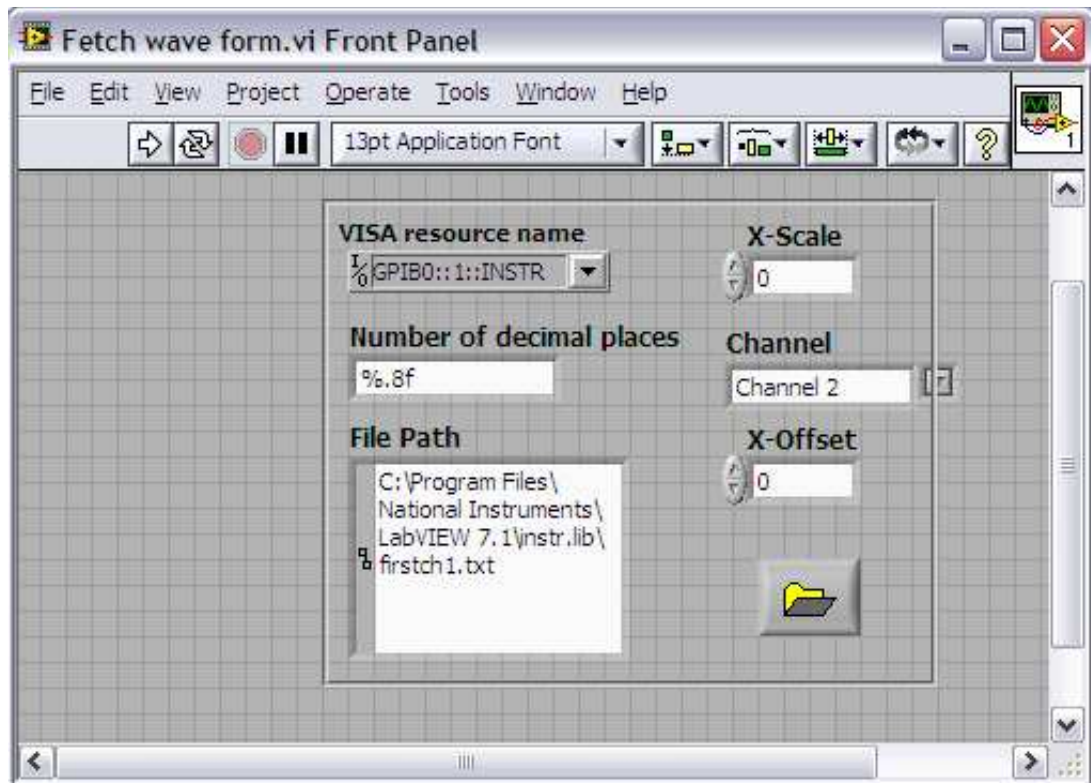


Figure 3.32, Labview front panel of “Fetch Waveform” file for Tektronics TDS3032 oscilloscope

Figure 3.32 shows the front panel of the “fetch waveform” file. This was designed to be simple and quick to use while collecting large amounts of data. Essentially the oscilloscope is used as normal, but to save the file. For this a path needs to be defined, usually once the path is defined the file name is increased by 1 etcetera for simplicity. The folder icon was used to define this file path although the path could also be typed, depending on the users preference.

Once the visa resource name is defined this would not need to be changed. The x-scale is defined to match that on the oscilloscope, if this is changed on the oscilloscope the definition on the fetch program must also be changed. The channel number must also be set, both channels could not be

recorded at once, for the experiment presented here this was not usually necessary and if it was needed, it simply required changing the defined channel on the program, i.e. the file name, ensuring the x-scale is correct and then running the program twice. Finally the x-offset was only used, if the trigger was not the zero point on the output of the display. In normal operation this was used to give a block of 20 μs , displayed before the zero starting point on the oscilloscope.

3.7 System Calibration:

As mentioned in section 2.6, the time of flight for the ion squared is proportional to the mass of the ion divided by its charge. The first step now, in the commissioning of the system was to collect data for various targets, recording the intensities of the peaks versus time, as it appears on the oscilloscope. For this four targets were used, Aluminium (Al), Zinc (Zn), Zinc Oxide (ZnO) and Tin (Sn). Squaring the time axis, results in data representing the relation $T^2 \propto (m/q)$.

The system was flushed out with O_2 and pumped down to 10^{-5} mbar. The laser was used at 1064 nm and set to 140 mJ focused to a spot size of 2 mm diameter. This gave a laser fluence of 4.5 J/cm^2 .

Figure 3.33 shows the intensity of peaks detected by the MCP versus time squared. The width of the mass peaks can be explained as follows; the Al ion has one mass peak at 26.981 atomic mass units (amu) with multiple charged states present but no other isotopes. Tin on the other hand has its main mass peak at 119.902, with an isotropic distribution of ten slightly differing masses, 111.904 - 123.905 amu.

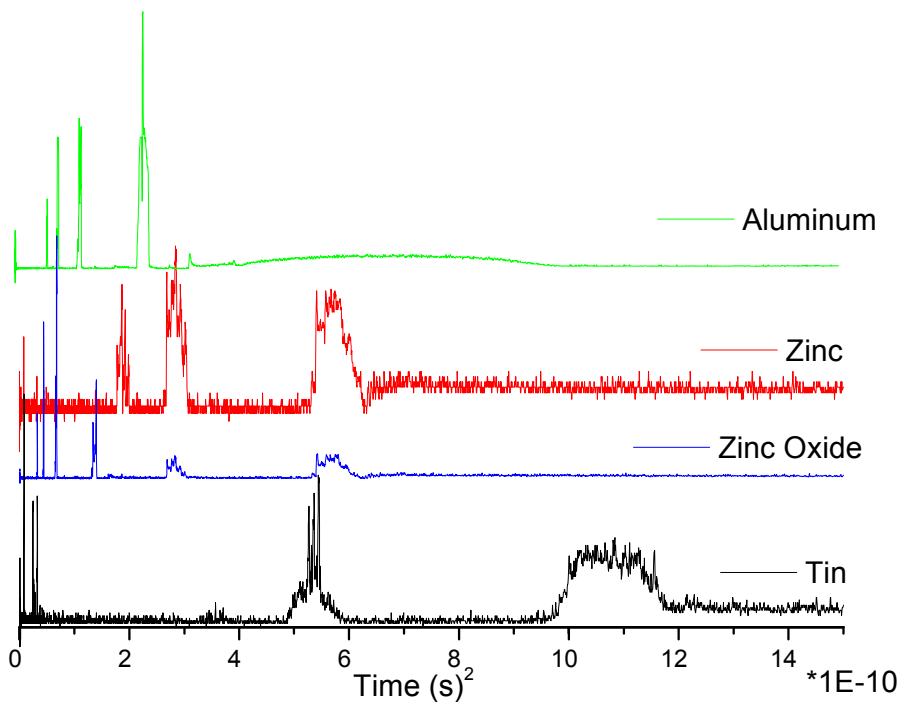


Figure 3.33, Time of Flight "Mass Spectra" calibration.

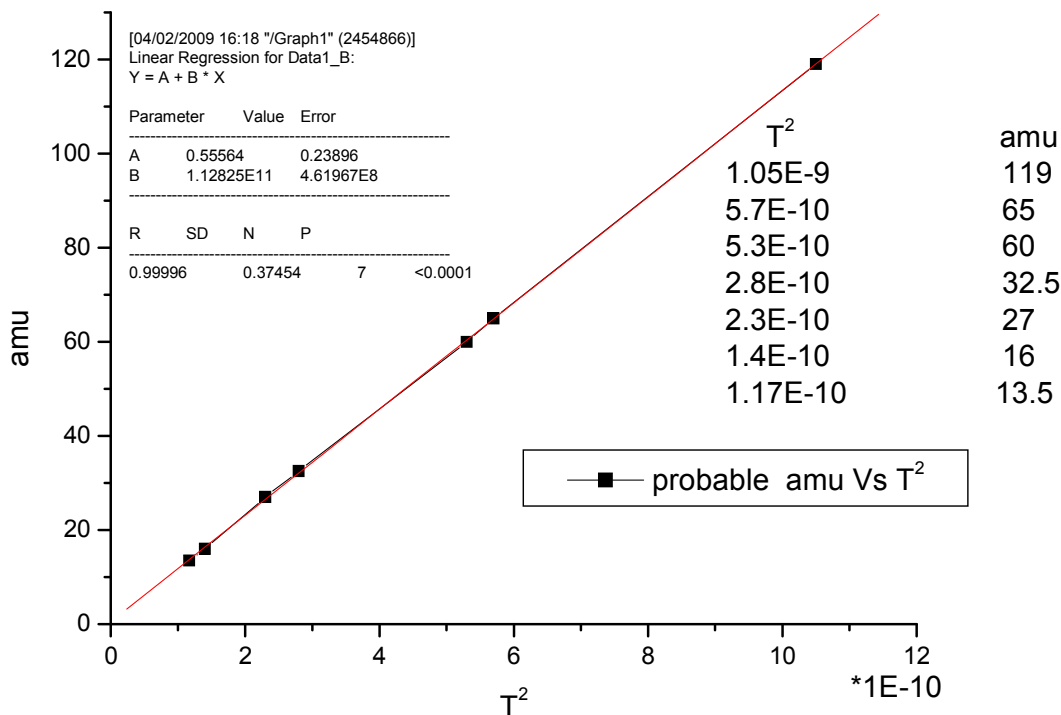


Figure 3.34, Linear fit of peaks in Time of Flight "Mass Spectra" calibration.

Figure 3.34 shows the probable mass, (m/q), of the detected ions versus time squared. This resulted in a linear plot therefore obeying equation 2.46. taking a best fit line resulted in the data presented in table 3.2.

Linear Regression for Figure 2.21, $Y = A + B * X$.

Parameter		Value	Error
A		0.55564	0.23896
B		1.12825E11	4.61967E8
R	SD	N	P
0.99996	0.37454	7	<0.0001

Table 3.2. Linear fit of Figure 3.33.

A: Intercept value and its standard error.

B: Slope value and its standard error.

R: Correlation coefficient.

p: value - Probability (that R is zero).

N: Number of data points.

SD: Standard deviation of the fit.

From this converting a time axis into a mass axis now simply involved squaring the time, multiplying this by the slope value, and adding the intercept value.

$$amu = ((column (time)^2) * 1.12825E11) + 0.55564$$

(3.1)

Figure 3.35 shows the same spectra as before but this time with the mass scale implemented. Clearly visible are Sn^+ , Sn^{++} and possibly Sn^{+++} with the appearance of some unknown light contaminants. The ZnO spectra shows single and double charged Zn and O peaks up to a fourth charged state, no ZnO present, this will be discussed in more detail later. Zn shows material up to a charge of plus 3, while Al shows charged states up to plus 4.

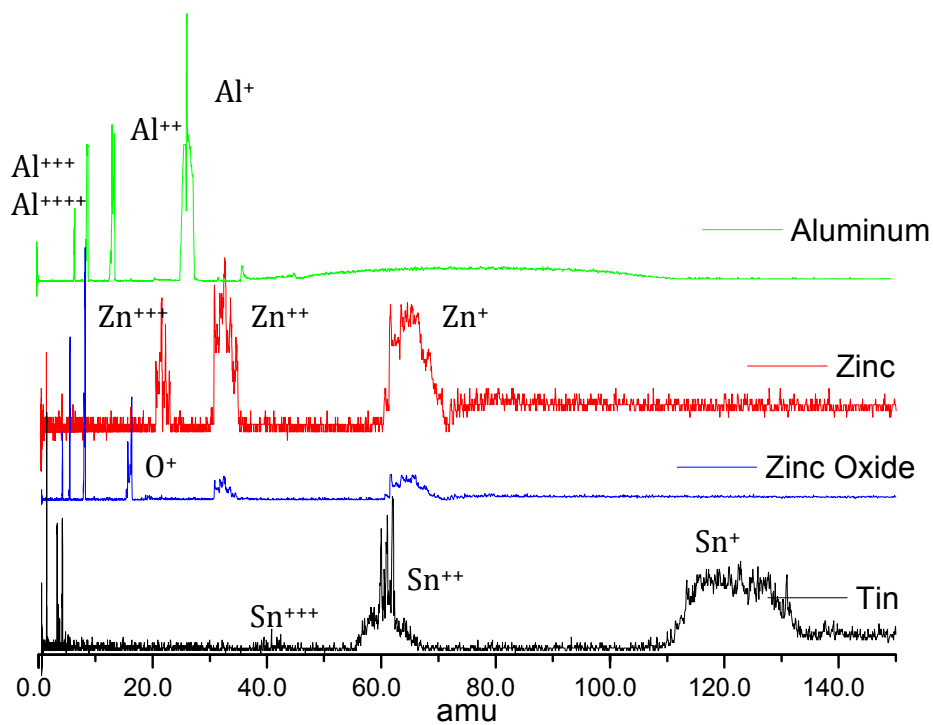


Figure 3.35, Mass resolved Time of Flight Spectra.

The varying of the extraction time during the experiment, as explained in section 3.4, in order to make up a single mass spectrum from the summation of numerous mass spectra, leads to inherent problems with resolution due to errors associated with, for example, variations in the plume such as jitter in the laser, the effects of varying temperature in the room by as little as 1 °C resulting in variations in the flight time or inconsistencies in the oscilloscope triggering of the order of 1 ns summed over 100 individual mass spectra, all resulting in broadening of the final measured mass spectra.

For comparison with the final mass spectra obtained in figure 3.35, figure 3.36 shows the mass spectra obtained for the laser ablation of the Zn target with an extraction time of 20 μ s after the laser pulse impacts on the target. Clearly shown are the isotopes of Zn⁺⁺⁺ at 21 amu, which corresponds to the singly charged 64 amu of Zn, with a relative abundance of 0.48. the second most abundant isotope of 66 amu with a triple charged state of 22 amu and a relative abundance of 0.27 is also seen, as

is the isotope representing 68 amu with a relative abundance of 0.19 and a triple charged state corresponding to 22.6 amu.

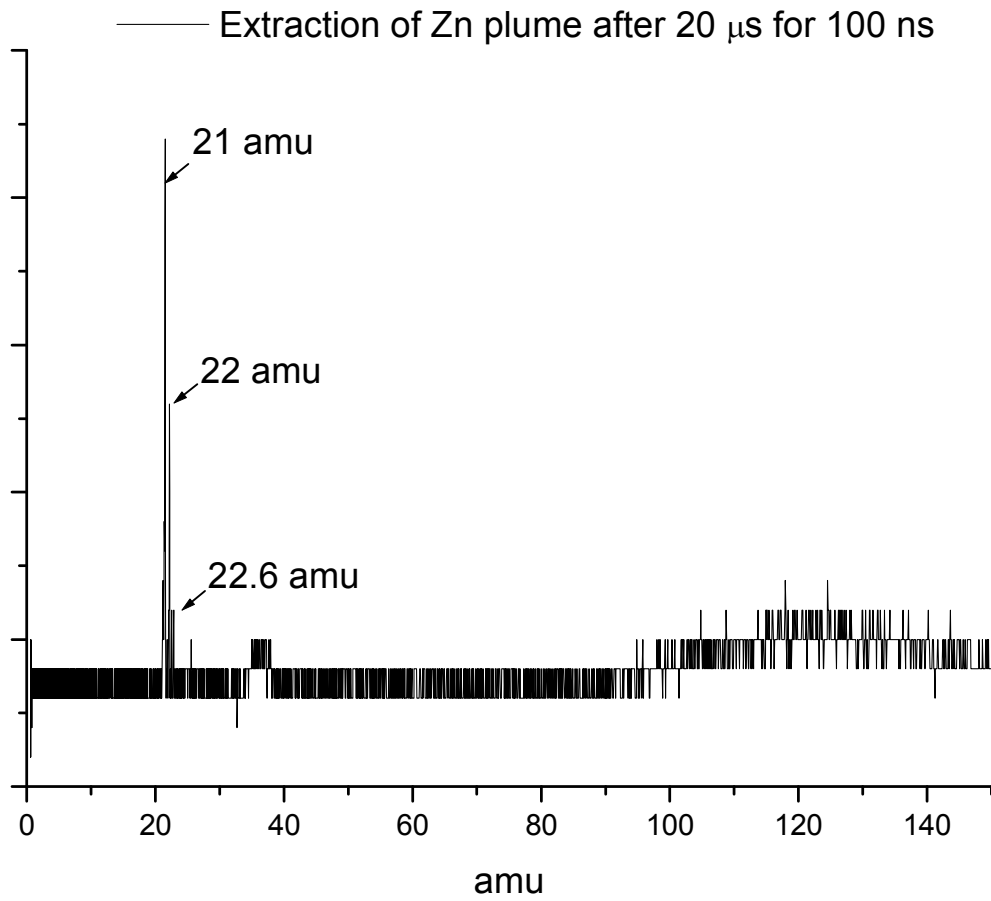


Figure 3.36, Single Mass resolved Time of Flight Spectra for Zn, extraction at 20 μ s.

Chapter 4:

FIELD EMISSION: RESULTS AND ANALYSES

4.0 Field Emission Background and Interpretation:

There is currently an interest in the development of new field emission electron sources for use in future technologies such as miniature x-ray sources [72] or novel flat panel displays [73]. This has been driven by the relative failure of carbon nanotubes to reach the initially hoped for role as the ultimate cold cathode in spite of intensive research in the past decade[74,75].

Materials that readily form wire-like structures and have attractive electronic and material properties such as a low work function and high thermal stability are the obvious alternatives as they should form efficient and stable electron sources. One such material is the n-type semiconductor ZnO.

ZnO Nanorods with good alignment, perpendicular to the substrate have been shown to be promising field emission electron sources with numerous reports detailing the use of ZnO nanostructures for such applications[76-77-78-79].

Reproducibility of the growth and an inter rod spacing has proved to be a problem for such applications, however in terms of scientific research, field emission test facilities can be used to verify, quickly, whether or not a sample is uniform.

Various signs can be seen with the use of field emission for detecting the quality of a nano-structured sample. Firstly a clean IV curve which is readily reproducible suggests that the sample has a homogenous height of grown structures.

A high field enhancement factor, figure 2.5, suggests that the samples are well spaced, a calculation of the field enhancement factor is also necessary to show that the emission mechanism is that of field emission.

A low turn on field, section 2.7, suggests the following:

1. the samples are conductive, if this is not the case perhaps the crystal structure of the grown material is poor.
2. that the structures have grown with a high aspect ratio
3. a low packing density is also likely. If these structures were densely packed, then the structures would screen each other and any advantage gained from a high aspect ratio would be lost due to the detrimental effects of this screening.

Finally, the imaging of the field emission sites, using a phosphor for conversion of the electron beam to light, allows confirmation of uniformity of the sample and can explain noise, or un-reproducible nature of the IV curve due to enhanced emission .

4.1 Field Emission Results From Hybrid Growth Technique:

The first samples tested were grown using silicon (100) substrates. The deposition technique was a hybrid PLD and Vapour Transport (VT) technique. The depositions were that of ZnO buffer layers via PLD and subsequent nanostructure growth via VT. Briefly, the substrates were degreased prior to growth by washing in isopropyl alcohol, followed by acetone and again with isopropyl alcohol. The substrates were then inserted into the PLD system and preheated at 950°C for five minutes. The deposition was performed by ablating a ZnO target of 5 N purity, in an oxygen atmosphere of 5 N purity. The substrate was kept at 300°C during deposition and the as grown ZnO buffer layers were then annealed in-situ at 700°C for 5 minutes. The deposition pressure was 1×10^{-1} mbar. A Nd:YAG laser, operating in the fourth harmonic, 266nm, was used at a fluence of 1.4 J/cm² for the ablation process. The pulse width was measured as 6 ns, and the operating frequency was 10 Hz.

The samples provided had buffer layers of approximately, 65 nm of thickness. The buffer layer has the effect of giving the substrate a better lattice match for the growth of the nanostructures than that of a clean silicon

substrate, this allowed the nanostructures to grow on the substrate in a uniform direction, as the buffer layer is of the same material as the nanostructures we expected to get a uniform linear growth perpendicular to the substrate.

The vapour transport growths were performed as follows, firstly all tools to be used, namely the boat used for growths, the mortar and pestle were all cleaned using acetone, and scrubbed with a wire brush before finally being dried using a high pressure nitrogen gas gun.

The system used for the vapour transport technique, fig 4.1b, consists of a furnace with a quartz tube running through its centre. Before commencing growths, the tube is left open and the inert gas, Argon, (Ar) is switched on via a mass flow controller at a rate of 90 sccm. This, although not being a large flow rate had the effect of cleaning the system of most of the residual gas from the tube being opened.

The growth of vapour transport samples was done using a mixture of ZnO and carbon (C) powder. The preparation of this material was as follows: A balance was used to accurately measure the material which consisted of 0.6 g of ZnO to 0.6 g C, (total 0.12 g). This mixture was poured into the mortar and ground together until the black carbon powder and white ZnO powder made a grey mixture. This powder was then loaded into a ceramic boat and spread out over approximately 2 cm, the technique used to spread the powder was to make a wave pattern and not have the powder flat across the 2 cm.

The carbon powder had the effect of reducing the deposition temperature by a process known as carbo-thermal reduction (CTR) [80]. The reactions that govern CTR VPT growth for the ZnO nanostructures under consideration here are as follows:



At the normal range of growth temperatures ($>700\text{ }^{\circ}\text{C}$), the gases produced by reaction (a) are Zn and CO. The overall reaction at high temperatures is given by reaction (a), and it is known that this is preceded by two intermediate reactions shown in (b) and (c), so the actual reaction pathway is via solid-gas reactions, and thus may be sensitive to the solid surface area.

The ZnO buffer-layered Si substrates were placed directly above the powder with the buffer layer facing towards the powder and then introduced into the centre of the horizontal tube furnace, figure 4.1. Growths were carried out at $\sim 850^{\circ}\text{C}$ in a 90 sccm Ar gas flow.

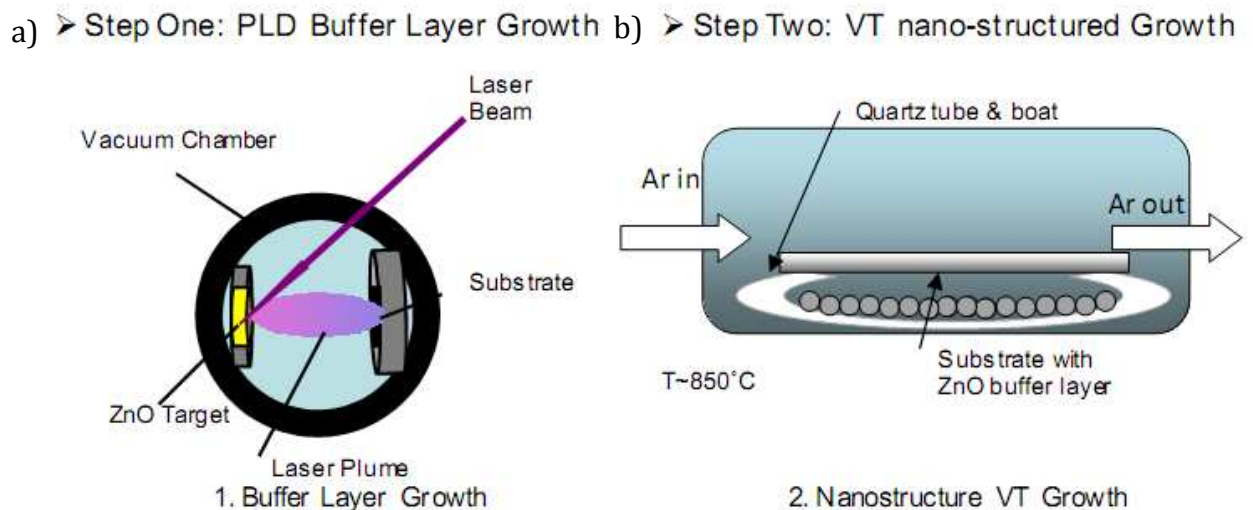


Figure 4.1. Two Step Growth of ZnO Nanorods, a) the PLD grown buffer layer of ZnO and b) the VT growth of ZnO nanorods.

The fastest possible ramp rate obtained with this system was calculated at $\sim 77^{\circ}\text{C}$ per minute taking 11 minutes to reach 850°C and left at this temperature for 20-25 minutes for nanorod growth. The furnace was then switched off, and left with the argon flow switched on for 6 hours to cool down.

4.2 Hybrid Growth Morphologies:

The 65 nm buffer layers were deposited in this fashion resulting in nanorods growth predominantly well aligned, 4-5 μm long and roughly perpendicular to the substrate, as shown in fig 4.2.

The majority of nanorods shown in figure 4.2 show two distinct regions, a uniform diameter for the long rod growth from close to the base to the tip, but the actual base is distinctly different showing a large tapered base to the substrate. For a comparison to this, samples were also grown by manually varying the temperature ramp rate during VT deposition.

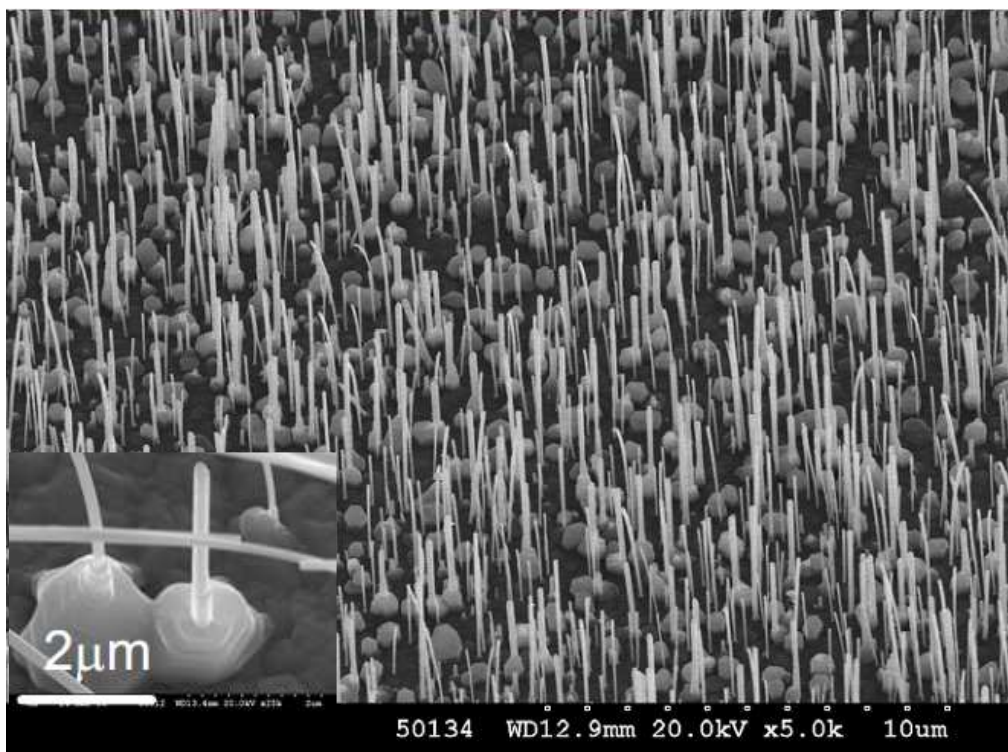


Figure 4.2 sample growth via 77° C / minute ramp of vapour transport temperature conditions on 65 nm buffer layers.

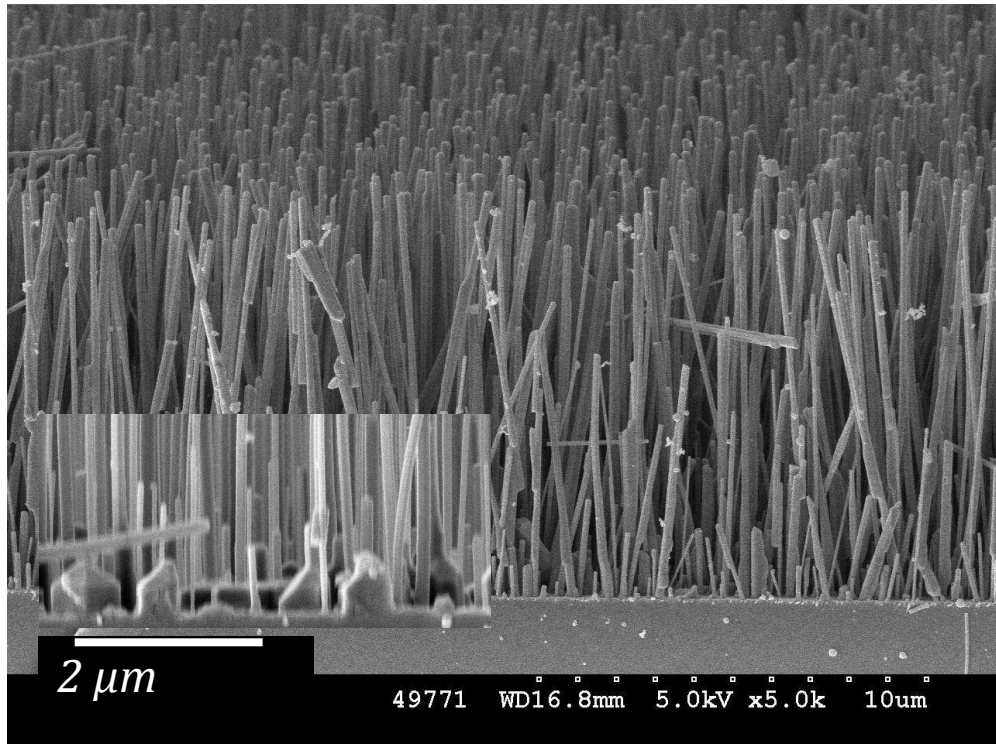


Figure 4.3 sample growth via 25° C / minute ramp of vapour transport temperature conditions on 65 nm buffer layers.

Figure 4.3 shows an SEM of a typical growth at 850° C by ramping up the temperature of the furnace at rate of 25° C per minute. The most outstanding difference in both SEM images is the density of the nanorods. Figure 4.3 also shows a uniform diameter along the growth of the nanorods with some dislocations near the base, shown inset, but no large base as is present in the faster ramp rate growth. The nanorods are 4 – 5 μm in length and have a diameter of < 200 nm.

Both the 75° per minute and 25° per minute ramp rates have similar length and, towards their ends, similar diameters. This suggests that the growth processes during the later parts of the depositions are similar, with differences in the early times of depositions resulting in differing growths at the base of the nanorods. This difference in early stage growth is attributed to the differing Zn supersaturation during the initial growth stages, which alters the growth mode from that of a 2D, layer by layer, growth under high Zn supersaturation, to 1D anisotropic nanorod growth [17].

4.3 Field Emission Results from ZnO nanorods grown by Hybrid Growth Method:

From a field emission aspect, the variation in inter-rod spacing, reported in 4.2, is interesting in order to see its effect on the field enhancement factor as described in section 2.8, with electric fields “bending” more around well spaced nanorods, and therefore interacting more with the rods’ edges. From field emission it is also possible to quickly learn if the sample is uniform by firstly checking the reproducibility of the IV curve, and secondly checking the emission pattern. Essentially if there are rods present with lengths noticeably longer than the average rod length, then these rods begin to emit before the uniform sample emission. If this rod length is such that all the electric field is focused around it, it will not be able to take the electric field strength and will essentially ionise in a process known as field ionisation [21].

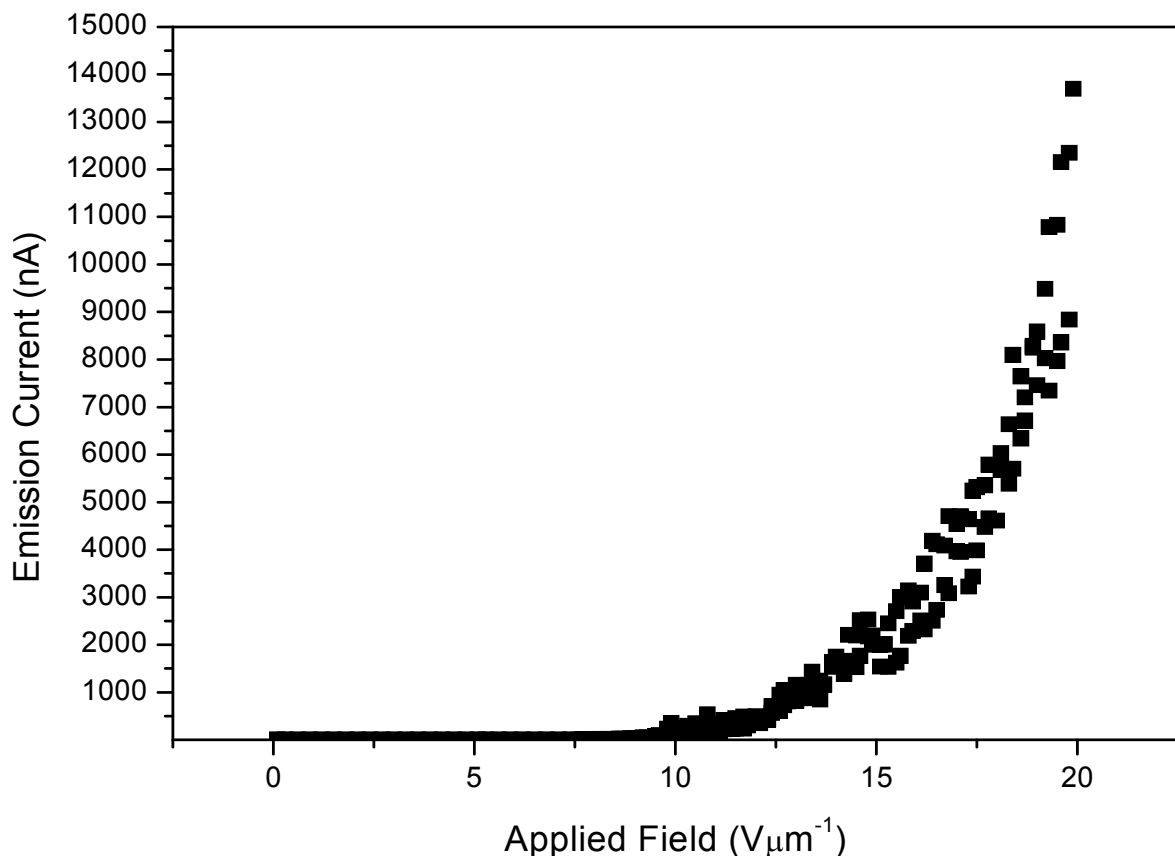


Figure 4.4 IV curve for sample of fig. 4.2

Figure 4.4 shows the field emission IV curve from the fast temperature ramp of ZnO growth on a 65 nm buffer layer. This ramp rate resulted in a field

emission curve, which was reproducible both increasing and decreasing the e-field strength, and for repeated runs with little conditioning required to produce the above IV curve (~ 2 runs). The initial turn-on field is found to be $\sim 7 \text{ V}/\mu\text{m}$, with the extrapolated turn on field $\sim 15 \text{ V}/\mu\text{m}$.

Figure 4.5 shows a plot of $\ln\left(\frac{I}{F^2}\right)$ versus $\frac{1}{F}$ for the data presented in figure 4.4, where electron emission occurs. This results in a straight line indicating that field electron emission is the dominant emission process as mentioned in section 2.7. Using equation 2.28, and taking the work function of ZnO to be 5.3eV, results in a field enhancement factor of 1299 ± 29 . This is very different from the expected field enhancement factor from $\beta \sim \text{length}/\text{radius}$, in our case $\sim 60\text{--}80$ [17].

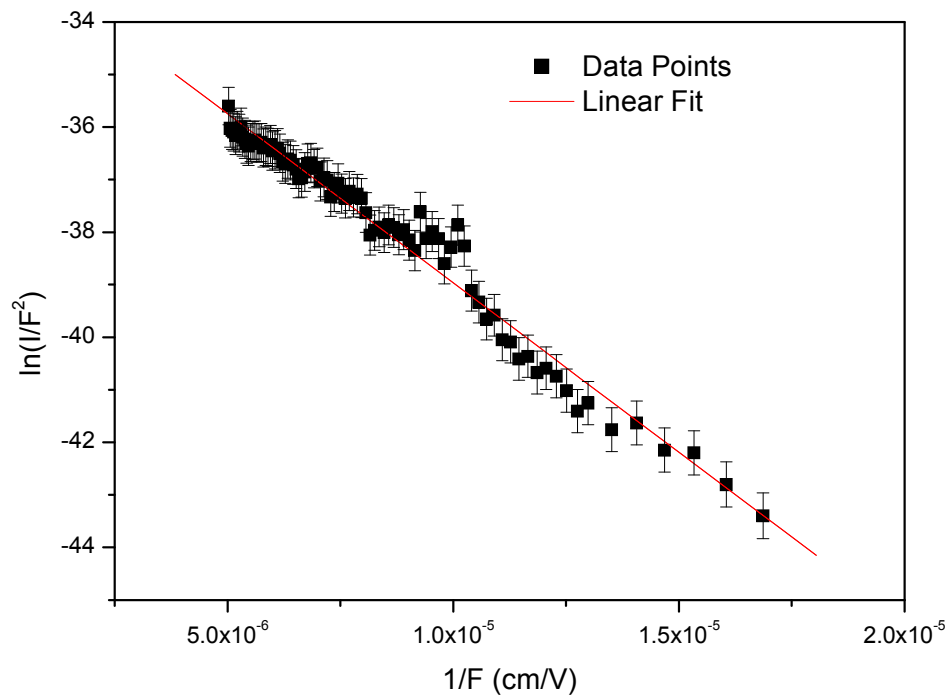


Figure 4.5 plot of $\ln\left(\frac{I}{F^2}\right)$ against $\frac{1}{F}$, F = electric field, for low density high ramp rate deposition.

Figure 4.6 represents the IV curve of the higher density sample, shown in fig 4.3, grown with a lower temperature ramp rate of $25^\circ/\text{minute}$. The IV curve of the higher density sample appeared noisy suggesting electron emission from

randomly longer nanorods than the average nanorods length of rod grown on the sample. Even after ten voltage ramps the noise on these samples remained.

The initial turn-on field for the slow temperature ramp rate is again ~ 7 V/ μm , with the extrapolated value ~ 11 V/ μm . Due to the higher density of nanorod coverage in the growths at a slow temperature ramp rate, one could expect the field enhancement factor be lower than that for the lower density of coverage, fast temperature ramp rate growths, but if we plot as before the $\ln\left(\frac{I}{F^2}\right)$ versus $\frac{1}{F}$, as can be seen in figure 4.7, we find the enhancement is slightly higher at 1667 ± 84 .

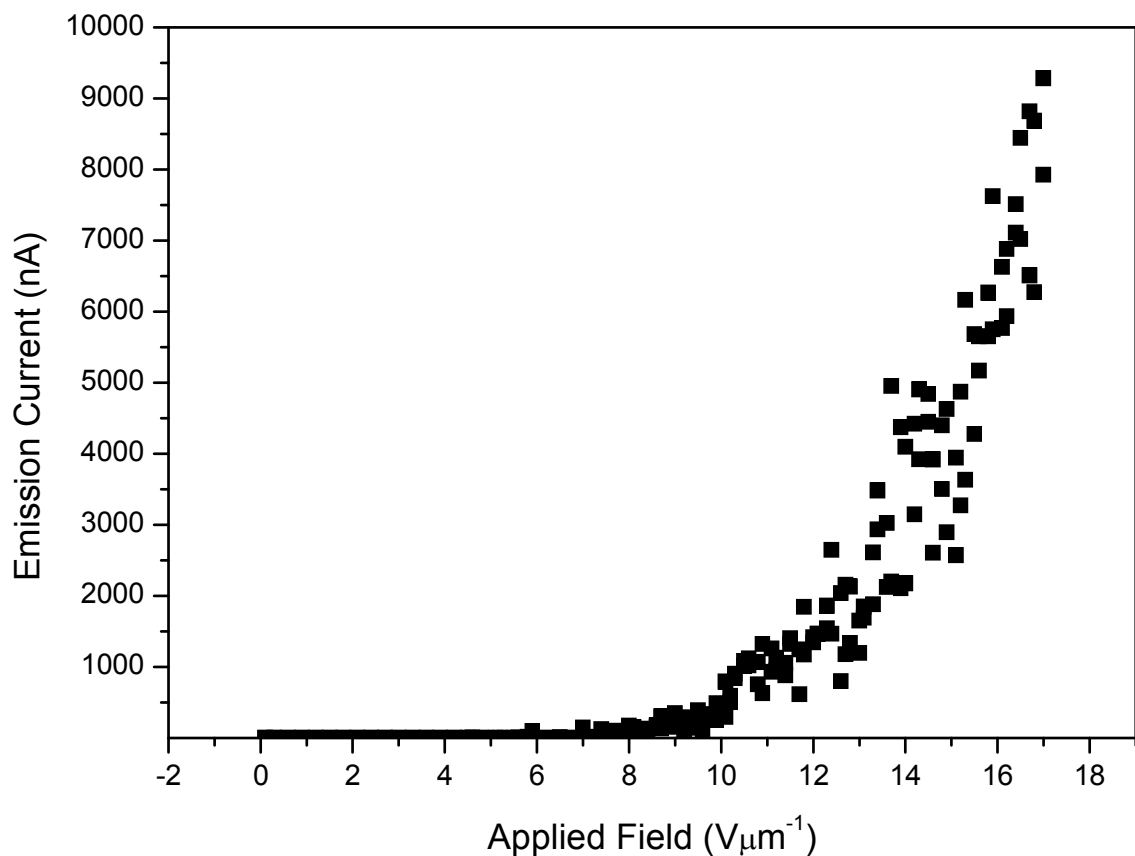


Figure 4.6 IV curve from high ramp rate (25° / minute) of vapour transport temperature conditions on 65 nm buffer layers.

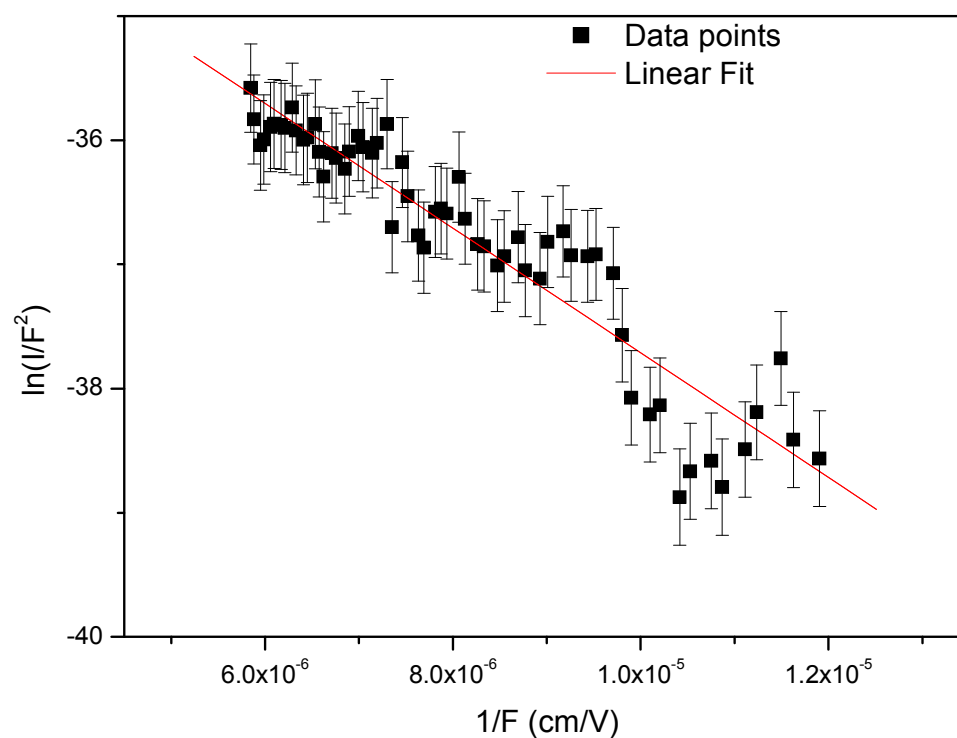


Figure 4.7 plot of $\ln\left(\frac{I}{r^2}\right)$ against $\frac{1}{F}$ for high density low ramp rate deposition.

Using a transparent electrode covered in $\text{Y}_2\text{O}_2\text{S:Eu}$ red phosphor powder, Appendix C, the converted, electron to light, emission patterns across a 6 mm diameter of both samples were taken and are shown in figure 4.8.

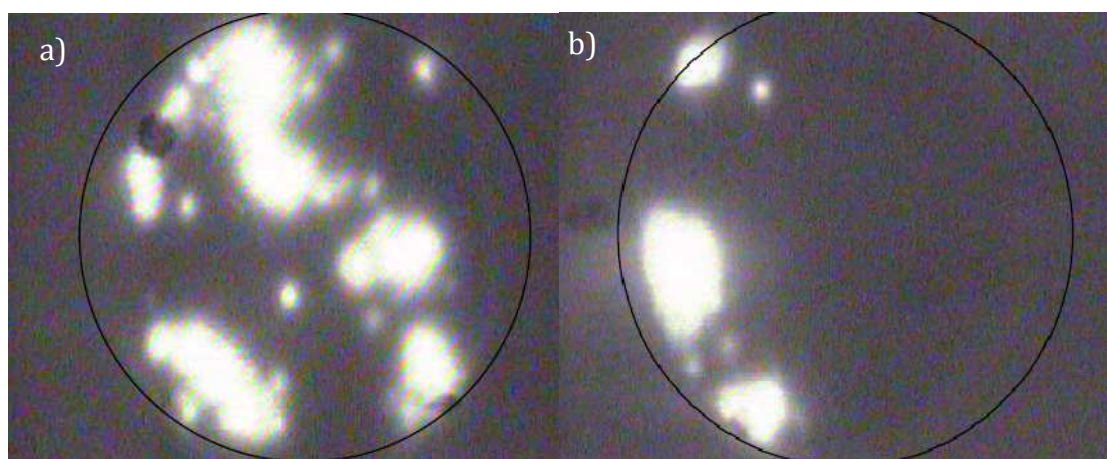


Figure 4.8 Emission pattern of Field emitting sites, circle diameter 5 cm. (a) corresponds to the high ramp rate low density sample, fig 4.2, (b) corresponds to the low ramp rate dense sample, fig 4.3.

The low density image shown in figure 4.8 (a) is taken at 4500V while the image of the high density sample, (b), is taken at 4000V. In both cases the uniformity of emission is not good, but generally the lower density samples give some emission throughout the sample, with emission from only a few localised sites close to the edge of the dense samples.

4.4 Interpretation of the Data:

Overall the data indicates that the sample with a lower density of nanorods results in an increased uniformity of emission sites. The turn on fields and the field enhancement factors are similar while it appears that the sample with the high density of nanorod growth results in a screening of the electric field, leading to a reduction of emission site density[81, 82]. This screening is most likely due to the close proximity of neighbouring nanorods. The similarity in field enhancement factors between the two growth techniques is explained by the occasional growth of taller nanorods protruding above the height of the average rod height, these rods would emit before the surrounding rods and essentially “burn off” as the electric field is increased, which would also explain the noise and need for a number of voltage ramps to obtain reproducible results.

The pattern of emission in figure 4.8 (b) shows significant non-uniformity along the left-hand edge of the image. Emission from a small area like this would explain the noise of the IV curve and the need for repeated ramps of the IV curve in order to arrive at a relatively reproducible one.

4.5 Field Emission Results From PLD Growth Technique:

Pulsed laser deposition (PLD) has recently been recognised as a suitable technique for the production of field emission device-quality ZnO nanowires/nanorods with the corresponding growth mechanisms debated by many authors [12-83-84]. Our system aims to analyse the growths during the deposition by allowing for simultaneous mass analysis with the help of the in-

situ reflectron time-of-flight (ReTOF) mass spectrometer, figure 3.18. The conditions in which optimised field emitters are produced and their possible relationship to both the processes of plume cluster formation and nZnO growth have been studied. Growths were performed using two laser wavelengths, 1064 nm, and 355 nm, with the intent that subsequent mass spectrometry measurements could determine the presence of clusters in the differing plasma plumes.

4.6 Sample Growth:

Samples were grown via pulsed laser deposition, in the custom designed system presented in Chapter 3. Q-switched Nd:YAG lasers were used either at the fundamental wavelength of 1064 nm or the wavelength of 355nm after frequency-tripling. The pulse width was about 6 ns for both wavelengths and the pulse repetition rate was 10 Hz. The fluence on target was kept fixed at ~ 7.7 J/cm² and obtained with a focal spot diameter of ~ 1 mm at 45° incidence.

The target was a 5 N's purity ZnO ceramic disk, which was continuously rotated and translated during deposition so as to present a fresh surface for each laser shot. The depositions were carried out either in a high vacuum at a pressure of 10⁻⁵ mbar or in an oxygen ambient pressure of 10⁻² mbar using a mass flow controller at a rate of 22 sccm. The depositions were performed at room temperature on clean phosphorus-doped n-type Si (111) substrates placed parallel to the expansion of the plume, 5-7 cm away from the target. Each deposition employed 9,000 laser shots.

4.7 PLD Growth Morphologies:

The samples growth orientation parallel to the plume expansion is a well known technique commonly referred to as glancing angle deposition [85]. Samples morphologies corresponding to growths at 1064 nm are presented in figure 4.9. Part (a) in 10⁻² mbar of oxygen while part (b) grown in 10⁻⁶ mbar (base pressure).

In the conditions of figure 4.9 (a) long narrow microstructures are obtained, randomly distributed over the surface, with typical length of $\sim 10\ \mu\text{m}$, no other structures are seen at greater magnifications. In Figure 4.9 (b) both long ($10\text{-}15\ \mu\text{m}$), narrow ($0.2\text{-}0.5\ \mu\text{m}$) microstructures and nano-particles ($150\ \text{nm}$) are observed. Both structures appear to be randomly distributed across the surface. The magnification in this case has been optimised to show more clearly the two types of structure.

For all structures the growths are facing away from the plume, by varying the orientation of the substrate with respect to the incoming vapour flux a variation of columnar growth has been seen by other authors [86]. A systematic change of the angle 'a' between the incident atom flux and the substrate normal has been correlated with the angle 'b' between the growth of a column's axis and the substrate normal.

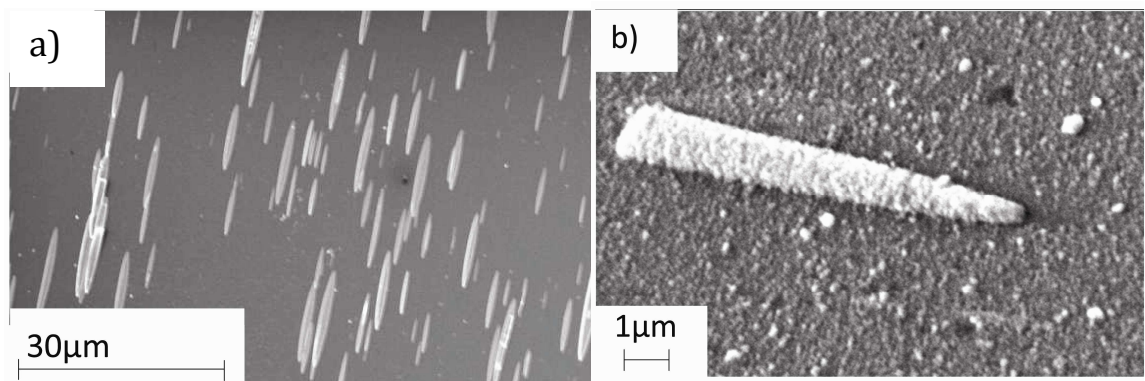


Figure 4.9 SEM images of nanostructured thin films grown on Si (111) substrates with: (a) pressure = 10^{-2} mbar, overhead image. (b) base pressure tilted image.

Samples morphologies corresponding to growths at 355 nm, 9000 laser, shots are presented in figure 4.10. Part (a) represents 10^{-2} mbar of oxygen while part (b) represents 10^{-6} mbar, base pressure.

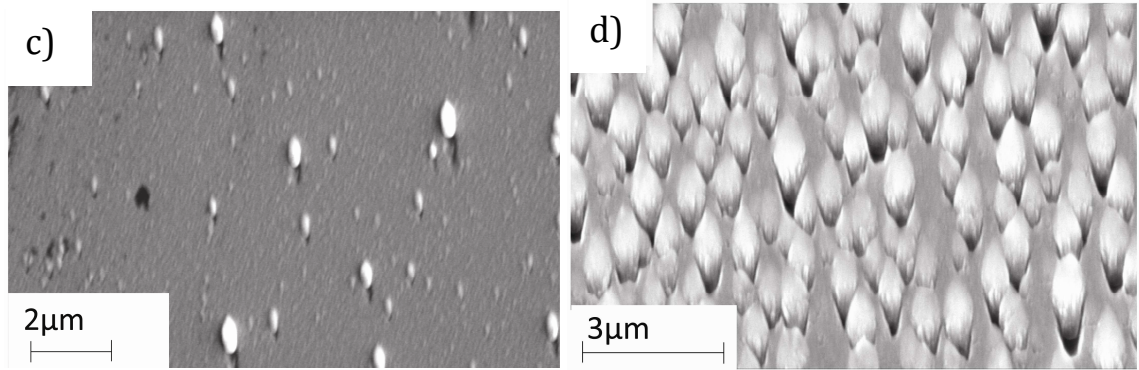


Figure 4.10: SEM images of nanostructured thin films grown on Si (111) substrates with: (c) 10^{-2} mbar, flow of O_2 at 22 sccm tilted image. d) 10^{-6} mbar overhead image.

In the conditions of figure 4.10 (c), one observes oblong nanostructures with average widths of 170 nm, average lengths of 350 nm while the average inter-structure spacing is typically 1 μm . In figure 4.10 (d) we observe some self-organized growth of microstructures with dense packing on the surface and consistent heights and widths of $\sim 1 \mu\text{m}$ and 0.5 μm , respectively.

Energy dispersive X-ray spectroscopy (EDX) was also performed on all samples and indicating the presence of Zn and O peaks for all the samples. EDX works by penetrating the surface of the sample, and therefore is more sensitive to bulk properties of the substrate, it is only used here as an indication of the presence of Zn and O in the sample.

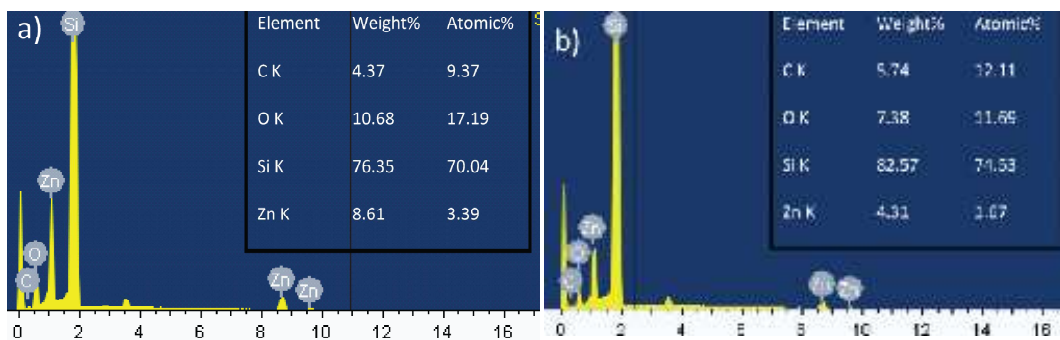


Figure 4.11: EDX spectra of growths at 1064 nm, a) corresponds to the O_2 regime and b) corresponds to the vacuum regime

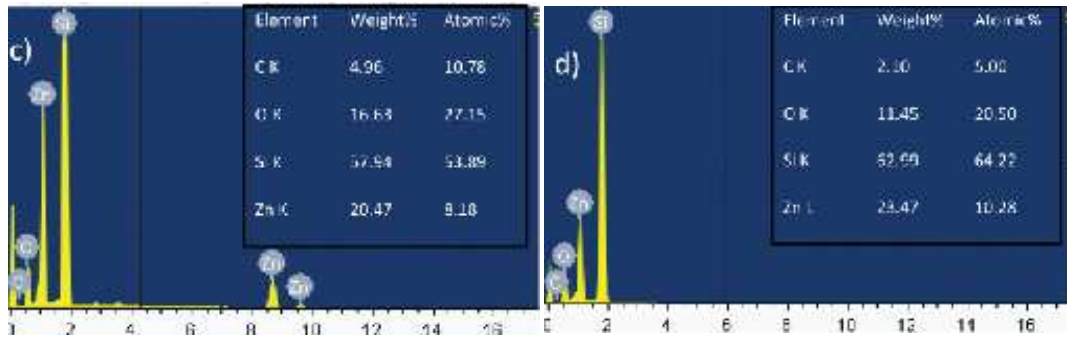


Figure 4.12: EDX spectra of growths at 355 nm, c) corresponds to the O₂ regime and d) corresponds to the vacuum regime

4.18 Field Emission Results from PLD Growth and Analysis

The field emission I-V curves of the aforementioned growths are shown in figure 4.13. The turn-on field, determined by extrapolation of the I-V curve, were $\sim 11.8 \text{ V}\mu\text{m}^{-1}$, $7.5 \text{ V}\mu\text{m}^{-1}$, $6.0 \text{ V}\mu\text{m}^{-1}$ and $5.2 \text{ V}\mu\text{m}^{-1}$ for samples (a), (b), (c) and (d) respectively.

Fitting the data using Fowler-Nordheim plots showed linear behaviour, fig 4.14, indicating the FN theory may be applied to obtain field enhancement factors.

Field enhancement factors for samples (a), (b), (c) and (d) were calculated by again, taking the work function of ZnO is 5.3 eV and, using the slope of the linear graph resulting in $\beta = 1238$ for sample (a), the 1064 nm 10^{-2} mbar deposition, $\beta = 1622$ for sample (b), the 1064 nm 10^{-6} mbar deposition, $\beta = 1891$ for the 355 nm 10^{-2} mbar deposition and $\beta = 2060$ for the 355 nm 10^{-2} mbar deposition.

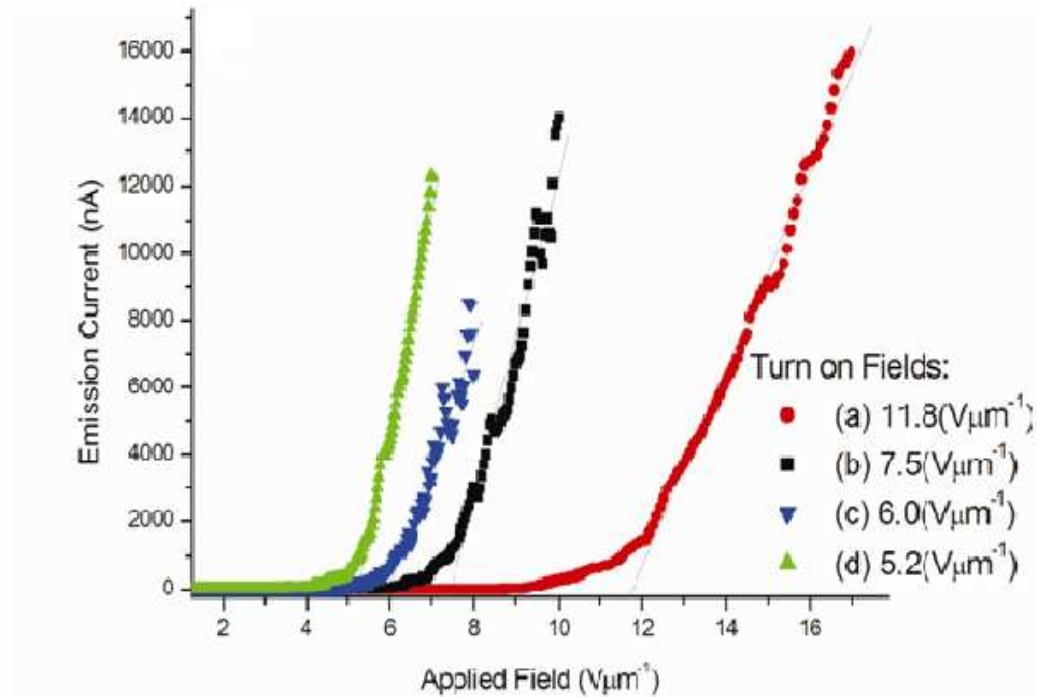


Figure 4.13 IV curves from PLD grown ZnO surfaces on Si (111) substrates (a) 1064 nm 10^{-2} mbar, (b) 1064 nm pressure of 10^{-6} mbar, (c) 355 nm pressure of 10^{-6} mbar (d) 355 nm pressure of 10^{-2} mbar.

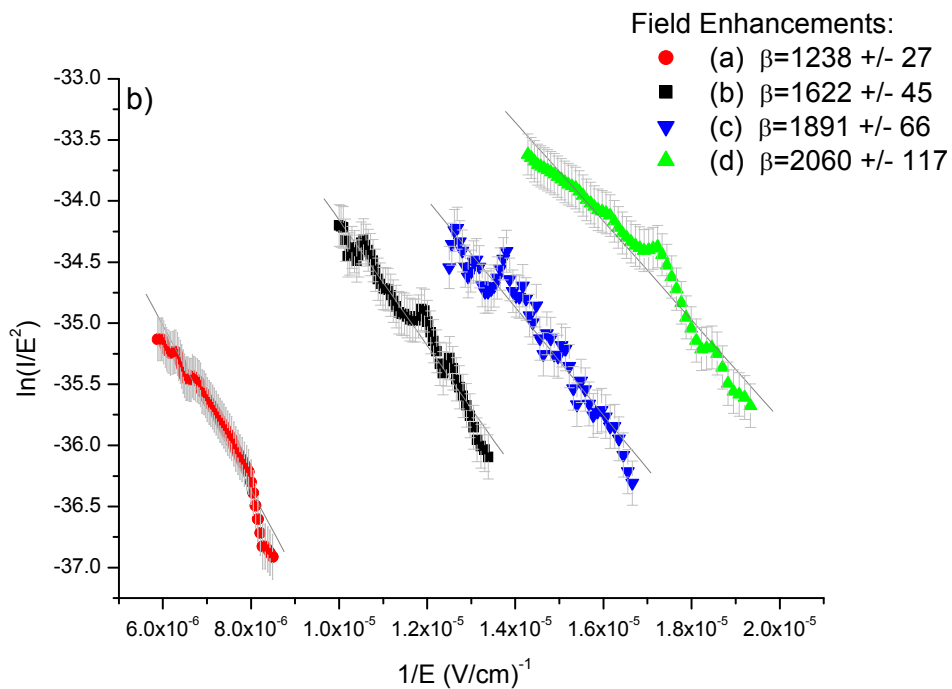


Figure 4.14 fits to Fowler-Nordheim equation for all samples $\ln\left(\frac{I}{F^2}\right)$ versus $\frac{1}{F}$.

The above analysis shows that the most uniform nanostructure, that of sample (d), gives the most efficient turn on field with the highest field enhancement factor. This can be attributed in part to the favourable nanostructure morphology showing nanotips and also to the high surface coverage density of the sample.

The FE properties of sample (c) can be explained by a downward trend from these favourable conditions due to a lower coverage density of oblong nanostructures yielding the second highest field enhancement factor of 1891 and lowest turn on field of $6.0 \text{ V}\mu\text{m}^{-1}$, respectively.

Again this downward trend continues for sample (b) with a higher turn on field increasing to $7.5 \text{ V}\mu\text{m}^{-1}$ and a lower enhancement factor of 1622 compared to samples (c) and (d). This can be clearly related to the samples morphology comprised of particle-like nanostructures and long flat microstructures which both have low aspect ratios leading to a low enhancement factor.

Finally, both the lowest enhancement factor and highest turn-on field values of 1238 and $11.8 \text{ V}\mu\text{m}^{-1}$ were observed for sample (a) for which no nanostructured tips were present but only long microstructures lying flat on the surface.

From figure 4.14, we also observe that the samples grown at 10^{-6} mbar have higher enhancement factors than the samples grown at 10^{-2} mbar in identical experimental conditions for a given laser wavelength. This can be explained in terms of the varying electronic properties of the deposits caused by the varying concentration of oxygen vacancies which is likely to result from the growth at different oxygen pressures. It should be noted that in the case of ZnO nanorods Zhao et al. [87] have shown that the field emission properties are strongly influenced by the surface oxygen vacancy concentration. These effects can lead to the presence of surface states which can significantly affect the field emission properties via modification of the work function due to band bending effects [88-89]. However, in our experimental conditions where no oxygen anneals were applied, oxygen vacancies are likely to affect both the bulk and

surface electronic properties. A comparison of the values obtained here for the field enhancement factors and turn on fields with those of other works [90,91, 92] where the emphasis is on producing well-aligned, high-aspect ratio nanostructured ZnO, such as in our hybrid growth techniques described above, suggests that the field enhancement factor may be as much dependent on the ZnO material electronic properties as it is on the morphology.

Chapter 5:

ANALYSIS OF LASER PRODUCED ZnO PLASMAS

5.0 Background and motivations

Laser produced plasmas have seen their range of applications increase dramatically since their first inception in the early 1960's. Examples include Pulsed Laser Deposition (PLD) [8], Laser Induced Plasma Spectroscopy, LIPS [93], or High Harmonic Generation (HHG) of short wavelength light [94] to name just a few.

An interesting point with regards to the work presented here is that in many cases of the above mentioned processes, it is common to use an ambient gas environment for controlling highly energetic particles and to diminish debris [95 - 96].

An interesting feature of laser ablation processes has been the observation of emission of fast electrons in a background gas [97]. Hough et al. [98] have used time-resolved Nomarski-Interferometry to show that electron densities, in a zinc, (Zn), plasma plume, at early times, in an O₂ background gas differ to the vacuum situation with more electrons detected further from the target in the O₂ case.

Many studies have already been performed on laser produced plasmas in ambient gases such as early studies by Koopman et al.[99] which, depict results suggesting a collisionless electrostatic shock front propagating radially at the leading edge of the plasma front in an ambient plasma.

Cronberg et al.[100] investigated laser produced plasmas of graphite. They observed the disassociation of ionic carbon clusters by energetic electrons created in the plasma. They ruled out the possibility of ionisation and disassociation occurring due to multiphoton excitations and ionisations as a result of the incoming laser beam. They observed an energy distribution of electrons depending on laser pulse energy and these electrons possessing

energies in excess of 15 eV. These initially photo-emitted electrons are accelerated to high energies via inverse bremsstrahlung, with the energy they acquire sufficient to produce an electron impact ionisation and dissociation of the carbon in the gas phase.

Isaac et al.[101] observed the emission of a fast electron peak after the ablation of a silver target with a 1064 nm Nd:YAG laser. They compared the temporal width of this peak with that of the laser pulse width, remarking that the two FWHM's were almost the same. This, they say, shows that the electrons are not the thermal electrons of a laser produced plasma and must be photoelectrons accelerated through the inverse-bremsstrahlung process. The electron density is found to increase with distance from the target, indicating a cascade ionisation of the ambient gas.

Wood et al. [102] modelled the expansion of a plasma in an ambient gas, (argon, Ar, and Helium, He) and assigned the fast peaks to the probability that some of the ionised material would reach the detector without any collisions with the ambient gas, a form of plume splitting, essentially agreeing with Koopman et al [99].

Amoruso et al.[103] directly measured the kinetic energy distribution of prompt, fast electrons produced in nanosecond excimer laser irradiation of Al targets, concluding that the prompt electron emission occurs as a consequence of two-photon photoelectric effects during the laser ablation pulse.

Saeki et al. [104] investigated the excitation mechanism of a neon (Ne) buffer gas during the laser ablation of silicon. Using time and space resolved emission spectroscopy, they assigned the fast process of excitation of Ne* to level selective excitation by electronic – electronic and translational – electronic from Si⁺.

Harilal et al.[105] examined the ambient gas effects on laser produced Sn plume expanding into Ar. Apart from thermalisation and deceleration of plume species the addition of Ar resulted in double peak formation in the temporal distributions and ambient plasma formation. Optical emission spectroscopy showed strong emission of Ar⁺ at early times even before the arrival of Sn

plasma at 5mm from the target surface. They argued that this fast peak was due to the ionisation of the ambient gas, with this resulting in a more efficient electron impact excitation and plasma recombination. This would enhance the emission of these species in the plasma.

A better understanding of the particle emission via laser ablation therefore still needs to be developed in order to exploit laser produced plasmas to their full potential, whether it would be as electron sources utilising high power density laser spots, or for PLD of materials with relatively low laser fluence.

For the laser ablation of ZnO for the deposition of materials, although device quality ZnO nanostructures have been grown by various groups, using quite similar conditions, there seems to be no agreement on the corresponding nanostructure growth mechanism by PLD [106].

For example Sun et al. [107] analysed the post growth structure of their nanorods to find a Zn capping layer which they use as evidence of the vapour liquid solid (VLS) growth mechanism, Lorenz et al. [108] had a similar conclusion employing gold coated sapphire substrates to produce a variety of nanostructures.

With regards to ZnO Sage et al. [109] have recently presented mass spectra of laser ablated ZnO at 532nm, in vacuum, resulting in multiply charged atomic Zn and O but with no ZnO detected.

Yan et al. [110], using the PLD technique, analysed the surface roughness as a function of deposition cycles, concluding that the main growth mechanism was the Stranski-Krastanov (SK) one.

One theory on the growth mechanism of particular interest to the present study assumes ZnO nanostructures grow from nucleation centres on the substrate formed by nanoparticles created in the expanding plume. To verify this, Kawakami et al. [111] used Rayleigh scattering imaging and concluded on the presence of ZnO nanoparticles in the ablation plume. This group concluded that the growth mechanism is nano-particle assisted pulsed

laser deposition (NAPLD) whereby the particles condense on the substrate surface acting as seeds for further nanomaterials growth[112-113].

The presence of clusters in a ZnO laser ablated plume has also been confirmed by Ozerov et al. [12] whereby photoluminescence spectra were performed on the expanding plume itself however no depositions were performed in the study.

The most direct experimental diagnostic would be to measure clusters using mass spectrometry. This technique has been used routinely to understand laser ablation, for example of superconducting materials [114].

In the case of mass spectrometry measurements of laser ablation of ZnO, Kukreja et. al. [15] measured mass spectra for nitrogen laser fluences of 0.125 J/cm² and 0.01 J/cm² and recorded a complete series of (ZnO)_n clusters up to (ZnO)₂₀. No enhancements of the cluster yield corresponding to n equals to a magic number was observed, (see section 1.23).

Behrman et al. [16] had previously shown using molecular-dynamics simulations of (ZnO)_n clusters that at certain magic numbers (n=12, n=16) the clusters spontaneously form into fullerene-like spheroids. These theoretical predictions have not been verified experimentally to date.

A. Dmytruk et. al. have recently depicted a technique utilising zinc peroxide (ZnO₂) as a precursor for the formation of ZnO clusters showing no indication of magic numbers [115]. In a later paper the same group have detailed magic numbers of ZnO [116], again via the laser ablation of a ZnO₂ target, which “could represent previously unpredicted clusters of enhanced stability at n = 34, 60 and 78”.

From the above summary, the following questions could be answered using our system.

Firstly, considering the distance our ion probe and extraction region of the mass spectrometer are from the ablating target, does the mass spectrometer detect the same particles at two different “peak” times in the presence of a background gas and therefore prove or disprove the theory of plume splitting

mentioned above. In relation to this, if we measure the mass spectrum, is there an ionisation of the background gas, and if so, where could this ionisation originate from.

And secondly, with a view to investigate experimental conditions leading to cluster formation, how does the mass spectrum change with varying laser wavelength, fluence and the ambient pressure in the chamber, and can any magic numbers of clusters be detected.

5.1 Ambient effects comparison between vacuum, O₂ and N₂ atmospheres.

In order to answer the first question, we put ourselves in the most favourable of conditions, by maximising the amount of ionised material. To do this the fundamental wavelength of the laser was used, thus getting the highest power output, and secondly to focus the spot to a relatively small size. These conditions were quite similar to those employed by Harilal et al. [105]

Briefly for the experiment, the laser pulse width, (FWHM) was measured to be 6ns operating at 10Hz. A 30cm focal length lens was used to focus the laser beam with an energy of 600mJ to a spot size of radius 0.5mm resulting in an on target fluence of 77J/cm². The radiation hits the target with an incident angle of 45°. A ZnO target provided by MaTECK GmbH was used, 99.999% purity. The target was moved to reveal a fresh surface for each laser shot. Experiments were carried out in three different atmospheric regimes. Firstly, in a vacuum environment with a pressure of 10⁻⁶ mbar, secondly, in an oxygen ambient of 10⁻² mbar and thirdly, in a Nitrogen ambient of 10⁻² mbar. The introduction of O₂ and N₂ was controlled by a mass flow controller at a rate of 30 sccm.

The mass spectra for the ReTOF were obtained by utilising a Stanford DG535 pulse generator to delay the extraction pulses on the plates at the entrance of the ReTOF. This enabled scanning of the plume as it arrived at the extraction plates. The delay of extraction was incremented by 2µs for a total

duration of 200 μ s. This resulted in numerous mass spectra as a function of extraction time, all averaged for 64 shots, which were then analysed to produce a single spectrum containing all information gathered. The ions were extracted by a potential difference of 800V for 100ns in order to obtain high resolution. By viewing the individual mass spectra used to arrive at the final spectra, it was possible to identify the arrival times in the extraction region of the ReTOF of various species of ionised material.

Figure 5.1 shows the final mass spectra of ZnO after ablation with 1064 nm radiation at an energy of 70 J/cm² with a) ablation in vacuum, b) ablation in 10⁻² mbar O₂ ambient and c) ablation in 10⁻² mbar N₂ ambient.

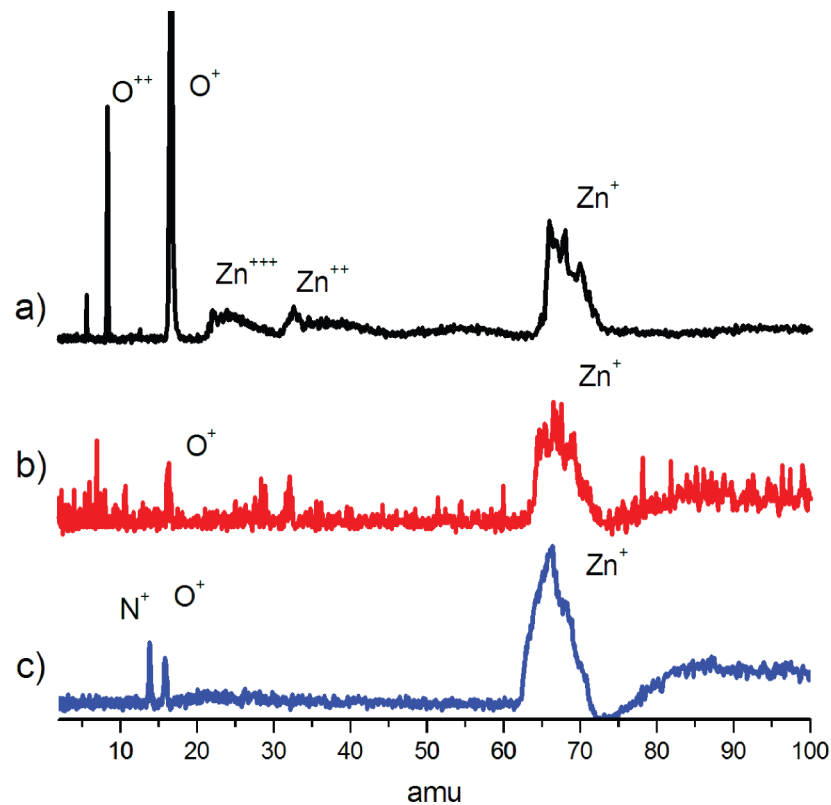


Fig. 5.1: Reflection Time of Flight mass spectra of ZnO target ablated via Nd:YAG laser operated at fundamental wavelength of 1064nm recorded at 70J/cm², with a) a background pressure of 10⁻⁶ mbar, b) a background pressure of 10⁻² mbar flow of O₂ at 30sccm and c) a background pressure of 10⁻² mbar flow of N₂ at 30sccm.

The additional noise in the ambient conditions is attributed to the higher gas pressure on the micro channel plate detector. It is clear to see that there was no clear ZnO present in any of the acquired spectra, a similar observation as Sage et al. [109] The broad Zn peak is present in all spectra, the lack of

resolution for the Zn^+ ion, in the isotropic distribution, is attributed to the averaging employed. This is specifically noticeable for Zn due to the isotropic distribution of the 5 relatively important Zn isotopes. This is in contrast to the sharp singly important isotopes of oxygen and nitrogen ions.

The second obvious result from the mass spectra is the additional charged states present in the vacuum conditions which are not present in either of the ambient conditions.

Finally the presence of both N^+ and O^+ for the spectrum acquired for 10^{-2} mbar of N_2 indicates an ionisation of the ambient gas and O^+ originating from the target surface. The detection of O^+ from a ZnO target in an O_2 ambient leads to some ambiguity as to the source of the ion. The ionisation potential for the first excited state of molecular oxygen is 13.6eV [117], given that the ionisation potential of the first excited state of molecular nitrogen is 14.5eV [118], then, the mass spectra show there are processes energetic enough to ionise atmospheric nitrogen. It is therefore not unreasonable to state that the atmospheric oxygen, with a lower ionisation potential than nitrogen, could also be ionised.

The presence of both the N^+ and O^+ in a nitrogen atmosphere proves these energetic processes are present, therefore we have ascertained the O^+ signal originates from the target but in the presence of an oxygen ambient this signal must also have a component which originates from the ambient gas.

5.2 Electron temperature analysis:

In order to further understand the processes involved in the ionisation of the gas it is necessary to analyse the temporal behaviour of not only the ions but also the electrons in the plasma.

Figure 5.2 is the signal acquired by varying a positively biased ion probe located at the entrance to the ReTOF's extraction region for both the O_2 and N_2 ambient experiments. There is clearly the presence of a fast component, a sharp peak followed by a short dip before the emergence of a large broad signal for

both O_2 and N_2 atmospheres. This large broad signal is seen to last for several microseconds.

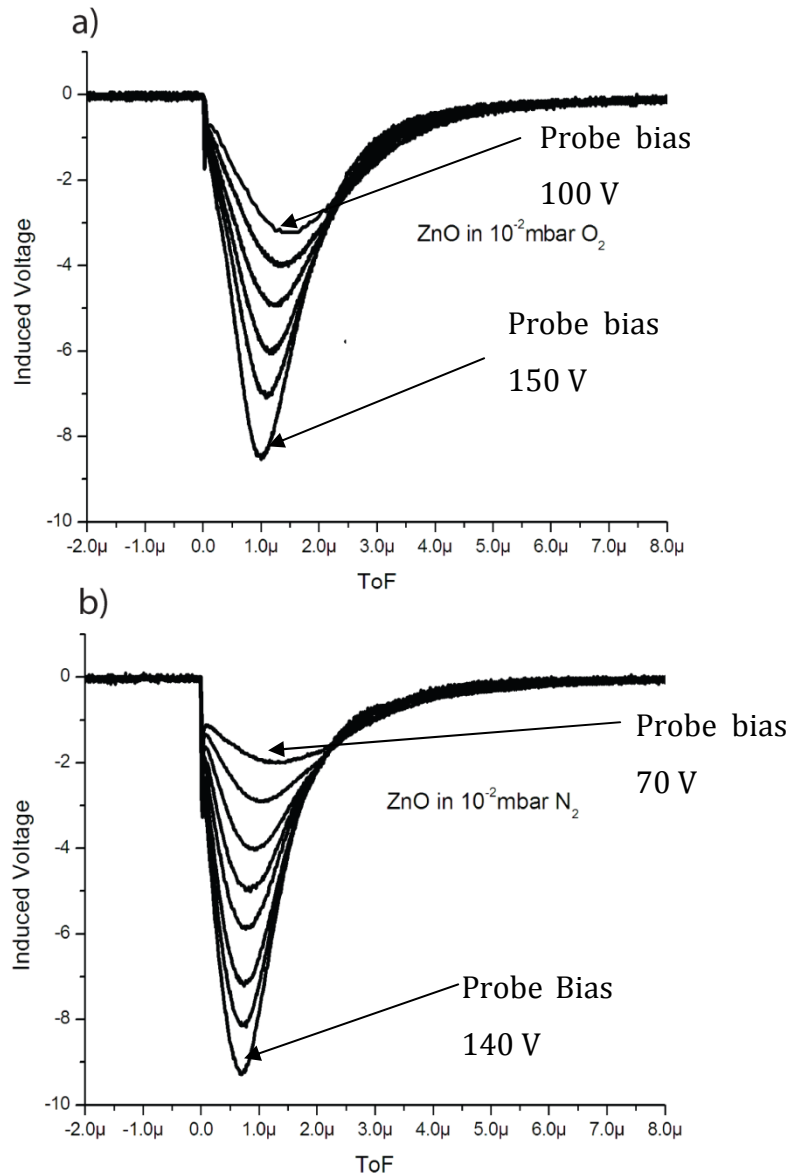


Fig. 5.2: Electron Probe Time of Flight of ZnO target ablated via Nd:YAG laser operated at fundamental wavelength of 1064nm recorded at 70J/cm² in a) a background pressure of 10⁻² mbar flow of O₂ at 30sccm and b) a background pressure of 10⁻² mbar flow of N₂ at 30sccm. Probe voltage was varied by 10 V for each new curve.

The fast electron signal, most pronounced in O_2 , but also visible in N_2 , has been discussed in detail by many authors, with a general consensus that it is due to photoelectric excitation [101, 119].

We rule out the possibility that the fast electron signal originating from photoelectric excitation result in the ionisation of the ambient gas. The maximum kinetic energy of electrons coming from a multiphoton - photoelectric process can easily be calculated by:

$$E_K = n_0 \frac{hc}{\lambda} - A \quad [5.1],$$

Where h is the Planck's constant, c is the speed of light, λ is the laser wavelength, A is the work function of the target and n_0 is the minimum number of photons necessary to balance the work function of the metal.

ZnO has a work function of 5.3eV, therefore for a laser operating at a wavelength of 1064nm, $n_0 = (5.3\text{eV} / \text{photon energy}) = 4.55$. This means that the target atoms must absorb a minimum of 5 photons and thus, the photon energy, given by $n_0 \frac{hc}{\lambda}$ is calculated to be 5.65eV and therefore the maximum E_K of the photo emitted electrons is 0.35eV. This implies that the ionisation of the ambient via an electron impact between the direct photo emitted electrons and the molecular gas is not possible as the maximum kinetic energy is too low. It must however be noted that an acceleration of these electrons is caused by inverse Bremsstrahlung heating the system.

5.13 Ion Temperature Analysis

Our setup allows us to turn our attention to the ions arriving in the ReTOF's extraction region and by analysing their temporal distributions it is possible to gain further understanding of the origins of the ionised material.

By reversing the bias on the ion probe we will attract these ions instead of electrons, this will result in a time of flight profile of the positively ionised material. Secondly, as mentioned earlier, we may look at the mass spectra as the extraction time is varied, this will allow us to associate a temporal distribution with each mass to charge ratio.

For this experiment we look at the vacuum ambient case to see if charge transfer is possible from the higher ionised states to the gas. Figure 5.3 depicts three separate traces. Firstly, on top is the ion probe measurement taken at 10^{-6} mbar. Secondly, the scatter trace for each ionised state shows data from the mass spectra, which have been individually analysed, and the presence of particular masses at certain extraction times noted. These extraction times were then plotted and the intensity of the mass peak summed over its mass range to essentially degenerate the mass spectrum into an ion TOF spectrum. This gives the added advantage of knowing what ions make up the TOF profile.

The density of charged particles is given by both the ion probe presented here in figure 5.3 and the mass spectrum presented in figure 5.1. Thirdly, fits are made of each (m/q) TOF distribution, created by the back substitution of data collected from the mass spectrometer to shifted Maxwellian functions, line plots fig. 5.3.

Kelly and Dreyfus [53] have shown that if the detector is located at a distance “x” perpendicular to the target surface, employing a flux sensitive detector and provided the Knudsen layer thickness is much smaller than the flight distance, the probability, P(t), of detecting an ion with a time of flight, t, is adequately solved using:

$$P(t) \propto x^2 t^{-5} \exp\left(-\left(\frac{m}{2kT_i}\right)\left(\frac{x}{t} - u\right)^2\right)$$

[5.2]

Where x is the distance from the target to the detector, m is the mass of the ion, k is the Boltzmann constant, T_i is the ion temperature determined by the total width of the flight time distribution and u is the average centre of mass velocity.

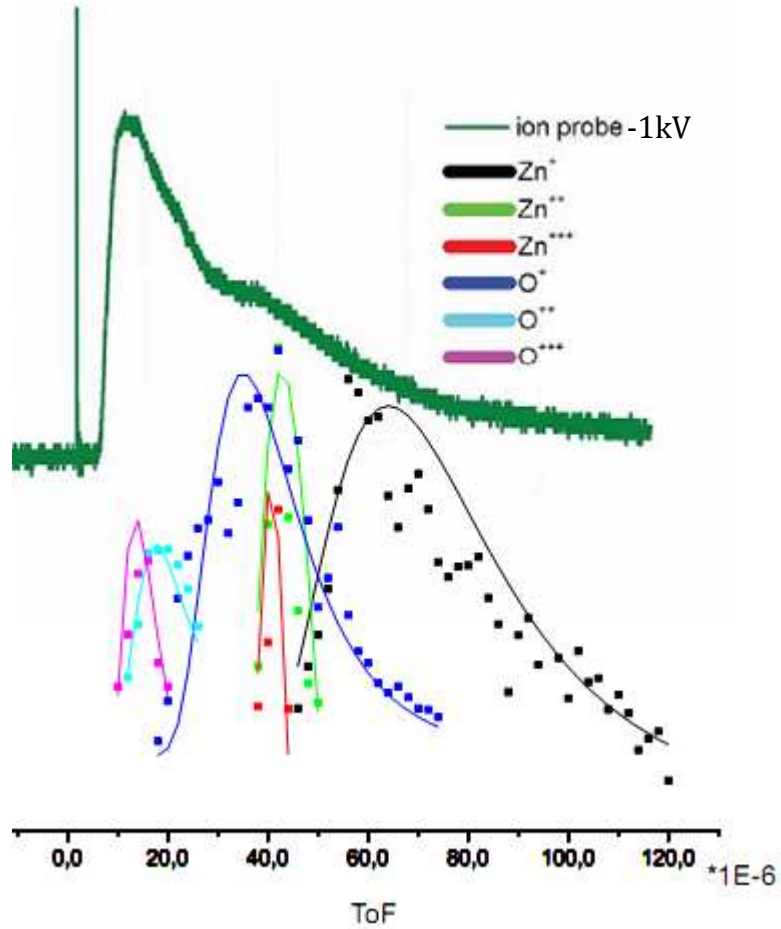


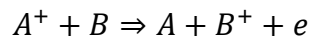
Fig. 5.3: Ion Probe Time of Flight of ZnO target ablated via Nd:YAG laser operated at fundamental wavelength of 1064nm recorded at 70J/cm² in a background pressure of 10⁻⁶ mbar. Sum of the Mass Spectra for individual ion states, indicated by dots, as the extraction time is varied and the corresponding shifted Maxwellian Fits.

The parameters obtained via fitting equation 5.2 and the kinetic energy calculated from the velocity distributions in the TOF curve are given in table 5.1:

Table 5.1:

	Zn ⁺	Zn ⁺⁺	Zn ⁺⁺⁺	O ⁺	O ⁺⁺	O ⁺⁺⁺
u (km s ⁻¹)	8.	13	13	16	30	39
T_i (eV)	5.17	5.56	4.31	3.88	8.6	6.9
E_K (eV)	7-47	21-31	19-22	5-77	19-87	21-58

There is also the possibility that the ionisation of N⁺ and O⁺ could arise due to Penning ionisation.

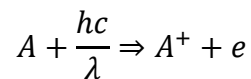


[5.3]

Where A and B are the ionisation potentials of two different charged particles.

For this reaction to occur we must have A >> B. For Zn the first ionisation potential is 9.39eV, this is not high enough to satisfy the above equation for nitrogen or oxygen. The second ionisation potential of Zn is 17.9eV, which could satisfy the equation. Similarly O⁺⁺ and O⁺⁺⁺ have ionisation potentials of 35.1 and 54.9eV respectively. This charge transfer would be in agreement with the collisional impact ionisation data presented above.

Finally, photoionisation is the physical process in which an incident photon ejects one or more electrons from an atom, ion or molecule.



[5.4]

The number of ionisation events caused by photoionisation is proportional to the radiation density [120]. The nature of this source of ionisation means that it would appear as an almost instantaneous ionisation of the ambient gas after the target is impacted with the laser radiation. To confirm this is not the source of ionisation both the N₂ and O₂ mass spectra have been reverse engineered into TOF profiles.

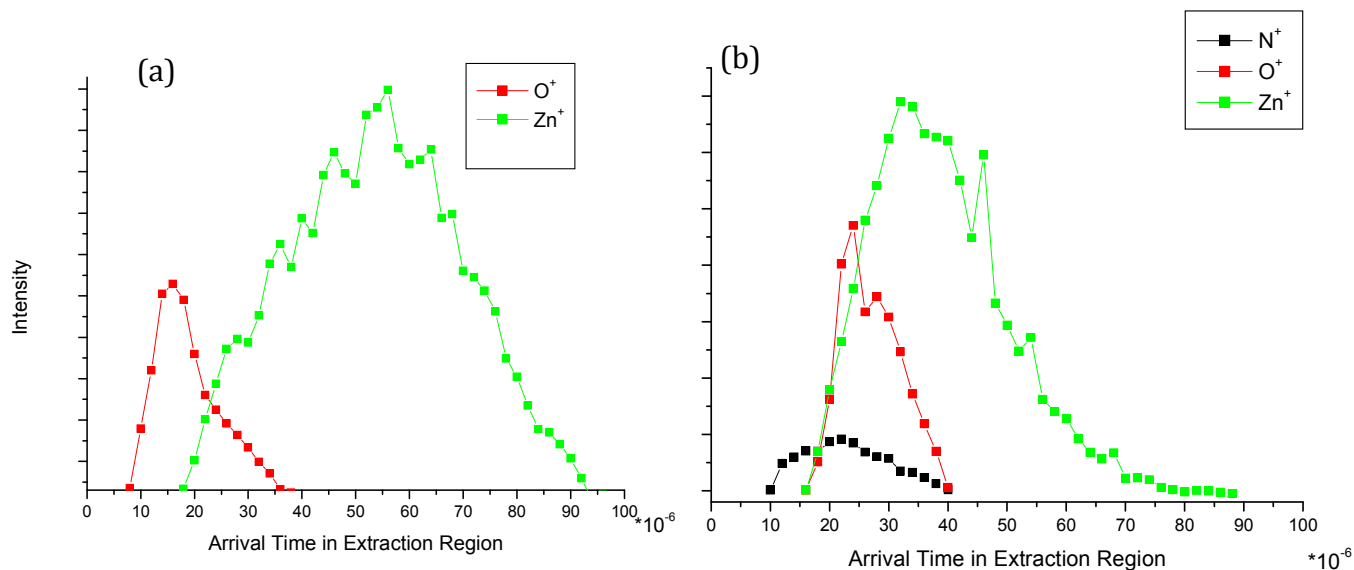


Figure 5.4 Sum of the Mass Spectra for individual ion states as the extraction time is varied, (a) corresponds to O_2 at 10^{-2} mbar, (b) corresponds to N_2 at 10^{-2} mbar.

Figure 5.4 clearly shows that the ionisation of the ambient nitrogen does not commence until $\sim 10 \mu s$, and the oxygen, whose origin is undistinguishable between the target and ambient in the O_2 atmosphere, commences at $\sim 8 \mu s$, neither of which are fast enough to be due to the UV radiation emitted from a laser ablation process. We may therefore rule it out as the cause of our ambient ionisation.

The ionisation of the ambient gas by the photoionisation processes was ruled out and instead an investigation of the collisional excitation of the gas species has been performed.

The data shows that the electron impact ionisation could be responsible for the ionisation of the ambient.

A collisional ionisation via charge transfer has been investigated and shown that the ionisation of the ambient via a collisional ionisation with Zn^{++} , O^{++} and O^{+++} , could answer the ionisation of our ambient. Equation 5.3 says that the charge transfer results in the release of an electron. This implies that, if the ionisation of the ambient was to occur from a charge transfer then the electron density in the ambient atmosphere would be higher than that in a vacuum situation. This was observed via a saturation of the ion probe signal at relatively

low voltages, $\sim 150\text{V}$, whereas in the vacuum situation the probe could be set as high as 1kV with no saturation of the electron signal output to the oscilloscope.

Finally no plume splitting was detected by means of the mass spectrometer, indicating that the possibility of some of the plume reaching a distance of 55 cm from the target in an ambient gas pressure of 10^{-2} mbar , without colliding with this ambient, does not occur in our system for these conditions.

5.2 Mass spectrometry analysis of ZnO:

As discussed in chapter 2, the ionisation of a solid target by the impact of laser radiation is strongly dependent on the wavelength of the laser radiation, both for the penetration depth, equation 2.5 and for the possibility of direct photoionisation, equation 2.6.

Two general regimes are usually analysed by inorganic chemists via mass spectrometry, laser ablation and laser desorption. Laser desorption is in effect the technique used in MALDI TOF systems whereby there is little disturbance of the surface being analysed. For our own interests, laser ablation, which involves the large scale disturbance of the target surface, is analysed for two regimes, the high fluence regime, and the low fluence regime which is of interest for material depositions.

There has also been publications in which the importance of the laser fluence has been discussed in relation to the composition of recorded mass spectra, for example, an increase in cluster size of ZnSe as the fluence was increased, observed by Kukreja et al. [15].

For a thorough investigation of these phenomena, our system allowed the variation of a number of different parameters, the fluence, easily adjustable using a combination of the half wave plate and Brewster's window discussed in the experimental design section, chapter 2; the wavelength, easily changeable via the harmonic generation of the laser from 1064nm to 532 nm or 355 nm or 266 nm; and finally as discussed above the atmospheric conditions when generating the plasma, easily varied using a combination of pumping speed and gas flow rate to within 1 sccm via mass flow controller.

5.3 Laser ablation of ZnO via 1064 nm:

5.31 High Fluence Regime Pressure Scans:

Figure 5.5 shows mass spectra taken in a high fluence regime of 70 J/cm², calculated from a laser energy of ~600 mJ focused to a spot size of radius ~0.5mm. The spectra was taken with the turbomolecular pump running at half speed, ~450 rps, in a gas pressure of 10⁻⁵ mbar, nearing the base pressure of the system, with no O₂ flow, similar to that discussed earlier. There are clearly no clusters recorded, the heaviest ion being that of Zn⁺. Multiple charged states of both Zn and O were recorded up to Zn⁺⁺⁺ and O⁺⁺⁺.

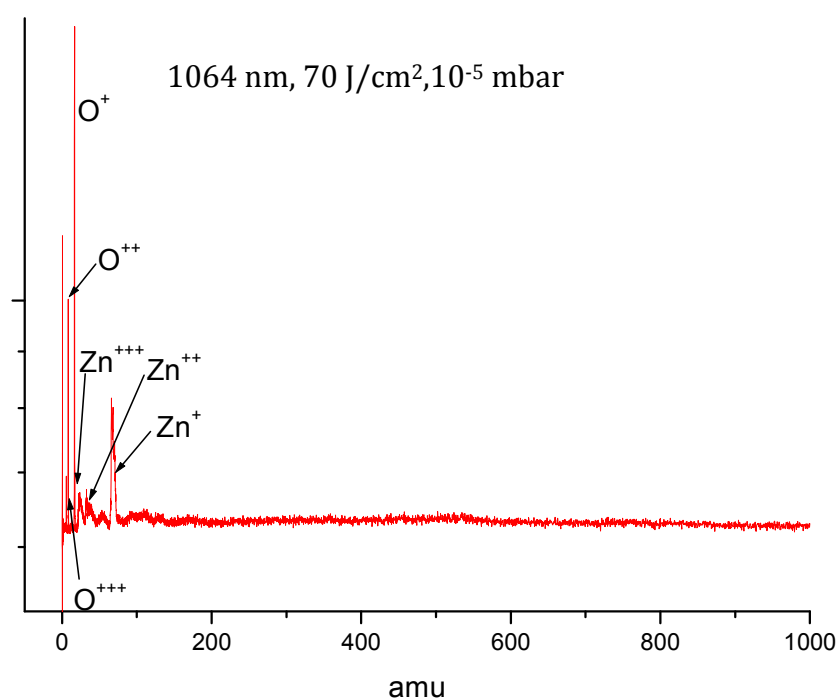


Figure 5.5: Mass spectra of a laser ablated ZnO target, 1064 nm, high fluence regime, base pressure conditions, 10⁻⁵ mbar.

Figure 5.6 shows the exact same conditions, laser wavelength and fluence, and pumping speed but with the introduction of O₂ at a rate of 5 sccm.

The gas purge valve at the back of the turbo pump was also switched on, this is essentially the introduction of nitrogen gas to the back end of the pump

in order to cool the pump's bearing, which begin to struggle at higher gas pressures. The time of flight chamber pressure increased to $1.9 \cdot 10^{-7}$ mbar.

The most obvious difference is the fact that it has a "tail" in the higher mass region. This may indicate the presence of larger masses, and is consistent with published data by A. Burnin et al. and A. Dmytruk et al. [123, 116]

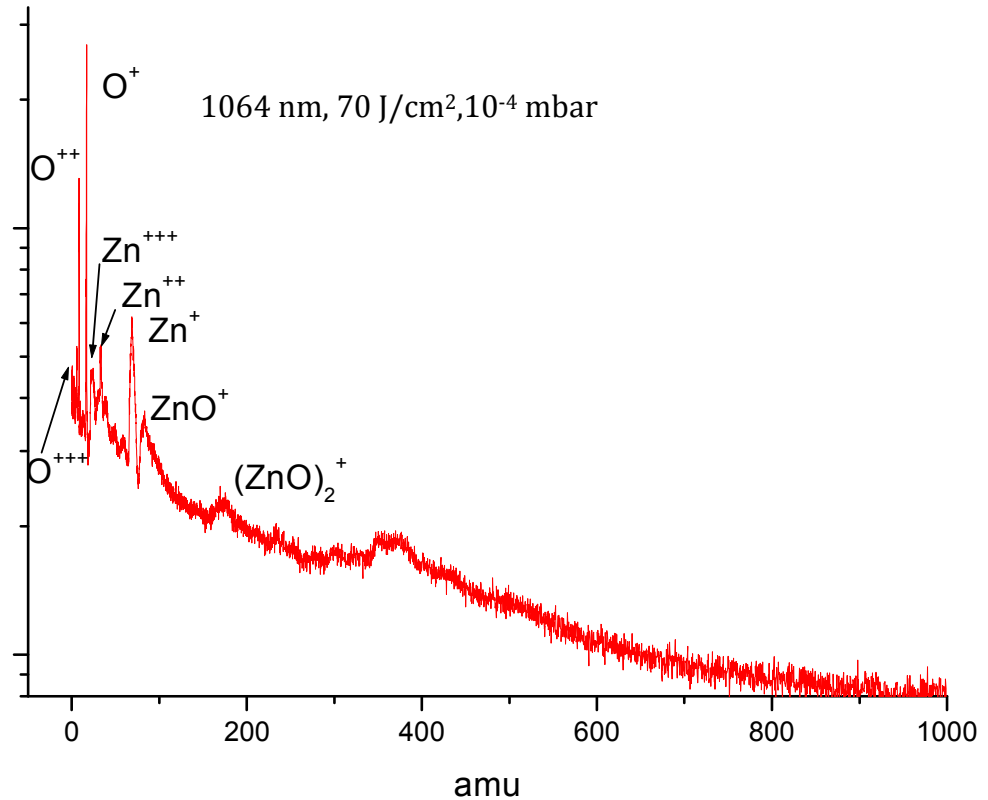


Figure 5.6: Mass spectra of a laser ablated ZnO target, 1064 nm, high fluence regime, O₂ flow at 5 sccm.

The next most striking result from adding a relatively small amount of gas is the addition to the mass spectra of what appears to be ZnO at ~81 amu, and what appears to be a singly ionised (ZnO)₂ cluster peak at ~165 amu. There also appears to be the formation of a broad peak at ~350 – 370 amu which could be (ZnO)₄.

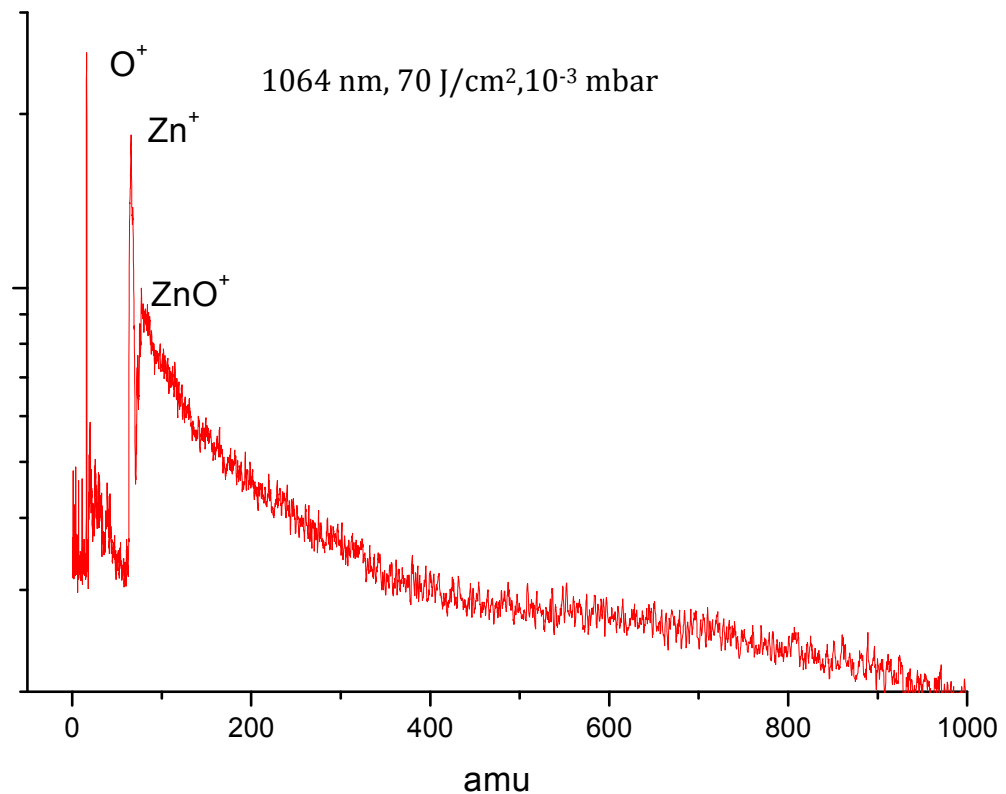


Figure 5.7: Mass spectra of laser ablated ZnO target, 1064 nm, high fluence regime, O₂ flow at 17 sccm.

As the pressure is increased via the mass flow controller to 17 sccm, the chamber reaches a pressure of 10⁻³ mbar. The effect on the mass spectra, figure 5.7, is to decrease the amount of charged states detected, to overall increase the noise and produce a long tail or discharge of the MCP. This is assumedly due to the high gas pressure on the MCP which is 1*10⁻⁶ mbar for a chamber pressure of 10⁻³ mbar. This assumption is made as the ZnO peak at 81 amu tails off, whereas if there were clusters, the first possible cluster state would be seen at ~97 amu, that of zinc peroxide, ZnO₂, followed by ~130 amu, a zinc dimer. These masses should be resolved by the mass spectrometer but the fact that the “tail” does not deviate from its decreasing slope indicates that they are not present.

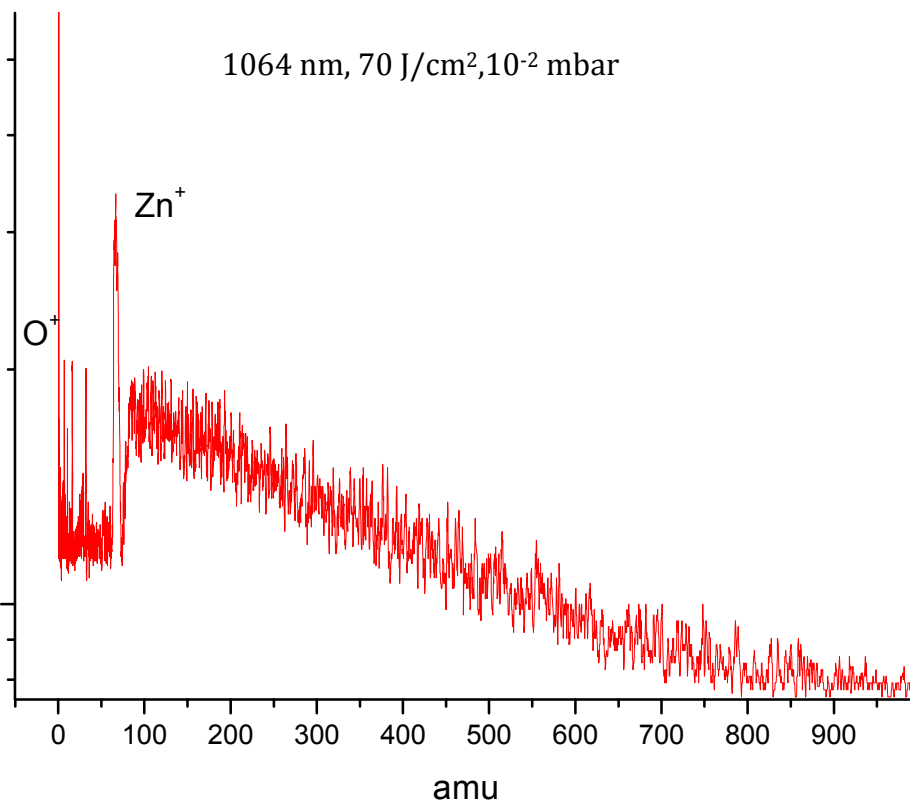


Figure 5.8: Mass spectra of laser ablated ZnO target, 1064 nm, high fluence regime, O₂ flow at 22 sccm.

The highest gas pressure obtainable in the plasma chamber, while maintaining the recommended operational pressure for the MCP in the ReTOF chamber, was $5 \cdot 10^{-2}$ mbar. This pressure was obtained by a flow of 22 sccm of O₂ via the mass flow controller, giving a ReTOF pressure of $4 \cdot 10^{-6}$ mbar.

Figure 5.8 is the mass spectra obtained for this pressure. A large reduction in the O⁺ signal is observed with a comparative increase in the Zn⁺ signal. The increase in the Zn⁺ signal indicates that the signal is real and not due to the increased pressure on the MCP. As discussed in previous sections, for this pressure and comparative fluences, the oxygen atmosphere is ionised by processes in the plasma. The fact that the signal decreases even though the presence of the same element increases is an indication of recombination of the charged species.

5.32 Low Fluence Regime Pressure Scans:

Figure 5.9 shows the mass spectrum obtained by the ablation of the ZnO target with no flow of O₂, in the vacuum regime, with the 1064 nm laser radiation. The threshold of ablation of ZnO is ~0.44J/cm² [121], for this reason the fluence of ablation was reduced to 0.7 J/cm² by setting the laser energy to ~6 mJ and maintaining the laser spot radius at 0.5mm.

The reduction in Laser fluence has an immediate effect on the noise in the signal and signal strength. Again no molecular ZnO is seen, rather the first and second ionisation states of Zn and O are seen. Comparing this to the high fluence regime, the signal intensity has certainly dropped off as would be expected, and there also appears to be less charge states of both Zn and O. These very slight differences in the mass spectra obtained suggest that there is no fundamental difference between the laser produced plasma at 0.7 J/cm² and 70 J/cm².

Figure 5.10 is again keeping the previous settings constant but with a variation of the gas pressure by flowing O₂ at a rate of 5 sccm. From the previous spectra there is a clear development of a tail end of the spectra and also the appearance of a zinc peroxide (ZnO₂) peak. This tail is in keeping with the spectra obtained for the higher fluence regime but the spectra is less rich in identifiable peaks detected.

The signal is reduced by an increase of the gas pressure to 10⁻³ mbar via a flow rate of 17 sccm of O₂, figure 5.11. The signal is for the most part noise, except for a peak standing out above the noise level corresponding to 65 amu, that of Zn⁺. This at first seems surprising as the ionisation of oxygen would seem more likely in an O₂ atmosphere. The reduction in the Zn⁺ yield could be explained by a reduction of metal valence state, [122] in the O₂ atmosphere.

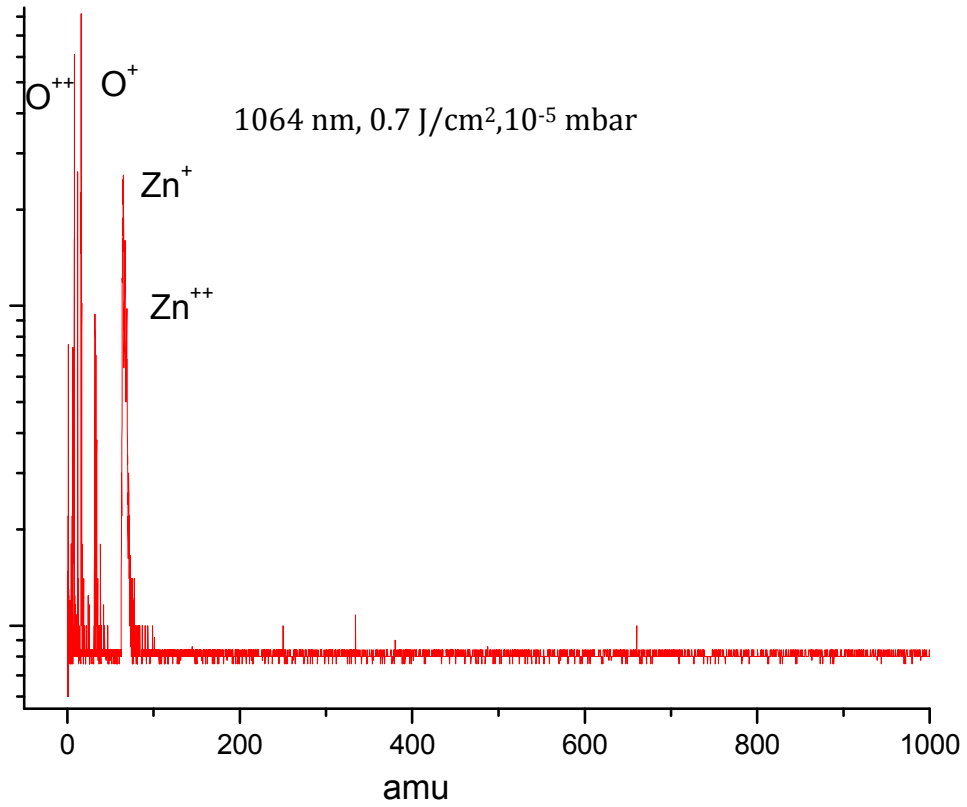


Figure 5.9: Mass spectra of ZnO, 1064 nm, low fluence regime, base pressure conditions.

Inset with y-axis set to log scale.

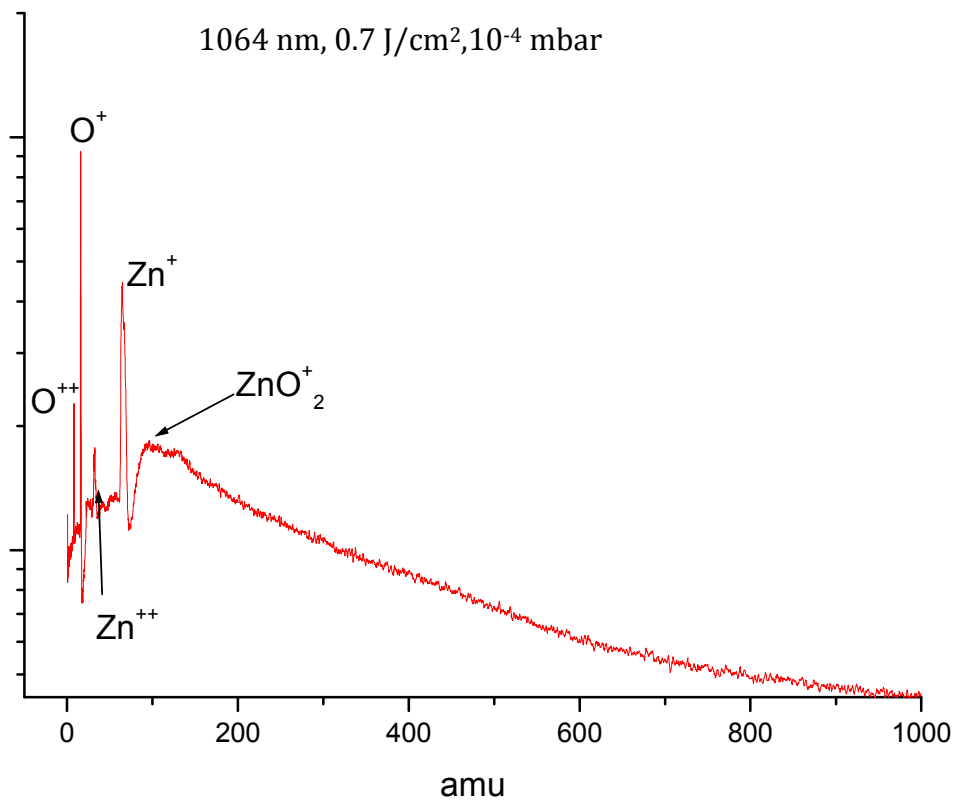


Figure 5.10: Mass spectra of ZnO, 1064 nm, low fluence regime, O_2 flow at 5 sccm. Inset with y-axis set to log scale.

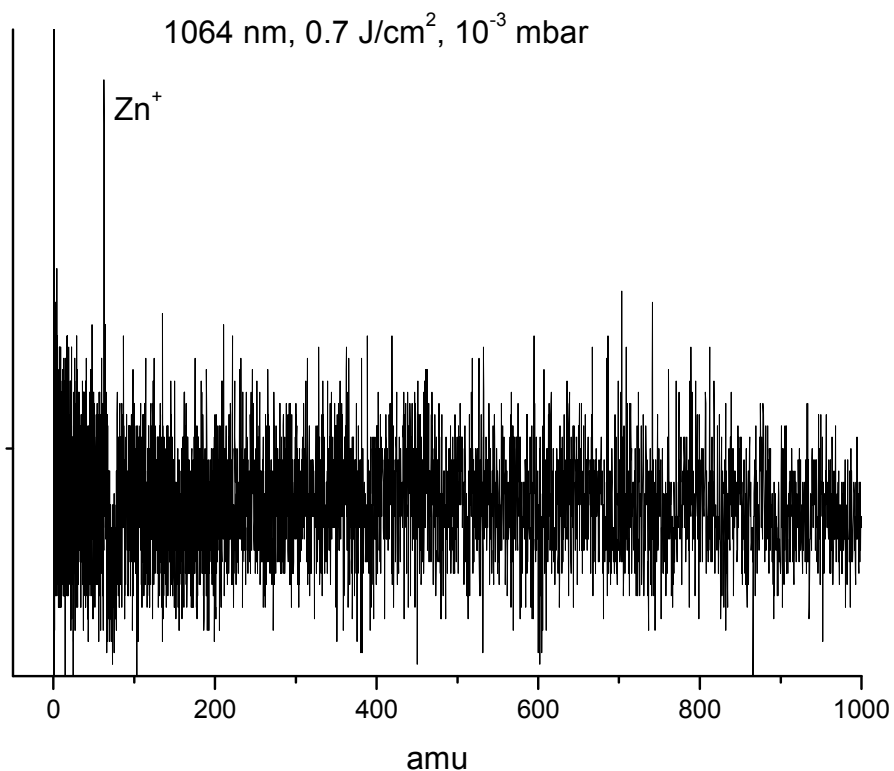


Figure 5.11: Mass spectra of ZnO, 1064 nm, low fluence regime, O₂ flow at 17 sccm.

Increasing the pressure still further led to a disappearance of all signal, figure 5.12, assumedly due to the complete recombination or confinement of the plasma in the low fluence high pressure regime.

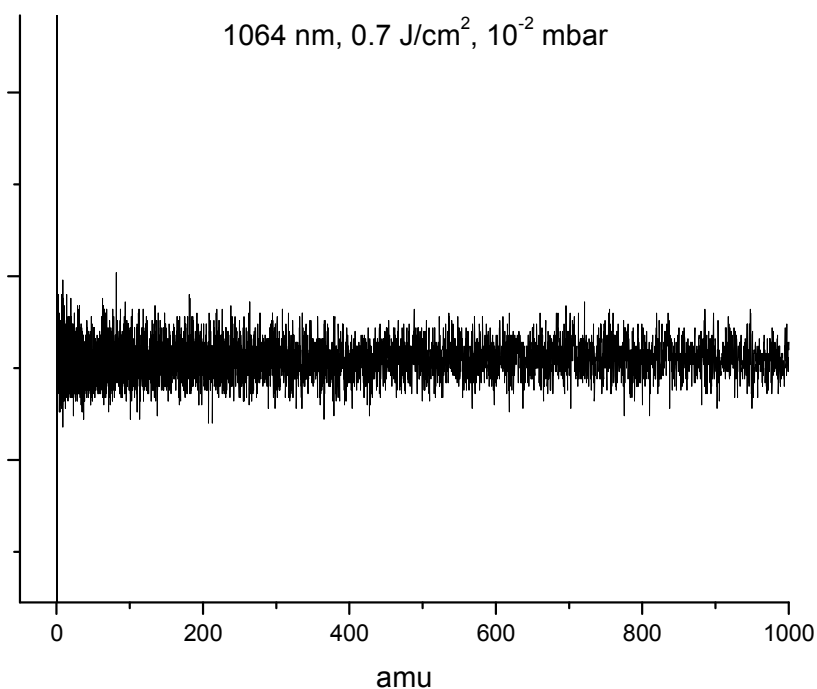


Figure 5.12: Mass spectra of ZnO, 1064 nm, low fluence regime, O₂ flow at 22 sccm.

5.4 Laser ablation of ZnO via 532 nm:

5.4.1 High Fluence Regime Pressure Scans:

The ablation of the ZnO target by the frequency doubled NdYAG laser in our base pressure regime for the highest fluence obtained by not changing the spot size of ablation, from the 1064 nm ablation, is presented in figure 5.13. The maximum laser output at this wavelength was 200 mJ on target without focusing. The focus lens brought the spot size to a diameter of 1 mm resulting in a fluence of 25 J/cm².

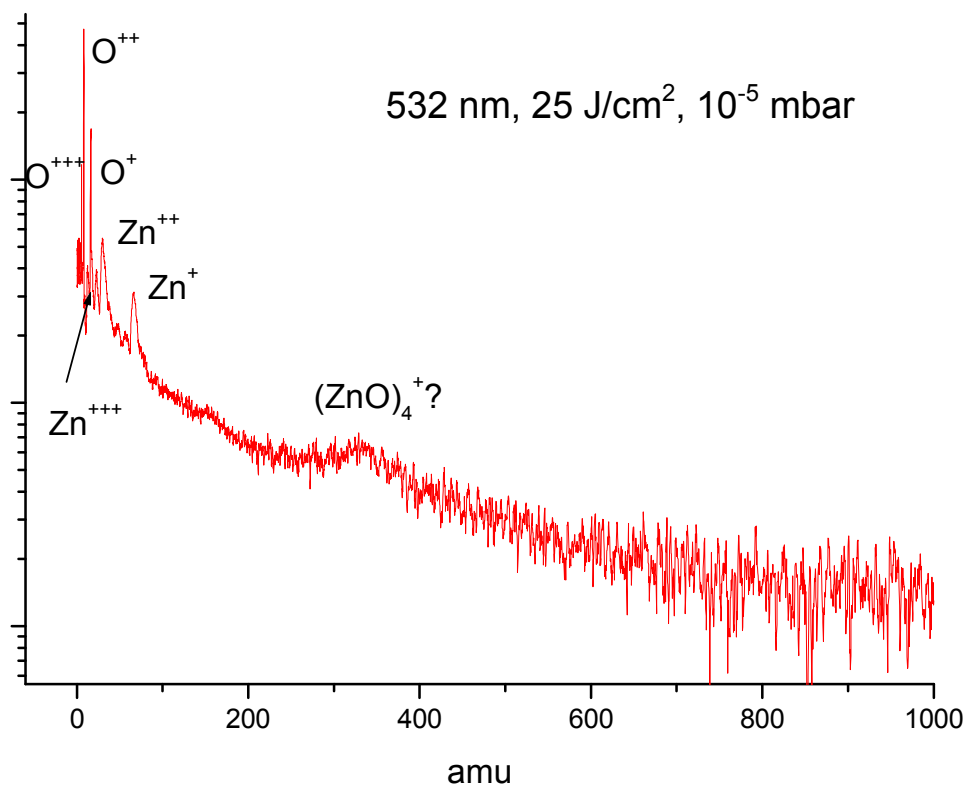


Figure 5.13: Mass spectra of ZnO, 532 nm, high fluence regime, base pressure conditions.

The mass spectrum obtained are quite similar to those presented by Sage et al. [109] for the same fluence range and vacuum pressure of ZnO except that the spectra presented here shows the third ionisation stage of O⁺⁺⁺ and possibly a (ZnO)₄⁺ cluster at ~320 amu. However Sage et al. do not present mass above 80 amu in their spectra.

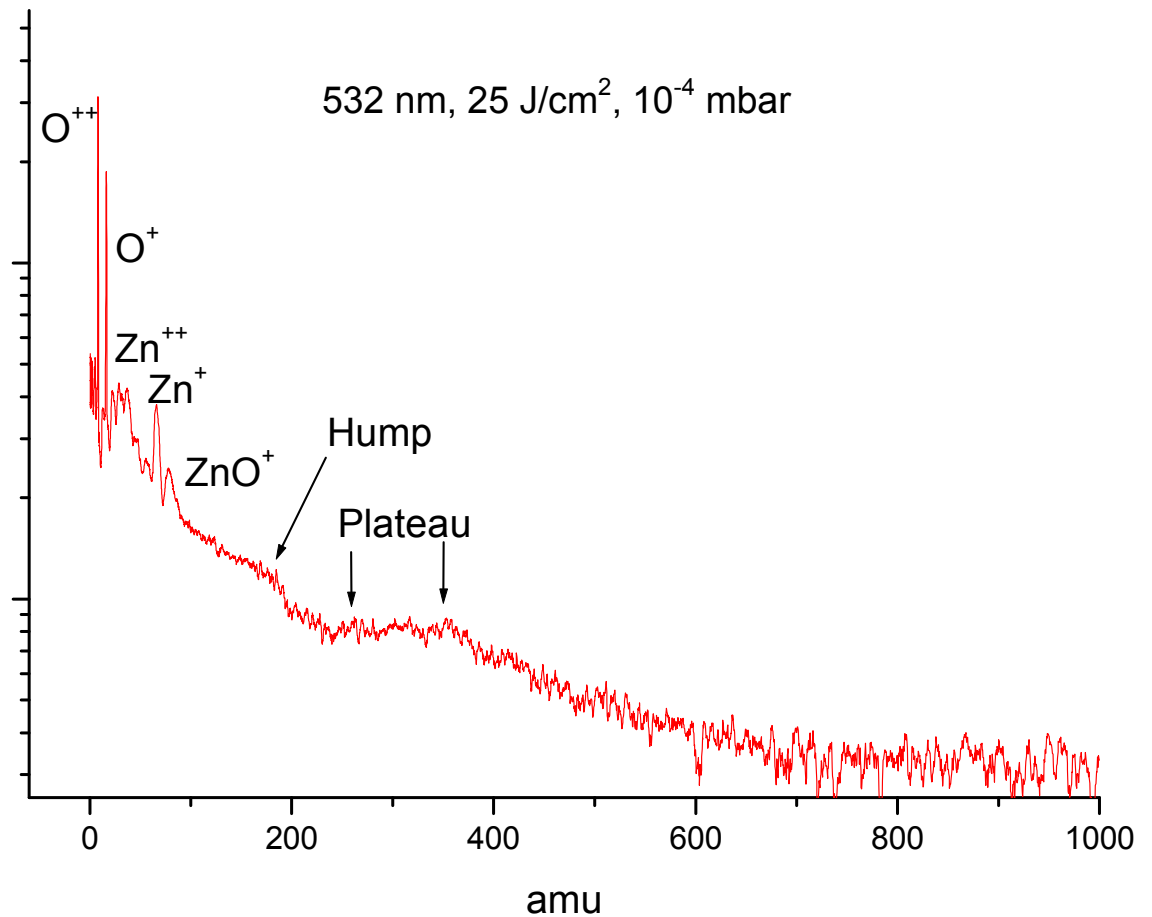


Figure 5.14: Mass spectra of ZnO, 532 nm, high fluence regime, O₂ flow at 5 sccm.

Figure 5.14, taken at 10^{-4} mbar of O₂, shows the presence of double charged Zn and O with singly charged ZnO, Zn and O. there also appears to be a “hump” where $(\text{ZnO})_2^+$ would be expected and a plateau region from where $(\text{ZnO})_3^+$ to $(\text{ZnO})_4^+$ could be found.

Figure 5.15 is an increase of the pressure to 10^{-3} mbar, the multi-charged states previously present have now gone, with the appearance of a long tail in the mass spectra. Singly charged O, Zn, ZnO and possibly a ZnO₂ ion are visible.

Finally in the high fluence regime for the 532 nm radiation a flow of 22sccm was introduced to the chamber and this spectrum is depicted in figure 5.16. The only ion clearly visible is that of singly ionised Zn. Again this may be due to the recombination of the ionised species in the higher background gas pressure.

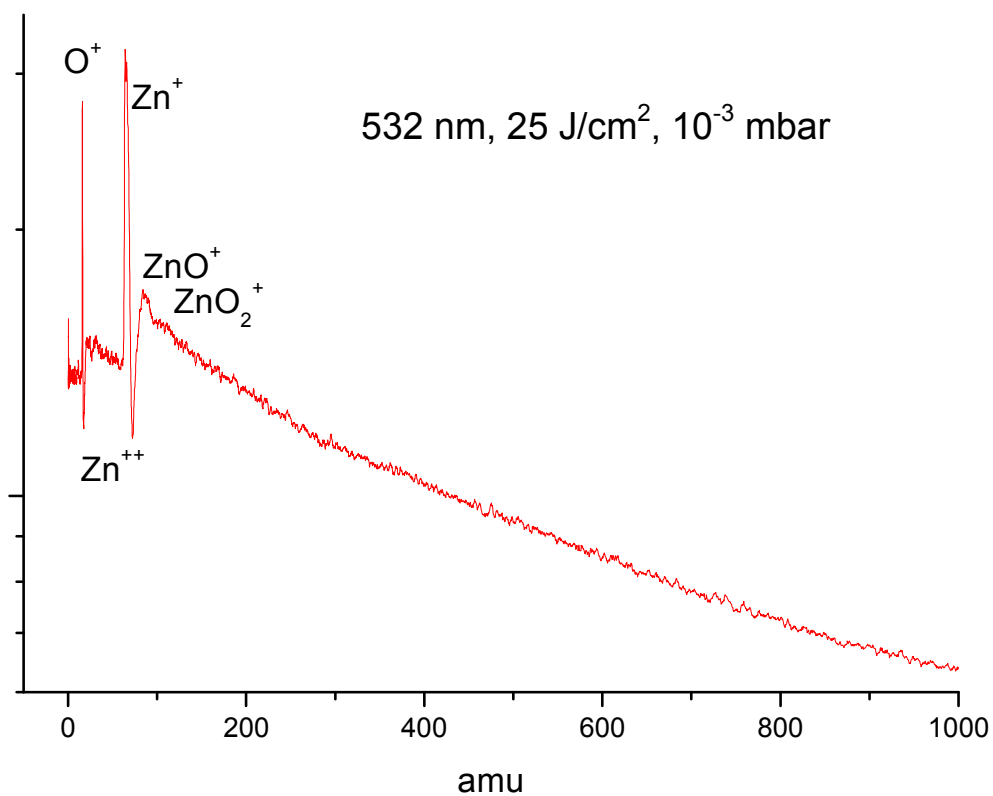


Figure 5.15: Mass spectra of ZnO, 532 nm, high fluence regime, O₂ flow at 17 sccm.

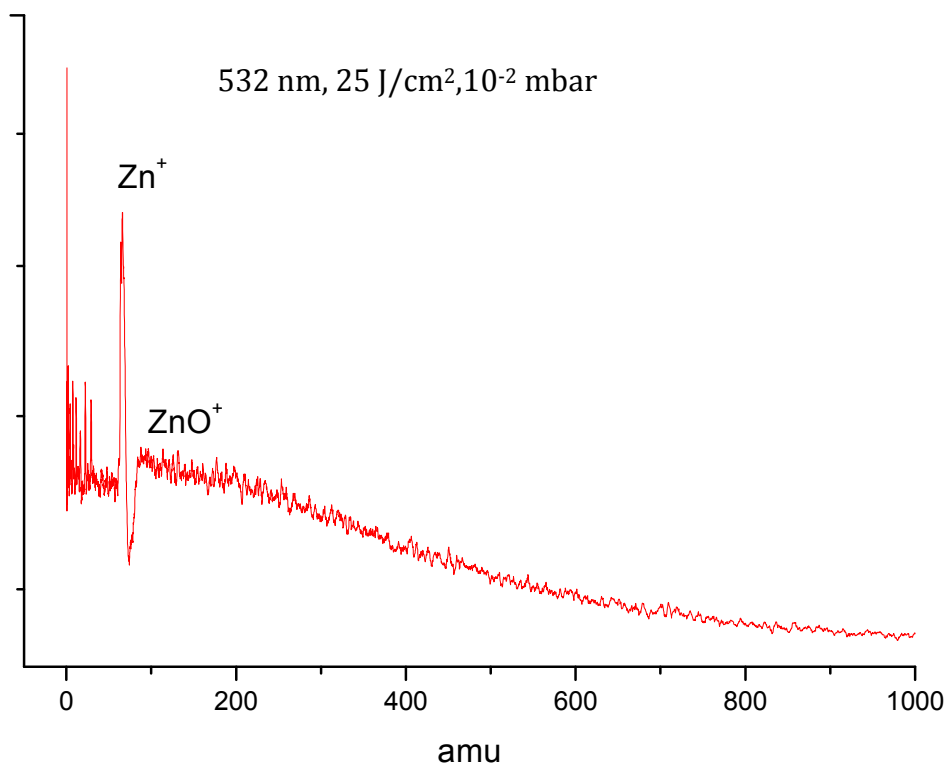


Figure 5.16: Mass spectra of ZnO, 532 nm, high fluence regime, O₂ flow at 22 sccm

5.42 Low Fluence Regime Pressure Scans:

Figure 5.17 is comparable to figure 5.09, with the only difference being that of the laser wavelength. As before no molecular ZnO is seen, the first ionisation states of Zn and O are seen however the second ionisation states are not.

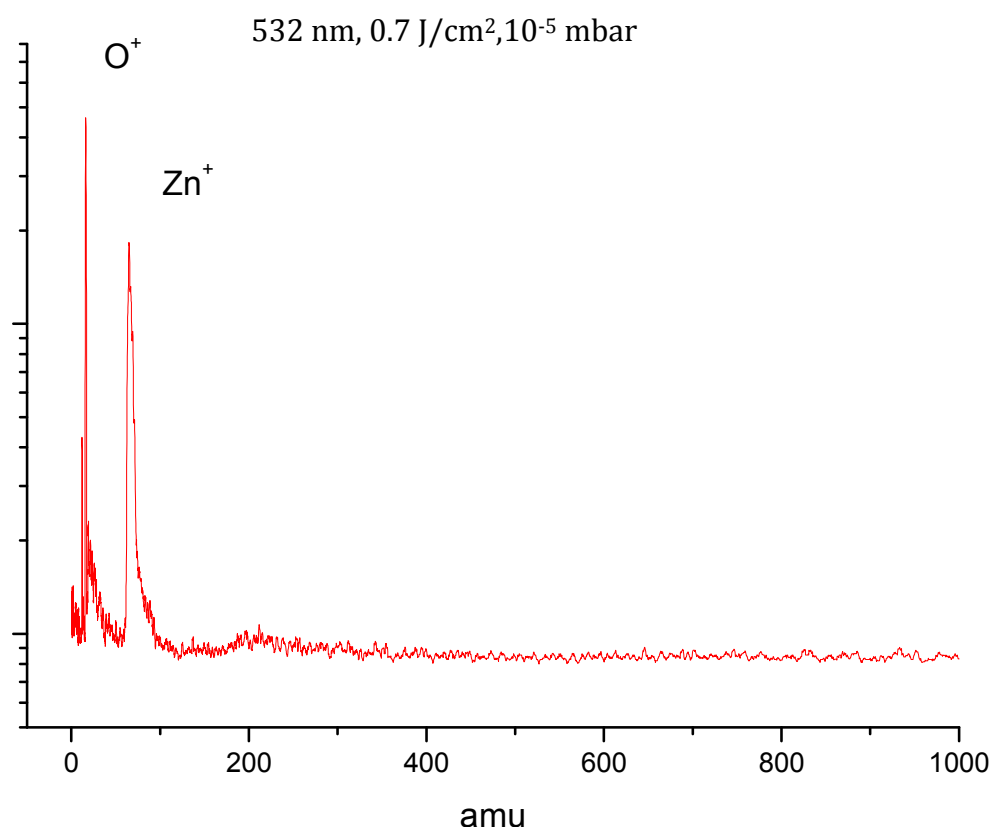


Figure 5.17: Mass spectra of ZnO, 532 nm, Low fluence regime, base pressure conditions

Figure 5.18, is the mass spectra with increasing O₂ pressure to 10⁻⁴ mbar, shows the appearance of a ZnO⁺ peak as well as the formation of a tail on the mass spectra, which becomes again more pronounced as the gas pressure is increased to 10⁻³ mbar, figure 5.19.

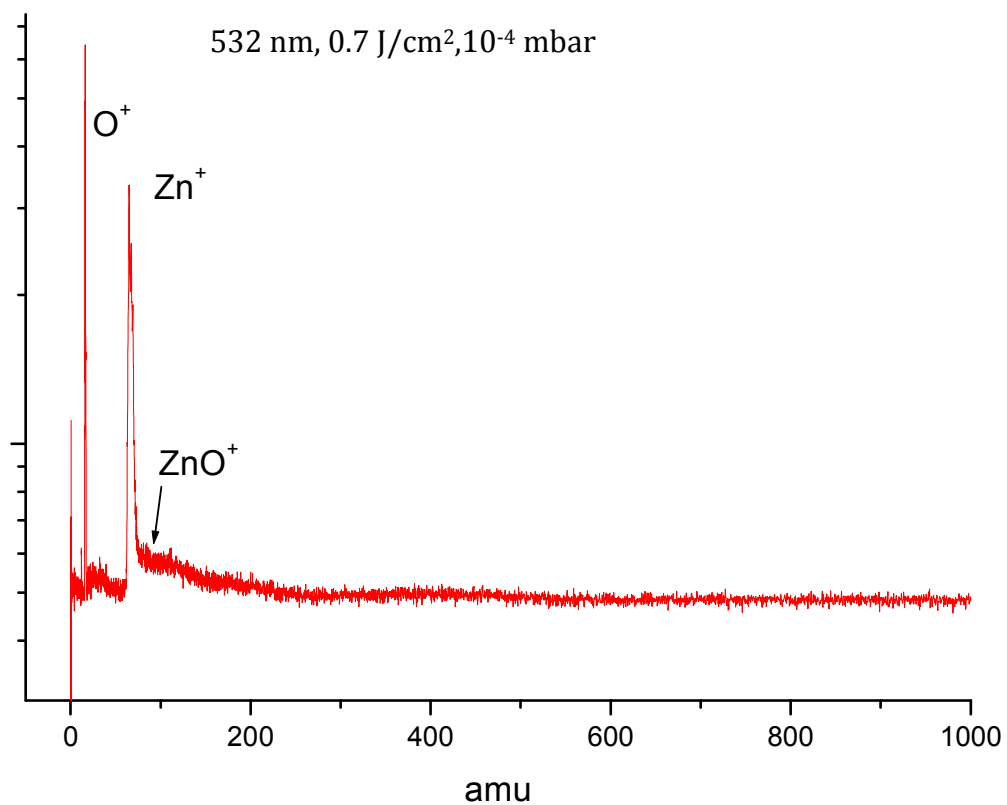


Figure 5.18: Mass spectra of ZnO, 532 nm, Low fluence regime, 10⁻⁴ mbar, 5 sccm flow O₂.

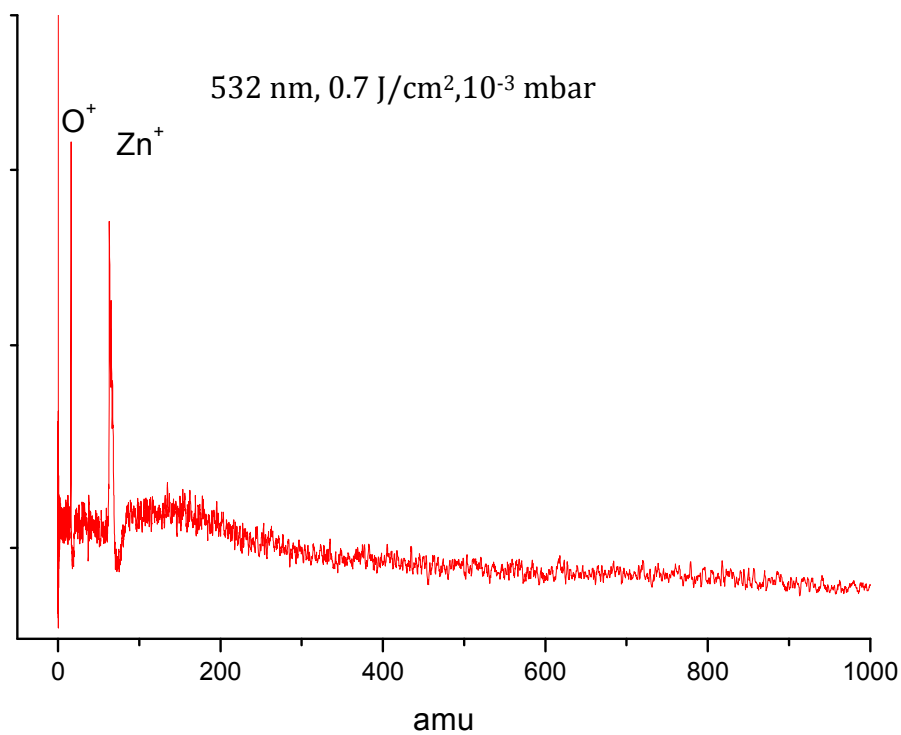


Figure 5.19: Mass spectra of ZnO, 532 nm, Low fluence regime, 10⁻³ mbar, 17 sccm flow O₂.

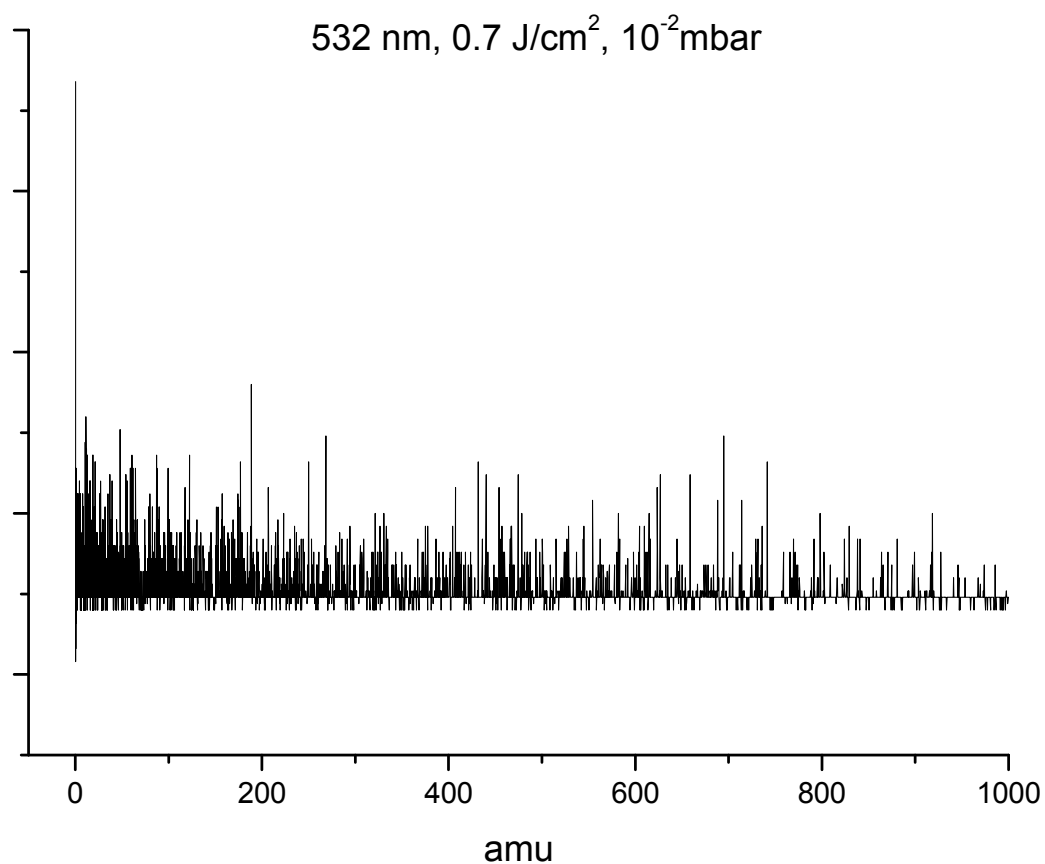


Figure 5.20: Mass spectra of ZnO, 532 nm, Low fluence regime, 10⁻² mbar, 22 sccm flow O₂.

Figure 5.20 again shows the disappearance of detected mass peaks, similar to the situation observed for the same conditions with a 1064 nm radiation at the same fluence.

5.5 Laser ablation of ZnO via 355 nm:

5.51 High Fluence Regime Pressure Scans:

The laser, when frequency tripled resulted in a maximum output of 100 mJ at 355 nm. Due to losses at the mirrors this energy dropped to 60 mJ at the target surface. The corresponding maximum fluence, with the focal spot kept at the same ~ 1 mm diameter, was ~ 7 J/cm².

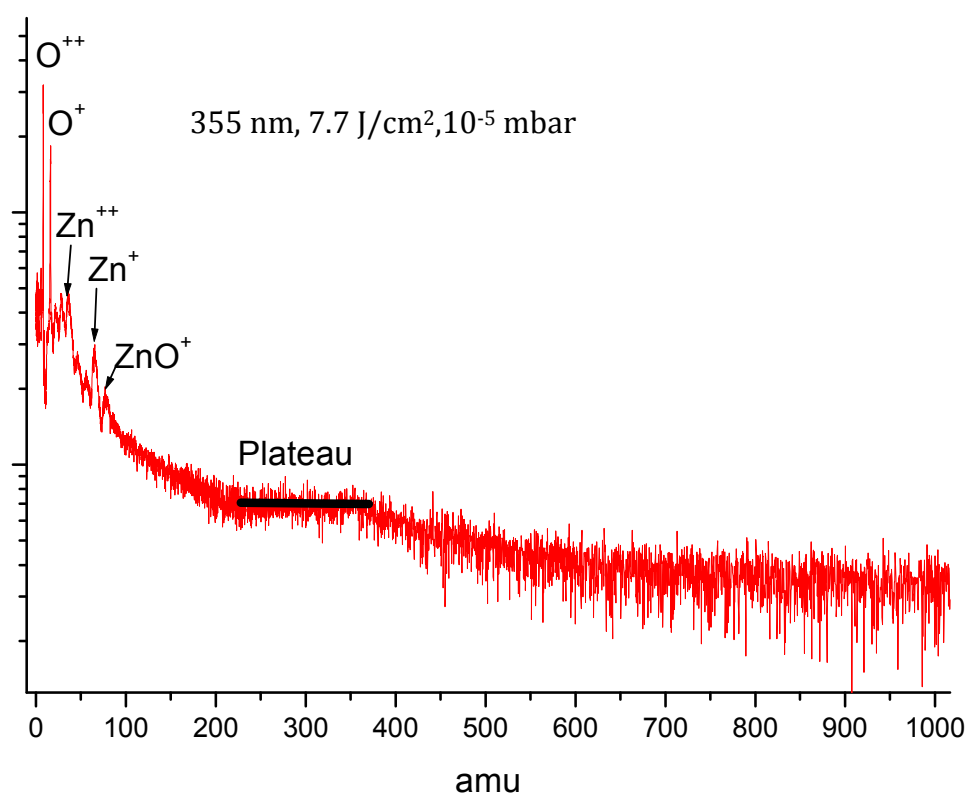


Figure 5.21: Mass spectra of ZnO, 355 nm, highest fluence regime, 10⁻⁵ mbar, base pressure.

The mass spectra obtained here results in singly ionised O, Zn and ZnO with the double ionisation of O and Zn, the presence of clusters is also likely given the shape of the “tail”. Also the plateau is again observed.

An increase of the O₂ pressure as before, figure 5.22, reduces the O⁺⁺ to O⁺ ratio, and also appears to increase the plateau to a measurable peak at 381 amu, the closest possible state to this is the 4th cluster of zinc peroxide.

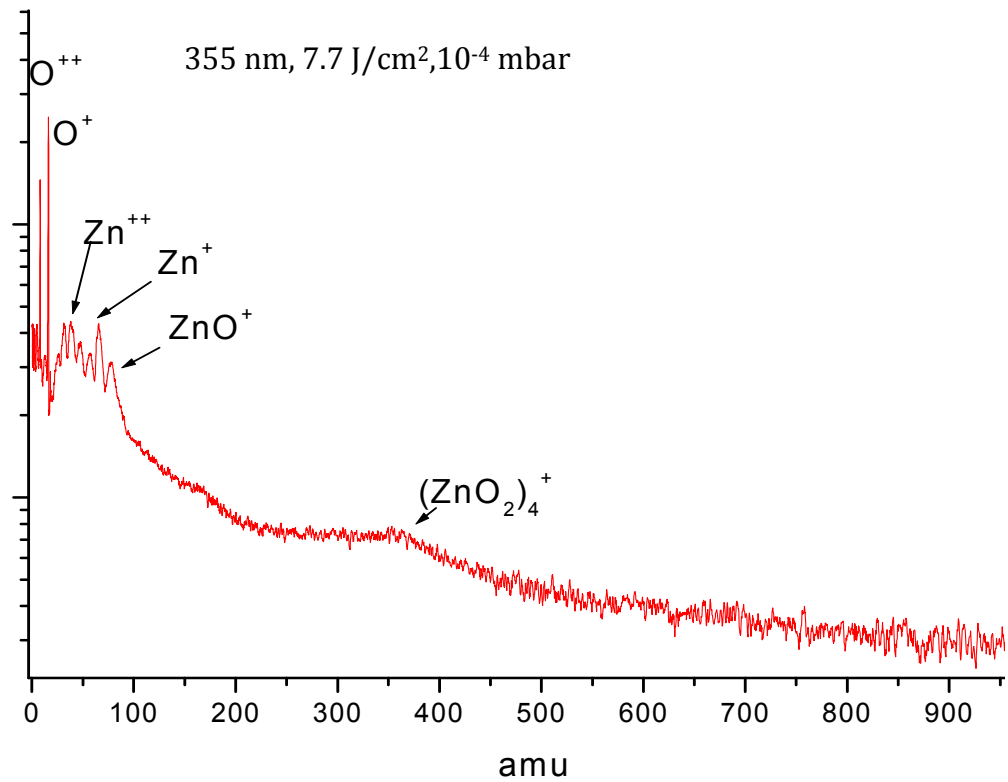


Figure 5.22: Mass spectra of ZnO, 355 nm, highest fluence regime, 10⁻⁴ mbar, base pressure.

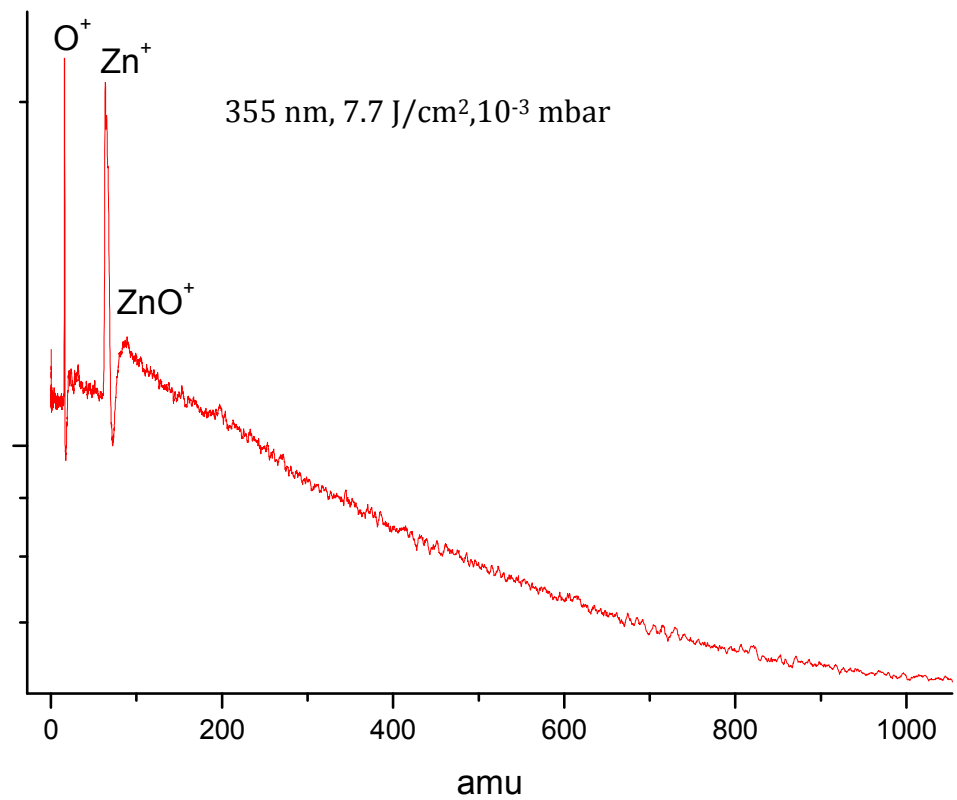


Figure 5.23: Mass spectra of ZnO, 355 nm, highest fluence regime, 10⁻³ mbar, O₂ flow at 17 sccm.

Still further increasing the pressure in the system results in mass spectra where only Zn^+ is visible. Figure 5.23, in keeping with results obtained for the higher fluence 532 nm regime.

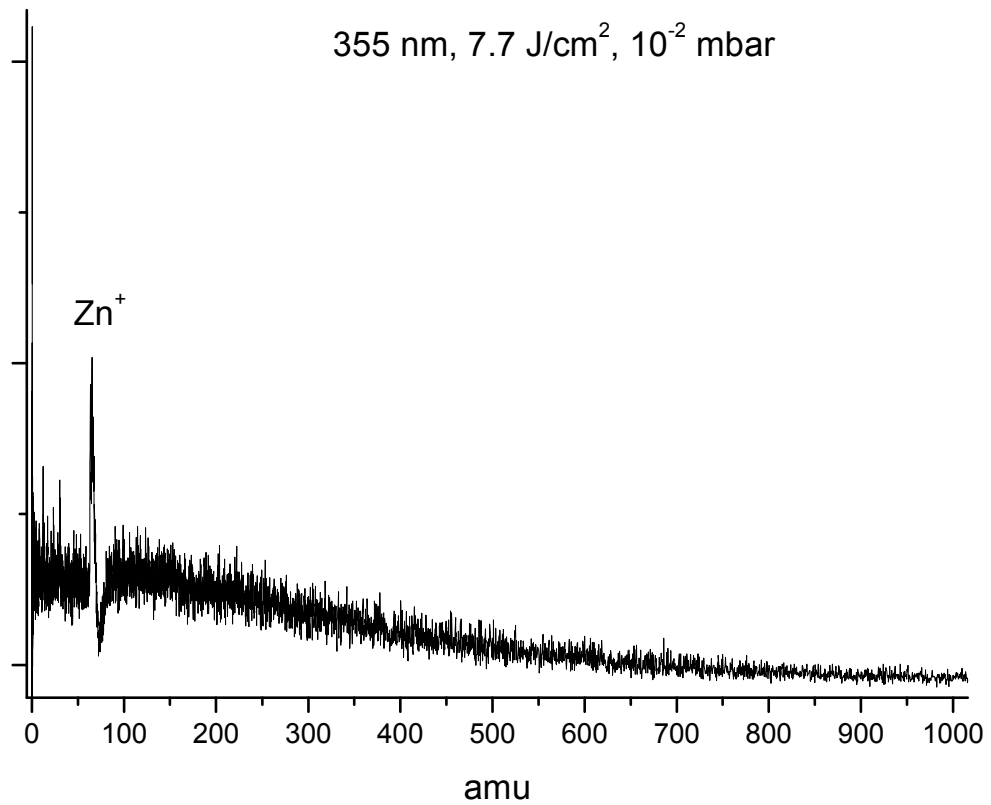


Figure 5.24: Mass spectra of ZnO, 355 nm, highest fluence regime, 10⁻² mbar, O₂ flow at 22 sccm.

5.51 Low Fluence Regime Pressure Scans:

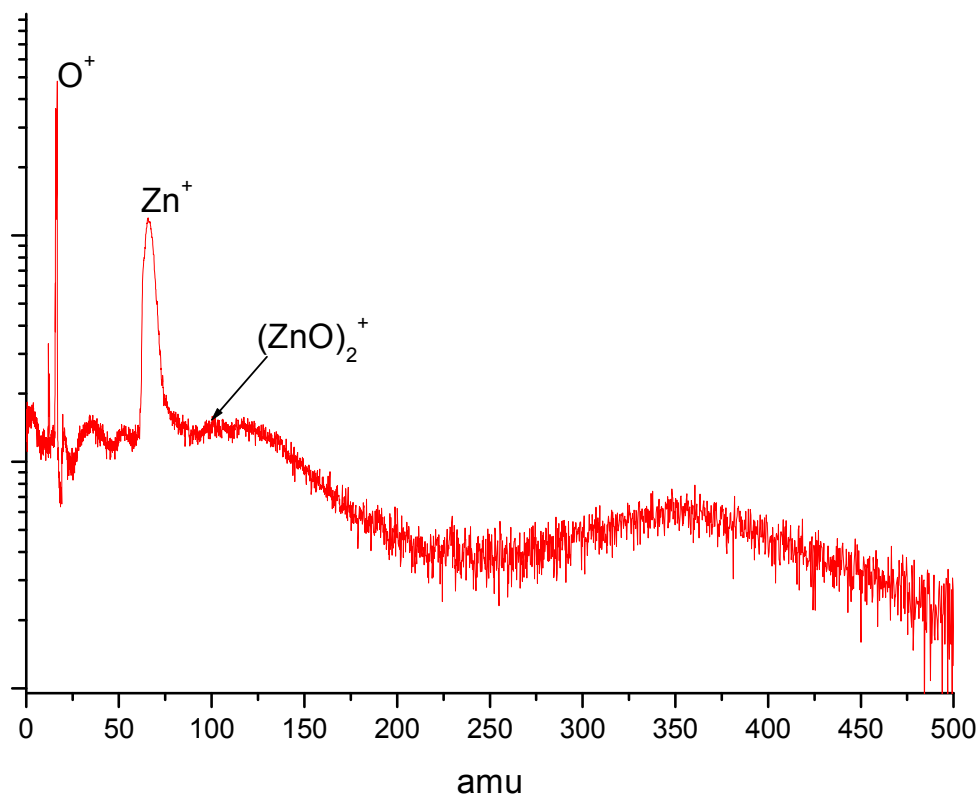


Figure 5.25: Mass spectra of ZnO, 355 nm, low fluence regime, base pressure.

A trend of increasing signal at higher mass range is beginning to become apparent in the shorter wavelength laser ablation, low fluence conditions. Comparing figures 5.9, 5.16 and now 5.25, the only difference is the wavelength, but whereas figure 5.11 is free from any signal heavier than that of Zn^+ there is the detection of some signal for the 532 nm radiation seen in figure 5.16 and ultimately the formation of a peak can be seen at the 355nm ablation in figure 5.24, at ~ 380 amu. The presence of this peak is again seen as some oxygen is introduced to bring the pressure to 10^{-4} mbar, figure 5.26.

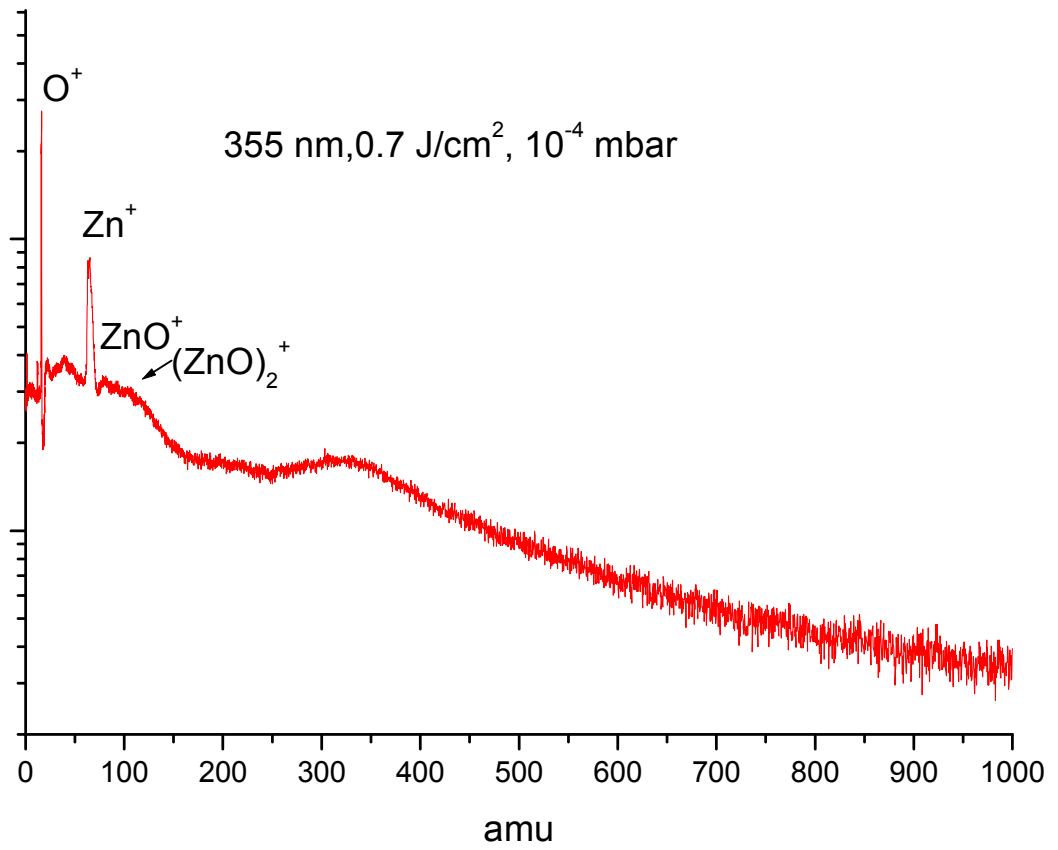


Figure 5.26: Mass spectra of ZnO, 355 nm, low fluence regime, 10⁻⁴ mbar O₂ flow at 5 sccm.

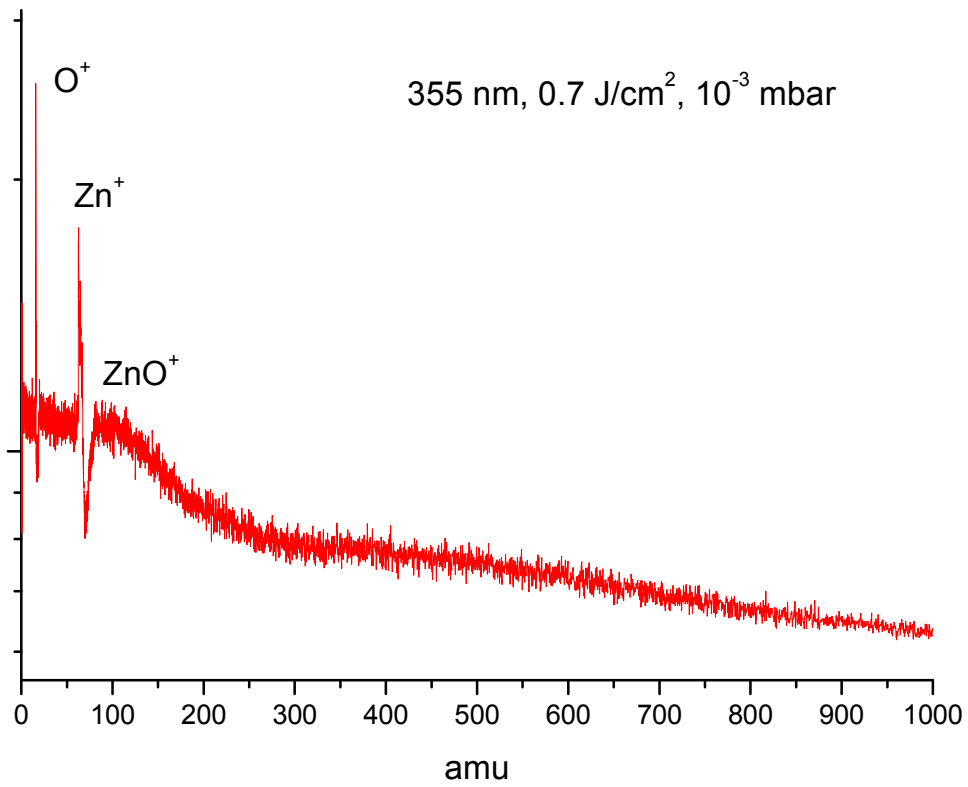


Figure 5.27: Mass spectra of ZnO, 355 nm, low fluence regime, 10⁻³ mbar O₂ flow at 17 sccm.

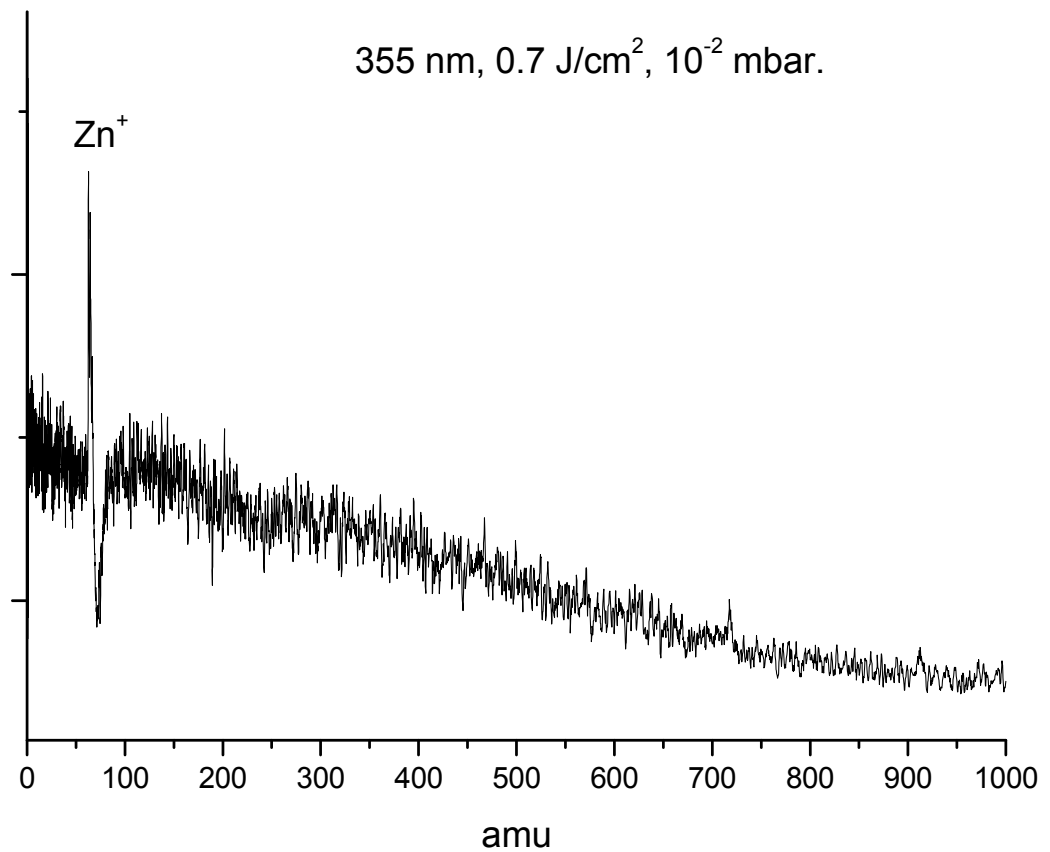


Figure 5.28: Mass spectra of ZnO, 355 nm, low fluence regime, 10⁻² mbar O₂ flow at 22 sccm.

Further increasing the O₂ pressure again reduces the amount of ionised material detected by the mass spectrometer however as seen before in the highest pressure obtainable in the system, 10⁻² mbar, the 1064nm and 532 nm radiation at 0.7 J/cm² did not result in a single mass peak. Figure 5.28 clearly produces a mass peak corresponding to Zn⁺.

5.4 Ionisation of a ZnO target via 266 nm Laser Radiation:

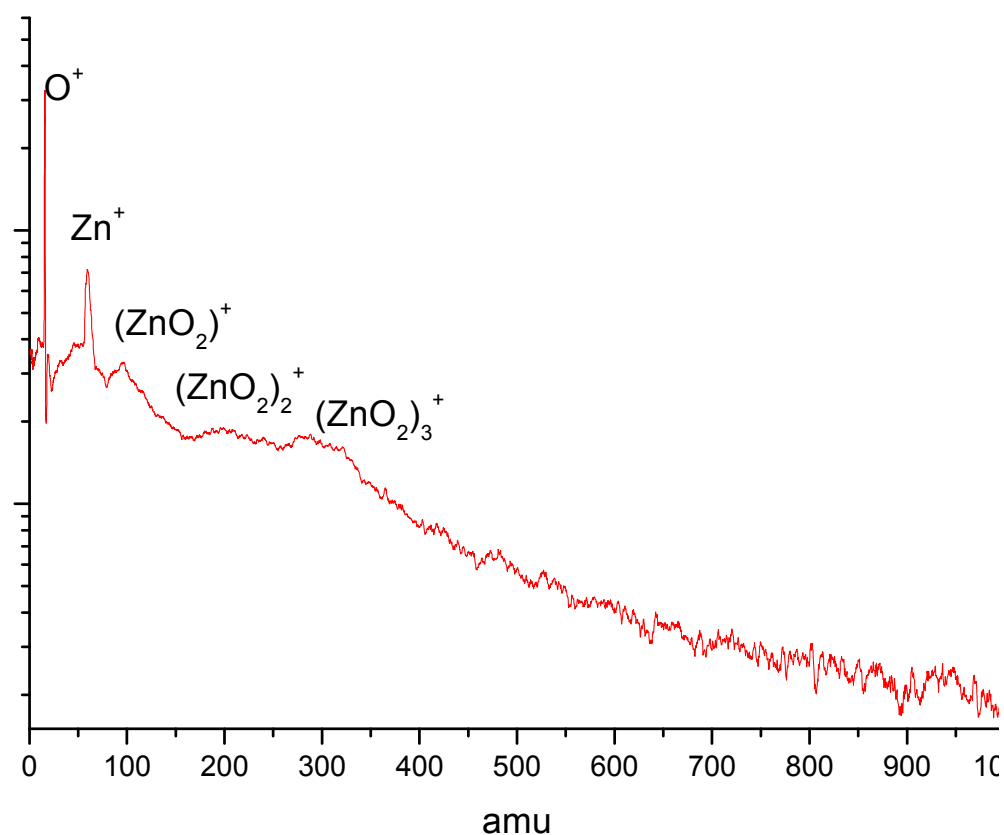


Figure 5.29: Mass spectra of ZnO, 266 nm, base pressure.

Figure 5.29 represents the mass spectra obtained by the ablation of the 5 N purity ZnO ceramic disc target, with a 266 nm, fourth harmonic Surelite I, Nd:YAG laser, operating at a maximum energy of 30 mJ measured at the laser head. In our optical setup, this energy is reduced to 29 mJ after the first mirror and 24.5 mJ after the second mirror. A quartz port window is used on the vacuum system and no loss of energy could be detected through this window, the on target energy without focusing was measured to be 24.5 mJ. A focusing lens was then used to focus the beam to a radius of 0.5 mm, this resulted in an on target fluence of $\sim 3 \text{ J/cm}^2$. The laser was left running at 10 Hz throughout this experiment, due to the stabilizing period of the harmonic generating crystals at the 266 nm setting.

The laser regime for this experiment is similar to that usually employed for the deposition of materials. The turbomolecular pump of the plasma chamber was set to half speed, for consistency with earlier experiments where a gas would be introduced, 450 rotations per second. There was no flow of gas into the chamber nor was the gas purge on the turbomolecular pump switched on. The base chamber pressure was again $2 \cdot 10^{-5}$ mbar, and this was considered a vacuum regime with little contamination and all signal, should originate from the target surface.

The ReTOF pressure was recorded at $\sim 3 \cdot 10^{-8}$ mbar and the extraction, as earlier, was varied with the laser pulse. The resulting spectra were summed and averaged to obtain the final mass spectra shown in figure 5.29.

The strongest peak is that of O^+ at 16amu, with a Zn^+ distribution also present at ~ 65 amu. There are no multiply ionised states of Zn or O present however a zinc peroxide, ZnO_2 , peak of ~ 97 amu is present. The use of a log scale, seen inset, reveals the presence of clusters of ZnO_2 , seen as ripples in the heavier end of the mass spectra.

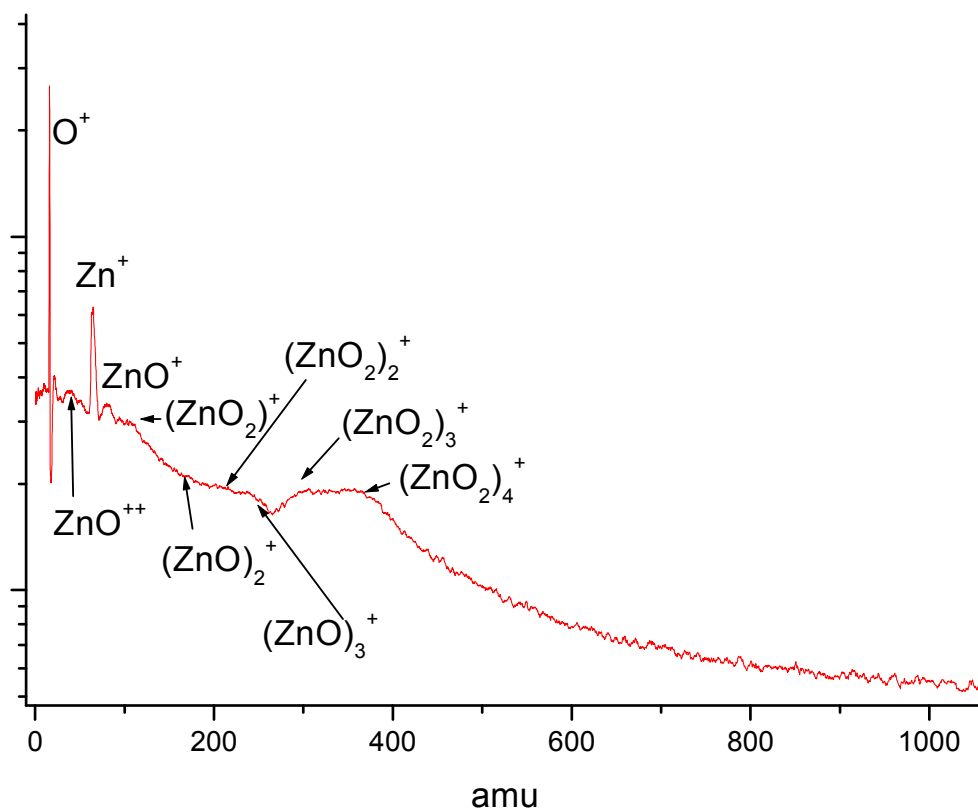


Figure 5.30: Mass spectra of ZnO, 266 nm, 10^{-4} mbar O_2 , 5 sccm.

With all settings kept the same, the mass flow controller was switched on with a flow rate of 5 sccm of O₂. The pressure increased to $\sim 3 \cdot 10^{-4}$ mbar, and the same data collecting procedure was employed for the mass spectra. The ReTOF pressure increased to $1.9 \cdot 10^{-7}$ mbar.

Again the mass spectra of figure 5.30, showed a dominant O⁺ peak at 16 amu with a minor Zn⁺ distribution at ~ 65 amu. Small peaks could be seen with a linear “Y” axis indicating the presence of ZnO⁺ at ~ 81 amu, and ZnO₂⁺ at ~ 97 amu. Again the use of a log scale enhances small signal and shows clusters of ZnO and ZnO₂ clearly up to cluster number n=3 for ZnO and n=4 for ZnO₂. Perhaps there is also the cluster number n=4 for ZnO however this may be speculative. This mass peak would appear at ~ 324 amu, however this is centred between the ZnO₂ peaks of n=3 and n=4, and it appears as a plateau in the mass spectra presented. I believe that it may be present but due to a lack of resolving power, cannot be seen.

After the presence of the ZnO₂ cluster n=4, there is a gradual drop off in signal however no “humps” or broad peaks, corresponding to the presence of an ionised Zn isotropic distribution can be deciphered within this sloping curve.

The procedure was again repeated with an increased O₂ gas pressure via the mass flow controller. The mass flow controller was set to 17 sccm, resulting in a chamber pressure of $2 \cdot 10^{-3}$ mbar. The ReTOF gas pressure increased to $1.9 \cdot 10^{-6}$, which is reaching the operational limits of the MCP detector. There was a noticeable decrease in the overall recorded signal, figure 5.31, necessitating an increase in the gain of the MCP. This is a common procedure and as long as the scan of the plasma is completed with the same gain, throughout the experiment. The relative intensities of detection of the particles should not be affected, however the noise will also increase but this should be helped by averaging.

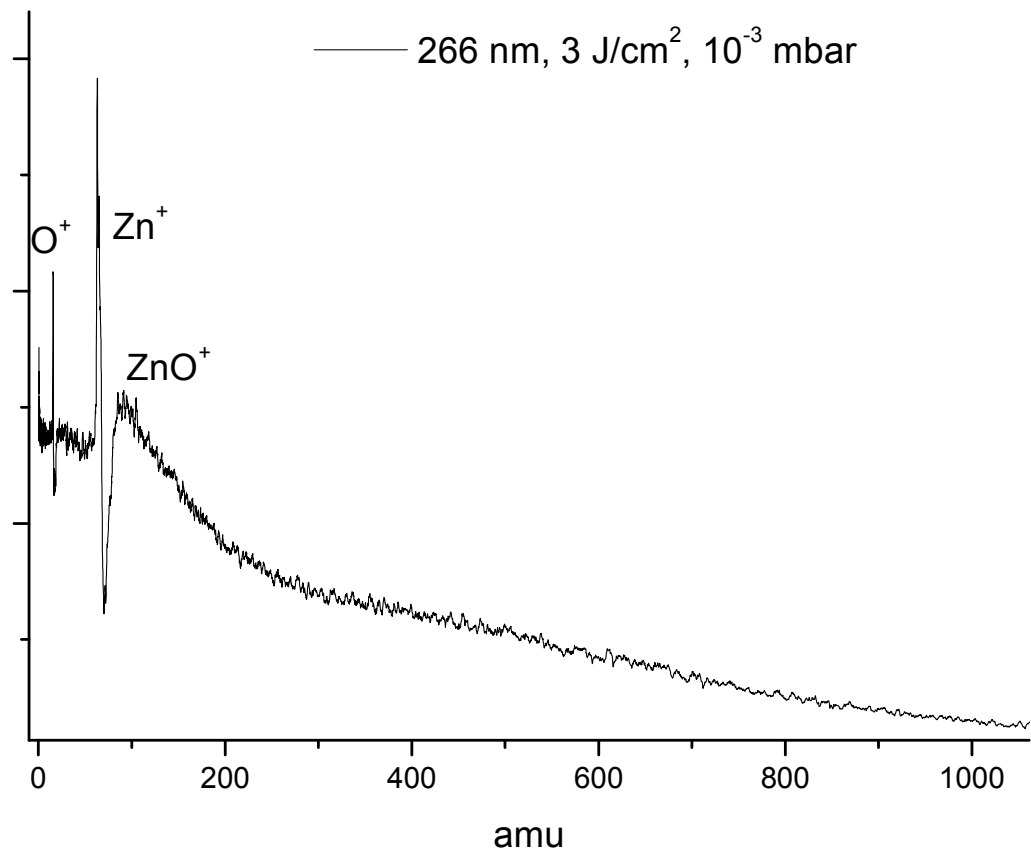


Figure 5.31: Mass spectra of ZnO, 266 nm, 10^{-3} mbar O_2 , 17 sccm.

The mass spectra for this O_2 gas pressure resulted in a reduction in the recorded O^+ signal when compared with the Zn^+ signal. It also showed no sign of the ZnO_2^+ . Both of these noticeable changes would indicate an overall reduction in the ionised oxygen, perhaps due to a recombination with the ambient oxygen. ZnO^+ is again present but no clear cluster groups stand out in the sloping reduction of signal.

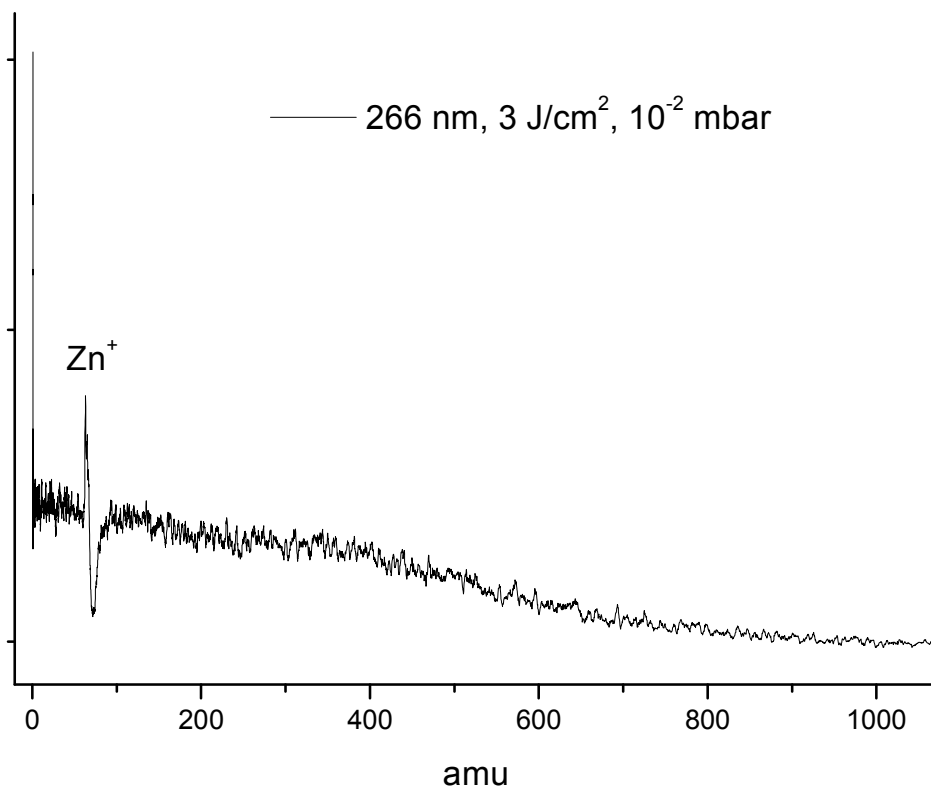


Figure 5.32: Mass spectra of ZnO, 266 nm, 10⁻² mbar O₂, 22 sccm.

Finally for the 266 nm ablations, the plasma chamber pressure was increased to 1*10⁻² mbar by applying a flow of O₂ of 22 sccm, resulting in a ReTOF chamber pressure of 4*10⁻⁶ mbar. The recorded signal was quite low with only a clear Zn⁺ mass peak, at ~65 amu, visible.

Again the signal was quite low; however it does follow the trend of a reduction in the detection of ionised oxygen with the introduction of an O₂ atmosphere.

5.5 Summary of Mass Spectra Analysis:

It is clear from tables 5.2 to 5.8 that detection of what appears to be clusters in the plume is a common occurrence. Unfortunately there is no obvious “magic number” detection for all conditions. This opposes results obtained by A. Dmytruk et al [116] for slightly different conditions, 300 μJ (fluence not given) for laser radiation of 337 nm, than those employed here, but supports results by R S. Sage et al, for similar conditions with the 533 nm ablation, with the addition here of a long tail which could indicate the presence of unresolved clusters.

Papers by L.M. Kukreja et al [15] and A. Burnin et al [123] would also support the formation of clusters in the plume but do not display the appearance of any magic numbers of ZnO.

The other outstanding results from the mass spectrum in the laser ablation of ZnO, is the ZnO target dissociates into charged Zn and O. This has consequences for the understanding of the deposition of materials, it implies that the deposition of ZnO occurs mostly due to the formation of ZnO on the surface of the substrate from Zn and O formed in the plume.

Clearly from the data there is also the formation of clusters in the vacuum regime, for all mass spectra, except that of the high fluence regime of 1064nm, this we can only assume is originating from the target surface. An increase of the gas pressure is also seen to reduce the charged states detected due to cooling of the plasma.

A reduction of the fluence also reduces the measured charge of the material and increases the likelihood of the formation of an undetermined broad peak situated where one would expect the clusters of $(\text{ZnO}_2)^{+3}$, $(\text{ZnO})^{+4}$ and $(\text{ZnO}_2)^{+4}$. The formation of this peak is also more evident with a reduction of the laser wavelength.

Table 5.2: 1064 nm Fluence: 70 J/cm²:

Ion	O ⁺⁺⁺	O ⁺⁺	O ⁺	Zn ⁺⁺⁺	Zn ⁺⁺	Zn ⁺	ZnO ⁺	ZnO ₂ ⁺	(ZnO) ₂ ⁺	Clusters
10 ⁻⁵ mbar	X	X	X	X	X	X				
10 ⁻⁴ mbar	X	X	X	X	X	X	X		X	X
10 ⁻³ mbar			X			X	X			X
10 ⁻² mbar			X			X				X

Table 5.3: 1064 nm Fluence: 0.7 J/cm²:

Ion	O ⁺⁺⁺	O ⁺⁺	O ⁺	Zn ⁺⁺⁺	Zn ⁺⁺	Zn ⁺	ZnO ⁺	ZnO ₂ ⁺	(ZnO) ₂ ⁺	Clusters
10 ⁻⁵ mbar		X	X		X	X				
10 ⁻⁴ mbar		X	X		X	X		X		X
10 ⁻³ mbar						X				
10 ⁻² mbar										

Table 5.4: 532 nm Fluence: 25 J/cm²:

Ion	O ⁺⁺⁺	O ⁺⁺	O ⁺	Zn ⁺⁺⁺	Zn ⁺⁺	Zn ⁺	ZnO ⁺	ZnO ₂ ⁺	(ZnO) ₂ ⁺	Clusters
10 ⁻⁵ mbar	X	X	X	X	X	X				X
10 ⁻⁴ mbar		X	X		X	X	X			X
10 ⁻³ mbar			X			X	X	X		X
10 ⁻² mbar						X				X

Table 5.5: 532 nm Fluence: 0.7 J/cm²:

Ion	O ⁺⁺⁺	O ⁺⁺	O ⁺	Zn ⁺⁺⁺	Zn ⁺⁺	Zn ⁺	ZnO ⁺	ZnO ₂ ⁺	(ZnO) ₂ ⁺	Clusters
10 ⁻⁵ mbar			X			X				X
10 ⁻⁴ mbar			X			X	X			X
10 ⁻³ mbar			X			X				X
10 ⁻² mbar										

Table 5.6: 355 nm Fluence: 7 J/cm²:

Ion	O ⁺⁺⁺	O ⁺⁺	O ⁺	Zn ⁺⁺⁺	Zn ⁺⁺	Zn ⁺	ZnO ⁺	ZnO ₂ ⁺	(ZnO) ₂ ⁺	Clusters
10 ⁻⁵ mbar		X	X		X	X	X			X
10 ⁻⁴ mbar		X	X		X	X	X			X
10 ⁻³ mbar			X			X	X			X
10 ⁻² mbar						X				X

Table 5.7: 355 nm Fluence: 0.7 J/cm²:

Ion	O ⁺⁺⁺	O ⁺⁺	O ⁺	Zn ⁺⁺⁺	Zn ⁺⁺	Zn ⁺	ZnO ⁺	ZnO ₂ ⁺	(ZnO) ₂ ⁺	Clusters
10 ⁻⁵ mbar			X			X		X		X
10 ⁻⁴ mbar			X			X	X	X		X
10 ⁻³ mbar			X			X	X			X
10 ⁻² mbar						X				X

Table 5.8: 266 nm Fluence: 3 J/cm²:

Ion	O ⁺⁺⁺	O ⁺⁺	O ⁺	Zn ⁺⁺⁺	Zn ⁺⁺	Zn ⁺	ZnO ⁺	ZnO ₂ ⁺	(ZnO) ₂ ⁺	Clusters
10 ⁻⁵ mbar			X			X		X		X
10 ⁻⁴ mbar			X			X	X	X		X
10 ⁻³ mbar			X			X	X			X
10 ⁻² mbar						X				X

Chapter 6:

CONCLUSIONS AND OUTLOOK

The work presented in this thesis is concerned with the wide band gap semiconductor ZnO, in regard to the deposition of material for field emission experiments and the analysis of the ionised plume of laser ablated ZnO via time of flight mass spectrometry and supplementary analysis via ion probe measurements. Two systems were designed and built during the course of this study to obtain experimental data characterising these research activities.

The field emission system and results are primarily concerned with the growth morphology and quality of field emission properties of deposited material. The results described are obtained via two different growth methods. Both methods involved the deposition of ZnO via PLD. The first method simply used the PLD deposition method to create a buffer layer for the deposition, via vapour transport, of nano-material ZnO. The second method was a variation of the traditional PLD technique whereby the plasma, instead of arriving perpendicular to the sample, arrived parallel across the substrate.

Nanomaterial ZnO was grown using both deposition techniques, with more control over the morphology via the hybrid PLD vapour transport technique. However the field emitting properties proved similar for both deposition methods, suggesting that the field enhancement factor may be as much dependent on the ZnO material electronic properties as it is on the morphology.

The analysis of the expanded plasma of ZnO showed many interesting traits both for the deposition of materials and in the high fluence regime. The presence of clusters was shown in the expanded plume but there are no obvious “magic number” detected in any conditions studied here. The other outstanding results from the mass spectroscopy analysis for the laser ablation of ZnO, is the appearance of relatively low intensity of ZnO⁺ compared with that of Zn⁺ and O⁺, therefore the ZnO molecule appears to dissociates into charged Zn and O. This

has consequences for the understanding of the deposition of materials. An undetermined broad peak situated where one would expect the clusters of $(\text{ZnO}_2)^{+3}$, $(\text{ZnO})^{+4}$ and $(\text{ZnO}_2)^{+4}$ was also shown to be more likely with a reduction of the laser wavelength and fluence to conditions associated with the deposition of materials.

The ReTOF system has been shown to perform well in lower pressure regimes and but fails to have the same detection capabilities in the higher pressures associated with the deposition of materials. Another drawback with this system is that only the charged particles are detected, an improvement of the system would be to add absorption measurements, allowing for the detection of non-emitting molecular and atomic species.

Appendix A.

Various Labview programs written for the purpose of this work:

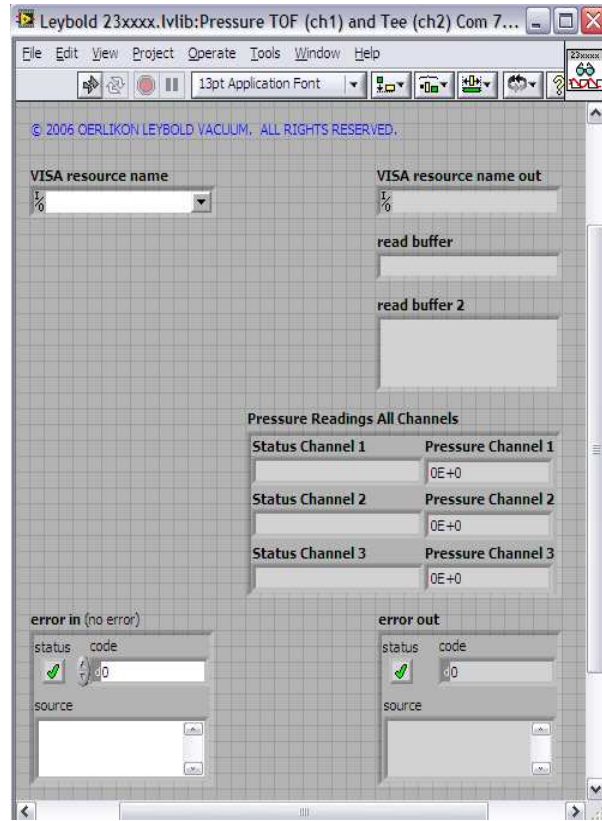


Figure Appendix A. 1. Labview Front panel for Leybold pressure gauge.

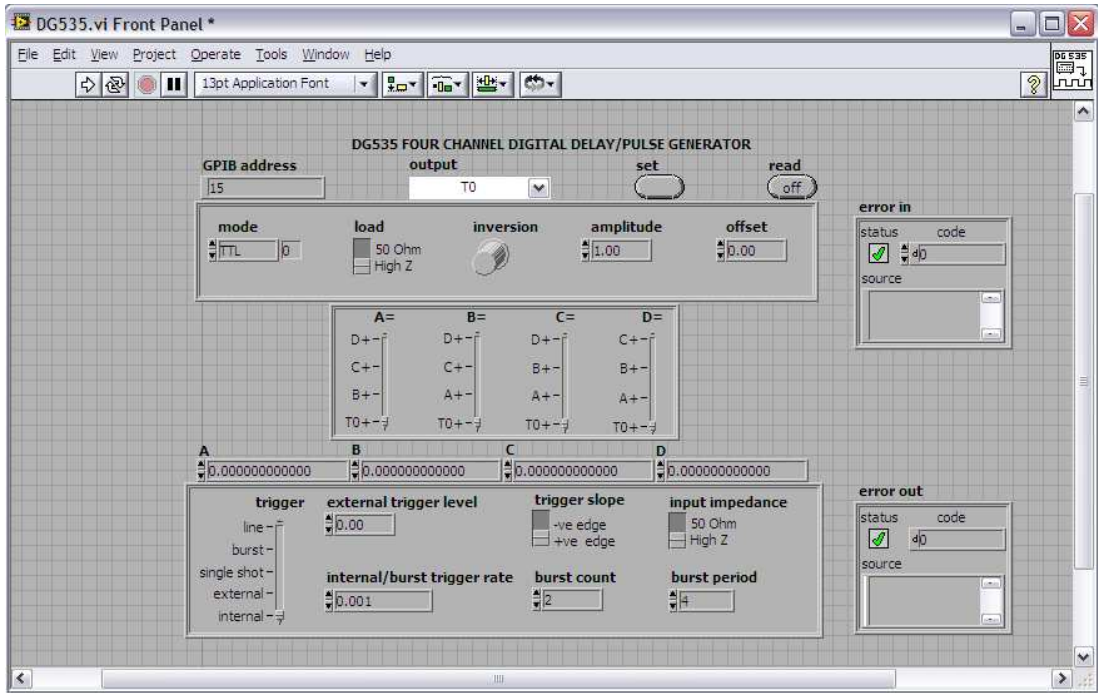


Figure Appendix A. 3. Labview Front panel for Stanford DG535 delay generator.

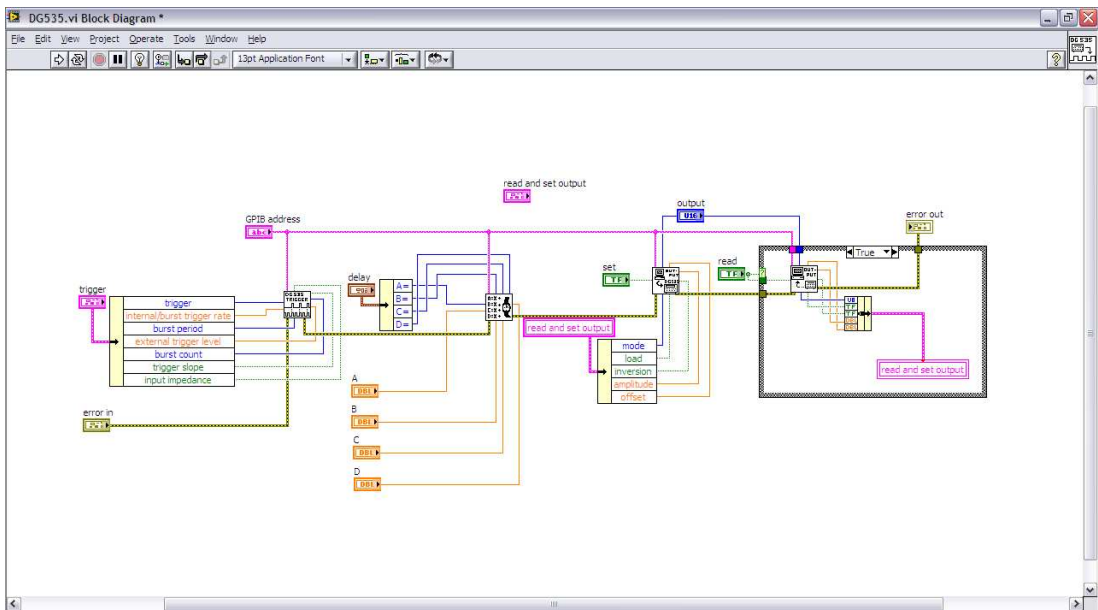


Figure Appendix A. 4. Labview block diagram for Stanford DG535 delay generator.

Appendix B:

MatLab program for data collecting:

This program performed two separate functions with the acquired data. Firstly it extracted the “Y” values of all spectra taken, and placed them into one file that could then be imported into a single “Origin” file. This data could then be analysed as one block of data without having to consider the “X”-values. The second function of this program was to sum all the “Y” values, obviously with this technique the signal will stand out from background noise.

```
close all; clear all; clc;

[fileName, pathName] = uigetfiles;
if isempty(fileName) || isequal(fileName,0)
    disp('User selected Cancel'); return;
end

[nFile, columnTemp] = size(fileName); %get number of files
% sort fileName
fileNameCell = cellstr(fileName); % convert string array to cell
array of strings
fileNameSort = sort_nat(fileNameCell);
% USRselection = menu('What sort of file is it?', 'LeCroy File','No
HeaderFVB spectrum');
%%
format long
j=0;
    %a = textread([pathName fileNameSort{1}], '%f', 'headerlines',
4); %assume 1st file is the biggest! - cone shape of stagnation layer
    %length = size(a(:,1));
z=zeros(10000,2);
x=zeros(10000,1);
all_y=zeros(10000,nFile);
for i=1:nFile
    z = dlmread([pathName fileNameSort{i}])+0.001;
    x=z(:,1);
    all_y(:,i) = z(:,2);
    %figure
    %plot(z(:,1),z(:,2));
    %axis([4e-6 12e-6 -0.01 0.08])
end
p=zeros(1,10000);
p = sum(all_y');
p = p';
save('sum_y.txt', 'p', '-ascii');
%save('test3.txt', 'all_y', '-ascii') ;
save('ally.txt', 'all_y', '-ascii')
%NB: NOW all_y contains a matrix with all the y values.
%NB: Now x contains the X values.
```

Appendix C:

Procedure for Field Emission Phosphor Screens [124]:

ZnO layer:

- 1). Mix 10ml of ethanol and 0.054g of zinc acetate in a beaker.
- 2). Place a magnetic stirrer into the beaker and place on hot plate with stir function, stir for 20 minutes.
- 3). Clean substrate (glass / Pyrex) in Isopropyl alcohol, and dip for 10 seconds in solution.
- 4). Holding the substrate at 45° dry the substrate using the nitrogen gas gun, raster the gun with a slow gas flow across the substrate until dry.
- 5). Repeat steps 3) and 4) five times.
- 6). With the oven set to 350°C insert the slide to the centre of the oven and leave for 20 minutes.
- 7). Repeat steps 3-6.

Phosphor Layer:

- 1). Grind the phosphors in a crucible for 5 minutes.
- 2). Add 7 mg of the phosphor to 5-10 ml of ethanol.
- 3). Manually stir the solution until the phosphor is diffused in the liquid.
- 4). Submerge the ZnO layered substrate into the solution.
- 5). Leave for 5 minutes.
- 6). Remove the Ethanol using a pipette.
- 7). Heat the beaker to 50° to evaporate the remaining ethanol.
- 8). Heat the substrate to 350° for 30 minutes.

Repeat the ZnO Layer Procedure

References:

- [1] <http://www.webelements.com/webelements/compounds/text/Zn/O1Zn1-1314132.html>
- [2] C. W. Bunn. Proc. Phys. Soc 47, (1935) 835.
- [3] D. M. Bagnall, Y. F. Chen, Z. Zhu, T. Yao, S. Koyama, M. Y. Shen, T. Goto. Appl. Phys. Lett. 70, (1997) 2230.
- [4] Zhong Lin Wang, J. Phys. : Condens. Matter 16 (2004) R829
- [5] T. Yasui, M. Yasuda, D. Nezaki, M. Takata, B. P. Zhang, Y. Segawa. Thin Solid Films 464-465, (2004), 276.
- [6] D.C. Look, D.C. REYNOLDS, J. W. HEMSKY, R.L. JONES; J.R. SIZELOVE; Applied Physics Letters 75, (1999), 811.
- [7] Y.Huh, J.Y.Lee, J.H.Lee, T.J.Lee, S.C.Lyu, C.J.Lee. Chemical Physics Letters 375 (2003), 388.
- [8] B. Doggett, S. Chakrabarti, R. O'Haire, A. Meaney, E. McGlynn, M.O. Henry and J.P. Mosnier. Superlattices and Microstructures 42, (2007), 74.
- [9] J Zúñiga-Pérez, A Rahm, C Czekalla, J Lenzner, M Lorenz and M Grundmann Nanotechnology 18 (2007) 195303
- [10] Ye Sun, Gareth M. Fuge and Michael N.R. Ashfold. Superlattices and Microstructures 39, (2006) 33.
- [11] Mitsuhsa Kawakami, Agung Budi Haranto, Yoshiki Nakata and Tatsuo Okada. Jpn. J. Appl. Phys. Vol. 42 (2003) pp. L 33.
- [12] I. Ozerov, A.V. Bulgakov, D.K. Nelson, R. Castell and W. Marine. Applied Surface Science 247 (2005) 1.
- [13] J. Mühlbach, K. Sattler, P. Pfau and E. Recknagel Physics Letters A 87,(1982), 415

-
- [14] L. Clark *Materials Today* 4 (1999) 10.
- [15] L.M. Kukreja, A. Rohlfing, P. Misra, F. Hillenkamp and K. Dreisewerd. *Appl. Phys. A* 78, (2004) 641.
- [16] E.C. Behrman, R.K. Fochrweiser, J.K. Myers and B.R. French. *Phys Rev. A* 49, (1994) R1543.
- [17] R.T. Rajendra Kumar, E. Mc Glynn, C. Mc Loughlin, S. Chakrabarti, R.C. Smith, J.D. Carey, J.P. Mosnier and M.O. Henry, *Nanotechnology* 18 (2007) 215704
- [18] Thomas Goislard De Monsaberta, Jean Dijona and Patrice Gadelieb, *Carbon* 43,(2005), 2441
- [19] Ralph Formana *Applications of Surface Science* 16,(1983), 277
- [20] S.R.P. Silva, J.D. Carey, X. Guo, W.M. Tsang, C.H.P. Poa. *Thin Solid Films* 482 (2005) 79.
- [21] Robert Gomer, *Field Emission and Field Ionization*, American Vacuum Society Classics, 1993.
- [22] J Bardeen *Physical Review* 49 (1936) 653.
- [23] E. Wigner, J. Bardeen *Physical Review* 48 (1935) 84.
- [24] N.D. Lang, W. Kohn *Physical Review B* 1 (1970) 4555.
- [25] K.L. Jensen *Journal of Applied Physics* 85 (1999)2667
- [26] O.W. Richardson *Proc. Roy. Soc. A* 117 (1928) 719.
- [27] Owen W. Richardson's Nobel lecture on thermionics, December 12, 1929.
- [28] L.W. Nordheim *Proc. Roy. Soc. A* 121 (1928) 626.
- [29] N. A. de Bruyne *Proc. Roy. Soc. A* 120(1928)423.
- [30] E.L. Murphy and R.H. Good, *Phys. Rev.* 102 (1956) 1464

-
- [31] R. A. Millikan and C. C. Lauritsen Proceedings of the National Academy of Sciences of the United States of America 14 (1928) 45
- [32] R. H. Fowler and L. Nordheim Proc. Roy. Soc. A. 119 (1928) 173.
- [33] R.W.Wood Phys. Rev. 5 (1897) 1.
- [34] R.D. Young Phys. Rev. 113 (1959) 110.
- [35] S.C. Miller Jr and R.H. Good Jr Phys. Rev. 91 (1953) 174.
- [36] W. W. Dolan and W. P. Dyke Phys. Rev. 95, (1954), 327
- [37] Sommerfeld & H. Bethe, Handbuch der Physik 24, (1933) 441.
- [38] J. B. Cui, J. Robertson, W.I.Milne. Journal of Applied Physics, 89 (2001) 5707.
- [39] S. Eliezer and Y Eliezer The Fourth State of Matter, An introduction to Plasma Science, IOP Publishing Ltd 2001, ISBN 0 7503 0740 4.
- [40] Bellan, P.M. Fundamentals of Plasma Physics, Chapter 1. Cambridge University Press, 2006. ISBN: 0-521-82116-9
- [41] Carroll, P.K.; Kennedy, E.T. Contemporary Physics 22 61-96 1981.
- [42] Fitzpatrick, R.; Hazeltine, R.D.; Waelbroeck F.L.; Introduction to Plasma Physics A graduate level course, Chapter 6.2.
- [43] E.D. Palik handbook of optical constants of solids II Academic press, London, 1991
- [44] Rothwell, E.J.; Cloud, M.J. Electromagnetics, Chapter 4. CRC Press, Electrical Engineering Textbook Series, 2001. ISBN: 0-8493-137-X.
- [45] P. R. Willmott and J. R. Huber Rev Mod Phys, 72 (2000)315
- [46] E. Hecht. Optics, Third Edition. Addison-Wesley, New York, 1998.]
- [47] http://www.luxpop.com/result_MC_4048.php

-
- [48] C. R. Phipps, Jr., T. P. Turner, R. F. Harrison, G. W. York, W. Z. Osborne, G. K. Anderson, X. F. Corlis, L. C. Haynes, H. S. Steele, and K. C. Spicochi J. Appl. Phys. 64, (1988) 1083
- [49] Rajiv K. Singh and J. Narayan Phys Rev B. 41, (1990) 8843.
- [50] S. I. Anisimov, B. S. Luk'yanchuk, A. Luches, Appl Surf Sci, 96-98(1996) 24.
- [51] Andrey V. Gusarov and Alexey G. Gnedovets Journal of Applied Physics 88 (2000) 4352.
- [52] R. Kelly and R.W. Dreyfus, Nuclear Instruments and Methods in Physics Research B 32, (1988) 341.
- [53] Roger Kelly and R. W. Dreyfus Surface Science 198 (1988) 263.
- [54] P. K. Wu, B. R. Ringeisen, D. M. Bubb, R. C. Y. Auyeung, J. Horwitz, E. J. Houser, A. Piqué, R. A. McGill, and D. B. Chrisey, Journal of Applied Physics 90 (2001) 3623.
- [55] H.M. Mott-Smith and Irving Langmuir Phys Rev. 28 (1926) 727.
- [56] D.W. Koopman and D. A. Tidman Phys. Rev Lett. 18 (1967) 533.
- [57] David W. Koopman, The physics of Fluids 14 (1971) 1707.
- [58] I. H. Hutchinson Principals of Plasma Diagnostics Second Edition, Cambridge University Press 2002 ch. 3.
- [59] E. Goldstein Sitzungsberichte der Koniglich Preussischen Academie der Wissenschaften zu Berlin 39 (1886) 691.
- [60] W. Wien Annalen der Physik und Chemie Leipzig, 8 (1902) 224.
- [61] J.J. Thomson Rays of Positive Electricity and their Application to Chemical Analysis, Longmans, Green and Co. 1913.
- [62] William Siri, Rev. Sci. Instrum. 18, (1947) 540.

-
- [63] W. E. Parkins, *Physics Today* 58 (5) (2005) 45–51
- [64] M.M. Wolff and W.E. Stephens *Rev. Sci. Instrum.* 24 (1953) 616
- [65] A.Vertes, R. Gijbels, F. Adams. *Laser ionisation Mass Analysis*, Wiley Interscience 1993.
- [66] Jürgen H. Gross *Mass Spectrometry* Springer 2004.
- [67] G. Sanzone *Rev. Sci Instr.* 41 (1970) 741.
- [68] W.C. Wiley and I.H. McLaren *Rev. Sci. Instr.* 26 (1955) 1150.
- [69] B.A. Mamyrin *Int. Jour. Mass Spec.* 206 (2001) 251.
- [70] B.A. Mamyrin, V.I. Karataev, D.V. Shmikk and V.A. Zagulin *Sov. Phys. JETP* 37 (1973) 45.
- [71] D.A. Dahl *International Journal of Mass Spectrometry* 200 (2000) 3.
- [72] G.Z. Yue, Q. Qiu, Bo Gao, Y. Cheng, J. Zhnag, H. Shimoda, J.P. Lu and O. Zhou, *Appl. Phys. Lett.* 81 (2002) 355.
- [73] J.D. Carey, *Phil. Trans. R. Soc. Lond. A* 361 (2003) 2891.
- [74] S.R.P. Silva, J.D. Carey, X. Guo, W.M. Tsang, C.H.P. Poa, *Thin Solid Films* 482 (2005) 79.
- [75] Jean-Marc Bonnard, Hannes Kind, Thomas Stöckli, Lars-Ola Nilsson, *Solid State Electron.* 45 (2001) 893.
- [76] Lee C J, Lee T J, Lyu S C, Zhang Y, Ruh H and Lee H J *Appl. Phys. Lett.* 81 (2002) 3648
- [77] Xu C X and Sun X W *Appl. Phys. Lett.* 83 (2003) 3806
- [78] Zhu Y W, Zhang H Z, Sun X C, Feng S Q, Xu J, Zhao Q, Xiang B, Wang R M and Yu D P *Appl. Phys. Lett.* 83 (2003) 144

-
- [79] Cui J B, Daghlia C P, Gibson U J, Pusche R, Geithner P and Ley L J. Appl. Phys. 97 (2005) 044315
- [80] M. Biswas, E. McGlynn, M. O. Henry, M. McCann and A. Rafferty Journal of Applied Physics 105, (2009) 094306.
- [81] Nilsson L, Groening O, Emmenegger C, Kuettel O, Schaller E, Schlapbach L, Kind H, Bonard J-M and Kern K Appl. Phys. Lett. 76 (2000) 2071
- [82] Jo S H, Lao J Y, Ren Z F, Farrer R A, Baldacchini T and Fourkas J T Appl. Phys. Lett. 83 (2003) 4821
- [83] T. Okada, K. Kawashima, M. Ueda, Appl. Phys. A 81 (2005) 907;
- [84] R. O'Haire, E. McGlynn, M.O. Henry, J.-P. Mosnier., Superlattice Microst. 42 (2007) 468
- [85] J.C. Sit, D. Vick, K. Robbie, M.J. Brett. J. Mater Res. 14 (1999) 1197.
- [86] J. Lintymer, J. Gavaille, N. Martin, J. Takadoum Surface and Coating Technology 174 (2003) 316
- [87] Q. Zhao, X.Y. Xu, X.F. Song, X.Z. Zhang, D.P. Yu, C.P. Li, L. Guo. Appl. Phys. Lett. 88 (2006) 033102.
- [88] Z.W. Liu, C.K. Ong, T. Yu and Z.X. Shen, Appl. Phys. Lett. 88 (2006) 053110.
- [89] Kungen Teii, Seiichiro Matsumoto, John Robertson. Appl. Phys. Lett. 92 (2008) 013115.
- [90] D.F. Liu, Y.J. Xiang, X.C. Wu, Z.X. Zhang, L.F. Liu, L. Song X.W. Zhao, S.D. Luo, W.J. Ma, J. Shen, W.Y. Zhou, G. Wang, C.Y. Wang, S.S. Xie. Nano Lett. 6 (2006) 2375.
- [91] Ning Zhang, Ke Yu, Yongsheng Zhang, Wei Bai, Ziqiang Zhu. Curr. Appl. Phys. 9 (2009) 34.

-
- [92] Q. Ahsanulhaq, Jin-Hwan Kim and Yoon –Bong Hahn *Nanotechnology* 18 (2007) 485307
- [93] Mohamed A. Khater, John T. Costello, and Eugene T. Kennedy. *Applied Spectroscopy*. 56, 2002, 970.
- [94] Masayuki Suzuki, Rashid A. Ganeev, Motoyoshi Baba, Hiroto Kuroda, *Physics Letters A* 372 (2008) 4480–4483.
- [95] F. Flora, L. Mezi, C. E. Zheng, and F. Bonfigli *Europhys. Lett.* **56** (2001)676.
- [96] D. B. Chrisey and G. K. Hubler, *Pulsed Laser Deposition of Thin Films* Wiley 1994.
- [97] R.C.Isaac, G.K. Varier, P. Gopinath, S.S. Harilal, V.P.N. Nampoori and C.P.G. Vallabhan. *Appl. Phys. A* 67, 1998, 557-561.
- [98] P. Hough, C. McLoughlin, T.J.Kelly, S.S. Harilal, J.P. Mosnier and J.T. Costello. *Applied Surface Science*, 255, 2009, 5167-5171.
- [99] D.W. Koopman and D. A. Tidman *Phys. Rev. Lett.* 18, 1967, 533.
- [100] H. Cronberg, M. Reichling, E. Broberg, H.B. Nielsen, E. Matthias and N. Tolk. *Appl. Phys. B*. 52, 1991, 155-157.
- [101] Riju C. Issac, Pramod Gopinath, Geetha K. Varier V. P. N. Nampoori and C.P.G. Vallabhan. *Appl. Phys. Lett.* 73, 1998, 163.
- [102] R.F. Wood J.N. Leboeuf, D.B.Geohegan, A.A. Puretzky and K.R. Chen *Physical Review B* Vol. 58, 1533, 1998.
- [103] S. Amoruso, M. Armenante, R. Bruzzese, N. Spinelli, R. Velotta and X. Wang. *Applied Physics Letters*, 75, 1999,7-9.
- [104] Morihisa Saeki, Kohichi Hirata, Tetsuo Sakka, Hironori Ohba and Atsushi Yokoyama. *Journal of Applied Physics* 98, 2005, 044912.

-
- [105] S.S. Harilal, Beau O'Shay, Yezhang Tao and Mark S. Tillack. *Journal of Applied Physics*, 99, 2006, 083303.
- [106] R. O'Haire, E. McGlynn, M.O. Henry and J.-P. Mosnier. *Superlattices and Microstructures* 42 (2007) 468–472.
- [107] Ye Sun, Gareth M. Fuge and Michael N.R. Ashfold. *Superlattices and Microstructures* 39 (2006) 33–40.
- [108] M. Lorenz, E. M. Kaidashev, A. Rahm, Th. Nobis, J. Lenzner, G. Wagner, D.Spemann, H. Hochmuth, and M. Grundmann. *Applied Physics Letters* 86 (2005) 143113.
- [109] R. S. Sage, U. B. Cappel, M. N. R. Ashfold, N. R. Walker *Journal of Applied Physics*, 103 (2008) 093301.
- [110] M. Yan, H. T. Zhang, E. J. Widjaja, and R. P. H. Chang. *Journal of Applied Physics* 94 (2003) 5240.
- [111] Mitsuhsa Kawakami, Agung Budi Haranto, Yoshiki Nakata and Tatsuo Okada. *Jpn. J. Appl. Phys.* 42 (2003) L 33–L 35.
- [112] T. Okada, K. Kawashima and Y. Nakata. *Thin Solid Films* 506 (2006) 274.
- [113] T. Okada, B.H. Agung and Y. Nakata. *Applied Physics A* 79 (2004) 1417.
- [114] V. Berardi, S. Amoruso, N. Spinelli, M. Armenante, R. Velotta, F. Fuso, M. Allegrini and E. Arimondo. *J. Appl. Phys.* 76 (1991) 8077
- [115] A. Dmytruk , I. Dmitruk , A. Kasuya *Mat.-wiss. u. Werkstofftech.* 2009, 40, No. 4
- [116] A. Dmytruk, I. Dmitruk, I. Blonskyy, R. Belosludov, Y. Kawazoe, A. Kasuya. *Microelectronics Journal* 40 (2009) 218.
- [117] W.L. Fite and R.T. Brackmann, *Physical Review* 113 (1959) 815-816.
- [118] M. J. Seaton, *Physical Review* 113 (1959) 814.

[119] H. Cronberg, M. Reichling, E. Broberg, H.B. Nielsen, E. Matthias and N. Tolk. Appl. Phys. B. 52, 1991, 155-157.

[120] S. Amoruso, M. Armenante, R. Bruzzese, N. Spinelli R. Velotta, X. Wangc Applied Physics Letters 75 (1999) 7.

[121] S. Zoppel H. Huber G.A. Reider Applied Physics A 89 (2007) 161.

[122] Frédéric Aubriet and Jean-François Muller J Am Soc Mass Spectrom 19, (2008), 488

[123] Andrei Burnin, Joseph J. BelBruno Chemical Physics Letters 362 (2002) 341-348

[124] Lori E. Greene, Matt Law, Joshua Goldberger, Franklin Kim, Justin C. Johnson, Yanfeng Zhang, Richard J. Saykally, Peidong Yang 42 (2003) 3031